TECHNICAL REPORT

Semi-Annual Technical Report No. 4

STRUCTURE AND PROPERTY CONTROL THROUGH RAPID QUENCHING OF LIQUID METALS

Sponsored by
Advanced Research Projects Agency
Contract No.: DAHC15 70 C 0283

CENTER FOR MATERIALS SCIENCE AND ENGINEERING

Massachusetts Institute of Technology
Cambridge, Massachusetts 02139

R 140

For period - January 1, 1972 to July 31, 1972

Semi-Annual Technical Report No. 4

STRUCTURE AND PROPERTY CONTROL THROUGH RAPID QUENCHING OF LIQUID METALS

Sponsored by
Advanced Research Projects Agency
Contract No.: DAHC15 70 C 0283

ARPA Order No.: 1608
Program Code No.: 0D10

Contractor:

Massachusetts Institute of Technology
Cambridge, Massachusetts 02139

Principal Investigator:

N.J. Grant
(617) 253-5638

Effective date of Contract: June 22, 1970
Contract Expiration Date: July 21, 1972

Total Amount of Contract: $470,300
ARPA Order No. 1608

DOCUMENT CONTROL DATA - R&D

(Security classification of title, body of abstract and indexing annotation must be entered when the overall report is classified)

1. ORIGINATING ACTIVITY *(Corporate author)*
Massachusetts Institute of Technology
Cambridge, Massachusetts 02139

2a. REPORT SECURITY CLASSIFICATION
unclassified

2b. GROUP

3. REPORT TITLE

Structure and Property Control Through Rapid Quenching of Liquid Metals

4. DESCRIPTIVE NOTES *(Type of report and inclusive dates)*
Semi-Annual Technical Report #4, (January 1, 1972-July 31, 1972)

5. AUTHOR(S) *(Last name, first name, initial)*

Nicholas J. Grant, Regis M. Pelloux, Merton C. Flemings, Ali S. Argon

6. REPORT DATE
July 31, 1972

7a. TOTAL NO. OF PAGES
114

7b. NO. OF REFS

8a. CONTRACT OR GRANT NO.
DAHC 70 C 0283

b. PROJECT NO.

c. ARPA Order #1608

d. Program Code #0D10

9a. ORIGINATOR'S REPORT NUMBER(S)

9b. OTHER REPORT NO(S) *(Any other numbers that may be assigned this report)*

10. AVAILABILITY/LIMITATION NOTICES

11. SUPPLEMENTARY NOTES

12. SPONSORING MILITARY ACTIVITY
Advanced Research Projects Agency
1400 Wilson Blvd.
Arlington, Virginia 22209

13. ABSTRACT

This report presents the results and accomplishments of the fourth six-month period of a three year research program investigating the processing of billets from rapidly quenched liquid metals.

Various powder metallurgy (P/M) and quench-casting techniques have been employed to generate extremely fine dendrite arm spacings and homogeneous structures. Iron, nickel and cobalt-base alloy powders, produced by steam atomization (coarse powders), argon atomization, vacuum atomization, and the rotating electrode process, have been consolidated into dense billets by hot isostatic pressing (HIP) and/or extrusion. New powder processes based on separating solid nodules from a liquid-solid mixture and random break up of a fine stream of liquid metal into spherical particles are being evaluated.

The hot working properties of P/M billets and quench-cast bars have been evaluated by hot rolling, high strain rate tests, and creep (superplastic)testing. Two P/M superalloys, MAR-M-509 (cobalt-base) and IN-100 (nickel-base) after HIP and hot extrusion demonstrated excellent hot workability under high strain rate and creep forming conditions, respectively.

Detailed analyses of microstructure, heat treatment, and mechanical properties are presented for all P/M alloys and compared to equivalent cast materials. Room temperature properties of P/M alloys continue to be far superior to their cast counterparts. Elevated temperature properties are significantly improved by proper heat treatments.

DD FORM 1 JAN 64 **1473**

14 KEY WORDS	LINK A		LINK B		LINK C	
	ROLE	WT	ROLE	WT	ROLE	WT
Rapid Quenching Structure and Segregation Control Powder Metallurgy						

INSTRUCTIONS

1. ORIGINATING ACTIVITY: Enter the name and address of the contractor, subcontractor, grantee, Department of Defense activity or other organization *(corporate author)* issuing the report.

2*a*. REPORT SECURITY CLASSIFICATION: Enter the overall security classification of the report. Indicate whether "Restricted Data" is included. Marking is to be in accordance with appropriate security regulations.

2*b*. GROUP: Automatic downgrading is specified in DoD Directive 5200.10 and Armed Forces Industrial Manual. Enter the group number. Also, when applicable, show that optional markings have been used for Group 3 and Group 4 as authorized.

3. REPORT TITLE: Enter the complete report title in all capital letters. Titles in all cases should be unclassified. If a meaningful title cannot be selected without classification, show title classification in all capitals in parenthesis immediately following the title.

4. DESCRIPTIVE NOTES: If appropriate, enter the type of report, e.g., interim, progress, summary, annual, or final. Give the inclusive dates when a specific reporting period is covered.

5. AUTHOR(S): Enter the name(s) of author(s) as shown on or in the report. Enter last name, first name, middle initial. If military, show rank and branch of service. The name of the principal author is an absolute minimum requirement.

6. REPORT DATE: Enter the date of the report as day, month, year; or month, year. If more than one date appears on the report, use date of publication.

7*a*. TOTAL NUMBER OF PAGES: The total page count should follow normal pagination procedures, i.e., enter the number of pages containing information.

7*b*. NUMBER OF REFERENCES: Enter the total number of references cited in the report.

8*a*. CONTRACT OR GRANT NUMBER: If appropriate, enter the applicable number of the contract or grant under which the report was written.

8*b*, 8*c*, & 8*d*. PROJECT NUMBER: Enter the appropriate military department identification, such as project number, subproject number, system numbers, task number, etc.

9*a*. ORIGINATOR'S REPORT NUMBER(S): Enter the official report number by which the document will be identified and controlled by the originating activity. This number must be unique to this report.

9*b*. OTHER REPORT NUMBER(S): If the report has been assigned any other report numbers *(either by the originator or by the sponsor)*, also enter this number(s).

10. AVAILABILITY/LIMITATION NOTICES: Enter any limitations on further dissemination of the report, other than those imposed by security classification, using standard statements such as:

(1) "Qualified requesters may obtain copies of this report from DDC."

(2) "Foreign announcement and dissemination of this report by DDC is not authorized."

(3) "U. S. Government agencies may obtain copies of this report directly from DDC. Other qualified DDC users shall request through
____."

(4) "U. S. military agencies may obtain copies of this report directly from DDC. Other qualified users shall request through
____."

(5) "All distribution of this report is controlled. Qualified DDC users shall request through
____."

If the report has been furnished to the Office of Technical Services, Department of Commerce, for sale to the public, indicate this fact and enter the price, if known.

11. SUPPLEMENTARY NOTES: Use for additional explanatory notes.

12. SPONSORING MILITARY ACTIVITY: Enter the name of the departmental project office or laboratory sponsoring *(paying for)* the research and development. Include address.

13. ABSTRACT: Enter an abstract giving a brief and factual summary of the document indicative of the report, even though it may also appear elsewhere in the body of the technical report. If additional space is required, a continuation sheet shall be attached.

It is highly desirable that the abstract of classified reports be unclassified. Each paragraph of the abstract shall end with an indication of the military security classification of the information in the paragraph, represented as *(TS)*, *(S)*, *(C)*, or *(U)*.

There is no limitation on the length of the abstract. However, the suggested length is from 150 to 225 words.

14. KEY WORDS: Key words are technically meaningful terms or short phrases that characterize a report and may be used as index entries for cataloging the report. Key words must be selected so that no security classification is required. Identifiers, such as equipment model designation, trade name, military project code name, geographic location, may be used as key words but will be followed by an indication of technical context. The assignment of links, rules, and weights is optional.

TABLE OF CONTENTS

LIST OF TABLES

Table Number

Page Number

TASK I

TASK II

TASKS III and IV

Maraging Steels

Cobalt-Base Alloys

LIST OF TABLES- cont'd

LIST OF FIGURES

LIST OF FIGURES - cont'd

TASK II

LIST OF FIGURES - cont'd

LIST OF FIGURES - cont'd

TASKS
III
and IV

Maraging Steels

Cobalt-Base Alloys

LIST OF FIGURES - cont'd

Medium Carbon Steel

LIST OF FIGURES - cont'd

TASK I

Processing of Alloys

P.E. Price

R. Widmer

J. Blucher

TASK I

Processing of Alloys

I. INTRODUCTION

Task I work on structure and property control through rapid quenching of liquid metals during the present reporting period has included three major aspects: (1) study of the relation of metal chemistry to oxide pick-up in steam atomization, (2) production of consolidated bar material for property determination in Task III, and (3) study of the inter-relationships of powder chemistry including "inert" gas content, hot isostatic pressing parameters, and heat treatment on microstructure of low carbon and normal carbon IN-100.

II. EXPERIMENTAL WORK

A. Melting and Atomization

Table I summarizes all melting and atomization runs carried out by Task I.

1. Maraging Steel

Previous experience with steam and argon atomization in an open system of maraging steel to produce a coarse rounded powder in the 500 - 5000 micron size range has shown that the easily oxidizable elements titanium and aluminum are "lost" in atomization. Secondly, powder particles show a dispersion of oxide inclusions, with a general trend of larger inclusions in the smaller metal powder particles. Thirdly, oxygen level in the tundish stream at the point of atomization has been shown to be as low as 40 ppm.

Present work was aimed at determining the effect of carbon level in the melt on oxygen pick-up in steam atomization for an alloy whose atomization characteristics were known. Accordingly, 20 lb. heats of a "300" grade maraging steel were atomized with nominal carbon levels of 0.2, 0.4, 0.6, 0.8, and 1.0 wt. %. It is recognized that the transformation characteristics of this grade would be destroyed at the carbon levels used, but the primary interest was in metal chemistry. Coarse powder produced in the experiments

(See Table I) was chemically cleaned, screened into separate size fractions, and analyzed for carbon and oxygen. Results are summarized in Table II.

The oxygen levels in the powder fractions are substantially independent of carbon level and similar to levels previously found in coarse powder of this alloy. Cooling of the liquid metal droplets after atomization and simultaneous oxygen pick-up apparently occurs too rapidly for oxygen to be removed by a carbon deoxidation reaction. Structurally the oxygen contents are partially accountable as a dispersion of oxide inclusions, Figure 1.

2. Stainless Steel

Investigation of the effect of chromium level on oxygen pick-up in steam atomization of a 10% Ni stainless steel was also carried out. Atomization conditions are given in Table I. Nominal metal chemistries and oxygen levels of various powder fractions are given in Table II. Oxygen levels of the fractions are substantially independent of chromium level for the range investigated. Melt oxygen was higher than for maraging steel, possibly due to melting practice which used separate components, including low carbon ferrochrome instead of vacuum melted and fully prealloyed melt stock.

Oxygen level increased at smaller particle sizes and was generally lower than for VM-300 maraging steel (compare data in Table II). Structurally, a fine dispersion of rounded oxide inclusions was found, Figure 2. Except for the 12% Cr composition, which had the highest oxygen level (Table II), there are generally fewer very fine inclusions in the -25/+30 mesh stainless powders compared to maraging steel. This difference and the generally lower oxygen level for the various stainless steel powder fractions indicates that metal chemistry has a pronounced effect on the mechanics of oxygen pick-up.

Aside from the thermodynamics of oxidation of a particular composition, "secondary" variables such as metal/oxide (oxide may be liquid) interfacial energy and liquid phase viscosity may influence the mixing of surface oxide into the liquid metal droplets during the "shearing" action of atomization. Thus the final oxygen level in a coarse powder after cleaning cannot be generally predicted, but must be determined experimentally for a given composition.

3. Cobalt Alloys

One heat of a modified Mar M 509 composition was steam atomized and cleaned for processing by hot isostatic pressing plus extrusion. Nominal composition is given in Table II. Chemical cleaning reduced oxygen in the coarse powder to $\sim$ 400 ppm, (Table II).

B. Powder Consolidation

1. Objectives

Powder consolidation was carried out by hot isostatic pressing, hot isostatic pressing followed by extrusion, and direct extrusion. Objectives were:

a. Produce material for testing of high temperature properties by Task III.

b. Study the microstructural response to hot isostatic pressing parameters.

c. Study the response to heat treatment of material consolidated by hot isostatic pressing with particular attention to "thermally induced" porosity.

With respect to the last objective, it has been recognized that a limitation to the use of superalloy powder products for applications at $> 1600^{\circ}$F has been small grain size. Powder consolidated by extrusion frequently has a grain size in the $\sim$1-5 micron range. "Successful" grain coarsening treatments increase the size to $\sim 100\mu$, but cast grain size of IN-100 parts (for example) for high temperature application ($> 1600^{\circ}$F) is usually $> 1500\mu$. With normal carbon IN-100, as reported earlier, grain growth is limited by carbide networks around prior particle boundaries. When the carbon level is reduced, large grain material may be produced but void formation frequently accompanies grain growth.

2. Hot Isostatic Pressing Runs

All hot isostatic pressing runs completed in the present reporting period are summarized in Table III. HIP extrusion billets were all successfully extruded. IN-100 HIP bars were used primarily for study of microstructure dependence on heat treatment.

3. Microstructures

As discussed earlier, the usefulness of powder metallurgy processing for control of structure and high temperature properties ($>$ 1600°F) of superalloys depends in some alloy systems on the response of consolidated material to grain growth heat treatments. Since hot isostatic pressing may ultimately be used for production of finished parts, it was considered useful to determine the heat treatment response of HIP material produced from low carbon IN-100 powder. Accordingly, microstructures were examined for a variety of pressing conditions and heat treatments.

a. HIP @ 2000°F ($\ll \gamma'$ solvus)

Low carbon IN-100 powder was consolidated to substantially 100% density (Run #5, Can No. 2A37, Table III), Figure 3. Heat treatment above the γ' solvus produces substantial grain growth ($\sim$ 300μ g.s.) but also an "unstable" grain boundary structure and a few "thermally induced" pores, Figure 4. Additional time at 2275°F increases grain size to $\sim$ 400-500μ, reduced the "disturbance" at the grain boundaries, but also generates large round pores, Figure 5.

b. HIP @ 2250°F ($< \gamma'$ solvus)

Porosity formation during heat treatment after HIP at 2000°F might be attributed to incomplete bonding between particles. However, material pressed at 2250°F (Run #3, Can No. 2A20, Table III), which is just below the γ' solvus, showed identical structural behavior during heat treatments as in Figures 4 and 5.

c. HIP @ 2275°F ($> \gamma'$ solvus, $<$ solidus)

To avoid pore formation during grain growth, direct HIP processing above the γ' solvus was carried out (Run #7, Can No. 2A42, Table III). A grain size of $\sim 200\mu$ was achieved along with some massive white phase at grain boundaries, "stable" grain boundaries, and no "large" pores, Figure 6. Subsequent heat treatment and grain growth to $\sim 400\mu$ g.s. of this material again resulted in an "unstable" grain boundary structure and formation of pores, Figure 7.

4. Gas Analysis

In many systems, pore formation during powder compaction processing is attributed to residual gas. The gas species vary from system to system. In superalloy powder metallurgy, "inert" gases such as argon and helium have been suspected to play a role in pore formation. This avenue was explored by gas analysis of the low carbon IN-100 powder used in the structure studies described above. In addition, a very high temperature, 2270°F, 1 hr., vacuum bake-out was used on the same powder and a normal carbon IN-100 powder before sealing for HIP processing (Run #9, Cans #2D13, 14, and 15, Table III). The HIP compact materials were finally analyzed for gases and the structural response to grain growth heat treatment determined.

Argon content of the R.E.P. powder, 1.6 ppm (Table IV) appears significant considering that argon is <u>not</u> used in the powder manufacturing processing. Powder was handled in air, however, and some adsorption of the $\sim$9400 ppm argon normally in air may have occurred. High temperature outgassing reduced the argon level by an order of magnitude. Structural response to heat treatment was substantially identical to that previously observed for the alloy, Figure 8, (Run #9, Can #2D13, Table II), indicating that "inert" gas, if it influences pore formation, does so at a level of 0.1 ppm or less.

Normal carbon IN-100, degassed, at 2270°F, 1 hr., HIP'ed @ 2270°F, 2 hrs., and heat treated at 2300°F for 2 hrs., showed no sign of unstable grain boundaries or pore formation, Figure 9 (Run #9, Can #2D15, Table II). Carbide spheroidization occurred. The argon level in this material was low, Table IV.

For low carbon IN-100 during grain growth heat treatment at 2270°F, pore formation has been shown to be independent of prior HIP conditions and independent of outgassing treatment (1200°F vs 2270°F). If argon influences pore formation, it does so at a level of 0.1 ppm or less for the low carbon alloy (influence of higher argon levels has not been determined). Carbon at a level of 0.17% prevents pore formation but also prevents grain growth by a carbide pinning mechanism.

5. Extrusions

Five alloy powders were supplied as ~ 1/2" ϕ core extruded rods to Task III. Three extrusions (Mar M 509, C52-06; Cobalt-hafnium, CH6; and Cobalt-hafnium, CH7) were produced from hot isostatically pressed extrusion billets (see Table III). One direct powder extrusion of a Ni-Cr-Al alloy and one direct powder extrusion of low carbon IN-100 were supplied to Task III.

Grain growth heat treatment of the low carbon IN-100 extrusion material produced unstable grain boundaries and pores in short time, Figure 10. Similarity of this structure with those previously described indicates that the structural response of the low carbon IN-100 alloy to grain growth treatment is substantially independent of consolidation method.

III. CONCLUSIONS

In steam atomization, the extent of oxygen pick-up for a given particle size depends critically on metal composition. Quenching rate is too high for liquid metal carbon deoxidation reactions to take place to any significant extent in maraging steel.

The structural response of IN-100 to grain coarsening, required for maximum high temperature strength, is substantially independent of consolidation method, and outgassing technique provided inert gas levels are ~ 1 ppm or less. The main independent variable influencing pore formation and grain growth appears to be carbon level. For .02% carbon pores form at grain boundaries during grain growth. At .17% C grain growth is inhibited by carbide particles and networks. The range of carbon from .02% to ~.15% should be investigated in several steps to determine if high temperature properties can be maximized using a powder metallurgy process route which generates large grain pore free material.

TABLE I

Atomization Runs

Heat No.	Alloy	Atomization Steam, Argon	Nozzles, Pressure Top Pressure	Nozzles, Pressure Side Pressure	Tundish Nozzle	Top Temperature	Objective	Result
233	VM-300 Maraging Steel	S	60 mmg 8 psig	2 1/2 x 100 mmf 10 psig	13/32"	2900°F	Test effect of 1%C addition on oxygen pickup	Coarse rounded powder. Chemistry, see Table II
234	VM-300 Maraging Steel	S	60 mmg 8 psig	2 1/2 x 100 mmf 10 psig	13/32"	2940°F	Test effect of 0.8%C addition on oxygen pickup	Coarse rounded powder. Chemistry, see Table II
235	VM-300 Maraging Steel	S	60 mmg 8 psig	2 1/2 x 100 mmf 10 psig	13/32"	2910°F	Test effect of 0.6%C addition on oxygen pickup	Coarse rounded powder. Chemistry, see Table II
236	VM-300 Maraging Steel	S	60 mmg 8 psig	2 1/2 x 100 mmf 10 psig	13/32"	2940°F	Test effect of 0.4%C addition on oxygen pickup	Coarse rounded powder. Chemistry, see Table II
237	VM-300 Maraging Steel	S	60 mmg 8 psig	2 1/2 x 100 mmf 10 psig	13/32"	2940°F	Test effect of 0.2%C addition on oxygen pickup	Coarse rounded powder. Chemistry, see Table II
238	12% Cr S. S.	S	60 mmg 8 psig	2 1/2 x 100 mmf 10 psig	13/32"	3030°F	Test effect of 12%Cr level on oxygen pickup in 10% Ni S. S.	Coarse rounded powder. Chemistry,

TABLE I (continued)

Atomization Runs

Heat No.	Alloy	Atomization Steam, Argon	Nozzles, Pressure Top Pressure	 Side Pressure	Tundish Nozzle	Top Temperature	Objective	Result
239	18% Cr S.S.	S	60 mmg 8 psig	2 1/2 x 100 mmf 10 psig	13/32"	3050°F	Test Effect of 18% Cr level on oxygen pickup in 10% NiS.S.	Coarse rounded powder. Chemistry, see Table II
240	24% Cr S.S.	S	60 mmg 8 psig	2 1/2 x 100 mmf 10 psig	13/32"	3030°F	Test effect of 24% Cr level on oxygen pickup in 10% NiS.S.	Coarse rounded powder. Chemistry, see Table II
241	Mar M 509	S	60 mmg 8 psig	2 1/2 x 100 mmf 10 psig	13/32"	3025°F	Produce modified composition for hot isostotic pressing and extrusion	Coarse rounded powder. Shells. Chemistry, see Table II

TABLE II

Coarse Powder Chemistry

1. Maraging Steel

Heat No.	Sample Description	Analysis	
233-237	Remelt stock. Mill analysis.	C .018, Si .01, Mn .02, S .005, P .003, Mo 4.78, Co 9.03, Ni 18.51, Al .10, Ti .62, B .003, Zr .010, Ca .05 (added).	
		$\underline{O}$ (ppm)	$\underline{C}$ (wt. %)
233	VM-300. Steam atomized. Water quench. 4 chemical cleaning cycles + HCl etch. -4/+5 mesh.	1300	.97
	Same as above, except -8/+10 mesh	1200	.92
	Same as above, except -16/+18 mesh	1400	.98
	Same as above, except -25/+30 mesh	1600	.91
	Melt dip sample.	740	.99
234	VM-300. Steam atomized. Water quench. 4 chemical cleaning cycles + HCl etch. -4/+5 mesh	1600	.73
	Same as above, except -8/+10 mesh	1500	.72
	Same as above, except -16/+18 mesh	1700	.76
	Same as above, except -25/+30 mesh	1700	.74
	Melt dip sample.	38	.77

TABLE II (Continued)

Heat No.	Sample Description	Analysis	
		O (ppm)	C (wt. %)
235	VM-300. Steam atomized. Water quench. 4 chemical cleaning cycles + HCl etch. -4/+5 mesh	1100	.58
	Same as above, except -8/+10 mesh	1100	.55
	Same as above, except -16/+18 mesh	1700	.55
	Same as above, except -25/+30 mesh	1800	.54
	Melt dip sample.	4	.53
236	VM-300. Steam atomized. Water quench. 4 chemical cleaning cycles + HCl etch. -4/+5 mesh	1400	.37
	Same as above, except -8/+10 mesh	1400	.38
	Same as above, except -16/+18 mesh	1800	.33
	Same as above, except -25/+30 mesh	2000	.33
	Melt dip sample.	5	.42
237	VM-300. Steam atomized. Water quench. 4 chemical cleaning cycles + HCl etch. -4/+5 mesh	960	.17
	Same as above, except -8/+10 mesh	2200	.21
	Same as above, except -16/+18 mesh	2100	.14
	Same as above, except -25/+30 mesh	2000	.15
	Melt dip sample.	9	.16

TABLE II (Continued)

Heat No.	Sample Description	Analysis
238	12% Cr S.S. Nominal comp.	Cr 12%, Ni 10%, Si 1%, C .03%, Fe Bal
		O (ppm)
	Steam atomized. Water quench 3 chemical cleaning cycles.	
	-4/+5 mesh	460
	-8/+10 mesh	900
	-16/+18 mesh	500
	-25/+30 mesh	900
	Melt dip sample.	120
239	18% Cr S. S. Nominal comp.	Cr 18%, Ni 10%, Si 1%, C .03%, Fe Bal
	Steam atomized. Water quench 3 chemical cleaning cycles.	
	-4/+5 mesh	460
	-8/+10 mesh	540
	-16/+18 mesh	560
	-25/+30 mesh	600
	Melt dip sample.	200
240	24% Cr S. S. Nominal comp.	Cr 24%, Ni 10%, Si 1%, C .03%, Fe Bal
	Steam atomized. Water quench 3 chemical cleaning cycles.	
	-4/+5 mesh	430
	-8/+10 mesh	500
	-16/+18 mesh	610
	-25/+30 mesh	610
	Melt dip sample.	260

TABLE II (Continued)

Heat No.	Sample Description	Analysis	
241	Mar M 509, C52-06 Nominal comp.	C 0.8%, Cr 23%, Ni 10%, Ta 5.0%, Zr 0.5%, Ti 0.2%, Si 0.4%, W 9.0%, Co Bal.	
		O (ppm)	C (Wt. %)
	Coarse powder. 3 cycles chemical cleaning plus inhibited aqua regia -3 1/2 mesh	400	0.75%

TABLE III

Hot Isostatic Pressing Runs

No.	Can No.	Powder	Billet Size at Start	Pressing Conditions	Remarks
1	2A18, 2A19	IN-100, Low carbon Nuclear Metals R.E.P. Lot No. 6140, -35 mesh	7/8" ϕ x 13"	2050°F, 28,700 psi, 2 hrs.	Outgassing of all cans @ 1200°F unless noted. .02% C
2	2A15, 2A17	IN-100, Low carbon Nuclear Metals R.E.P. Lot No. 6140, -35 mesh	7/8" ϕ x 13"	2100°F, 28,700 psi, 2 hrs.	
2	2A38	IN-100, Low carbon Cartech Lot No. A00080, -80 mesh	7/8" ϕ x 13"	2100°F, 28,700 psi, 2 hrs.	
3	2A16, 2A20	IN-100, Low carbon Nuclear Metals R.E.P. Lot No. 6140, -35 mesh	7/8" ϕ x 13"	2250°F, 27,600 psi, 2 hrs.	
3	2A39	IN-100, Low carbon Cartech Lot No. A00080, -80 mesh	7/8" ϕ x 13"	2250°F, 27,600 psi, 2 hrs.	
4	2A36, 2A32	IN-100, Low carbon Nuclear Metals R.E.P. Lot No. 6140, -35 mesh	7/8" ϕ x 13"	2150°F, 28,700 psi, 2 hrs.	
5	2A31, 2A37	IN-100, Low carbon Nuclear Metals R.E.P. Lot No. 6140, -35 mesh	7/8" ϕ x 13"	2000°F, 29,000 psi, 2 hrs.	

TABLE III (Continued)

No.	Con No.	Powder	Billet Size at Start	Pressing Conditions	Remarks
6	2A14, 2A21	IN-100, Low carbon Nuclear Metals R.E.P. Lot No. 6140, -35 mesh	7/8"ϕ x 13"	2150°F, 28,300 psi, 2 hrs.	
7	2A33, 2A34, 2A42	IN-100, Low carbon Nuclear Metals R.E.P. Lot No. 6140, -35 mesh	7/8"ϕ x 13"	2275°F, 28,300 psi, 2 hrs.	
	2B25	Co-Hf casting	1/4" x 1/4" x 5"	2275°F, 28,300 psi, 2 hrs.	
8	2D16	Co-Hf Alloy, CH6. Homogeneous Metals	3 1/4"ϕ x 12"	2300°F, 26,500 psi, 4 hrs.	Extrusion billet.
	2D17	IMT 30-225, -3 1/2 mesh	Small pieces	2300°F, 26,500 psi, 4 hrs.	Re-HIP of pieces of 6"ϕ hot work HIP billet #1 H 28
9	2D13, 2D14	IN-100, Low carbon Nuclear Metals R.E.P. Lot No. 6140, -35 mesh	3/4"ϕ x 7 3/8"	2270°F, 28,700 psi, 2 hrs.	Canned in INCO 600. Outgassed @ 2270°F, 1 hr. before vacuum sealing.
	2D15	IN-100, Normal carbon Nuclear Metals R.E.P. Lot No. 4521, -35 mesh	3/4"ϕ x 7 3/8"	2270°F, 28,700 psi, 2 hrs.	Canned in INCO 600. Outgassed @ 2270°F, 1 hr. before vacuum sealing. .178%C

TABLE III (Continued)

No.	Can No.	Powder	Billet Size at Start	Pressing Conditions	Remarks
10	2A30, 2A35	IN-100, Low carbon Nuclear Metals R.E.P. Lot No. 6140, -35 mesh	7/8"ϕ x 13"	2325°F, 1 hr. + 2270°F, 1 hr. + 2325°F, 1 hr., + 2270°F, 1 hr. 28,300 psi	
	2D13 2D15	See run #9 above	3/4"ϕ x 7 3/8"	2325°F, 1 hr. + 2270°F, 1 hr. + 2325°F, 1 hr., + 2270°F, 1 hr. 28,300 psi	Re-HIP of material from run #9.
	2E18	Co-Hf alloy, CH7 Homogeneous Metals	3 1/4"ϕ x 12"	2325°F, 1 hr. + 2270°F, 1 hr. +2325°F, 1 hr., +2270°F, 1 hr. 28,300 psi	Extrusion billet.
	2E19	Mar M 509 "75 - 76"	Assorted Small Pieces	2325°F, 1 hr. + 2270°F, 1 hr. +2325°F, 1 hr., +2270°F, 1 hr. 28,300 psi	Re-HIP of pieces of 6"ϕ hot work HIP billet.
11	2E44	Mar M 509, IMT 30-241 -3 1/2/+30 mesh. C 52-06	3 1/4"ϕ x 12"	2300°F, 28,300 psi, 2 hrs.	Extrusion billet.

TABLE IV

Gas Analysis

No.	Sample Description	Vacuum Fusion - Mass Spec. Readout Analysis, ppm				
		N	O	H	He	Ar
1.	Low carbon, IN-100 R.E.P. powder Lot No. 6140, -35 mesh. Cannon Muskegon Ht. No. VE-383.	14	130	7.5	N.D., 0.1*	1.6, 0.5*
2.	Low carbon, IN-100 R.E.P. powder Can No. 2D13, Table III. Degas @ 2270°F, 1 hr. seal, HIP @ 2270°F, 2 hr.	36	170	10	----------	0.1, < 0.1*
3.	Normal carbon, IN-100 R.E.P. powder Can No. 2D15. Table III. Degas @ 2270°F, 1 hr., seal, HIP @ 2270°F, 2 hr.	28	89	14	----------	N.D., < 0.1*

* Detectability limit of analysis.

N.D. Not detected.

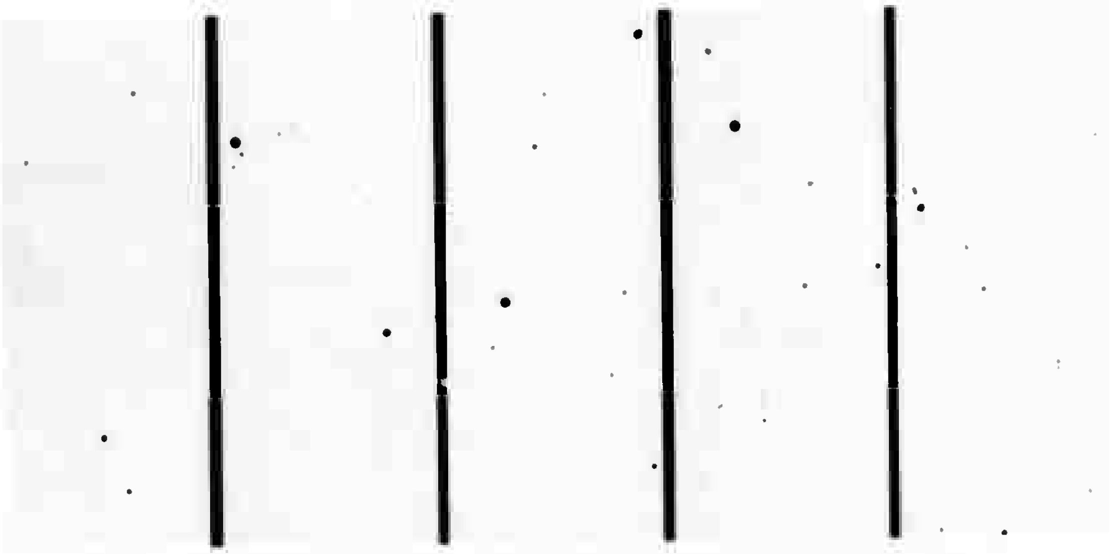

Figure 1. Maraging Steel VM-300. Steam atomization. L to R, Ht. Nos. 233 (1%C), 234 (0.8%C), 235 (0.6%C), 236 (0.4%C), 237 (0.2%C). -25/+30 mesh. Oxide inclusions. Unetched. 500X.

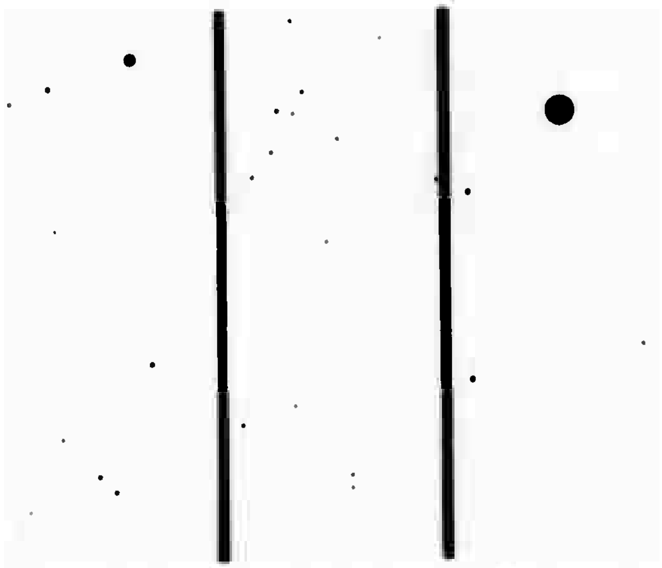

Figure 2. Stainless Steels. Steam atomization. L to R., Ht. Nos. 238 (12% Cr), 239 (18% Cr), 240 (24% Cr). -25/+30 mesh. Oxide inclusions. Unetched. 500X.

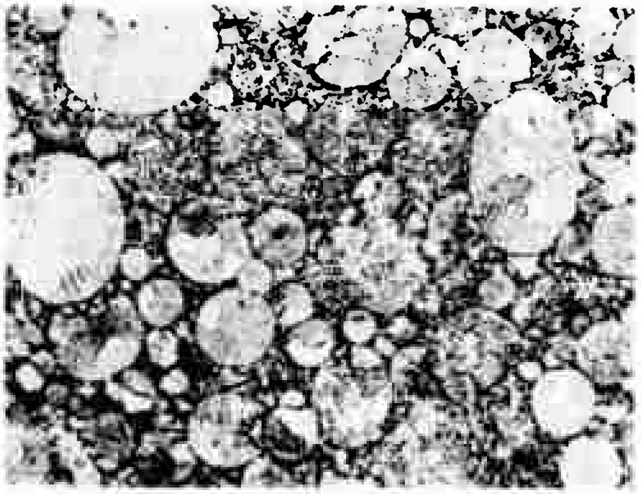

Figure 3

IN-100, low carbon, R.E.P. powder. -35 mesh. HIP @ 2000°F, 29,000 psi, 2 hrs. As pressed. Etched. 100X

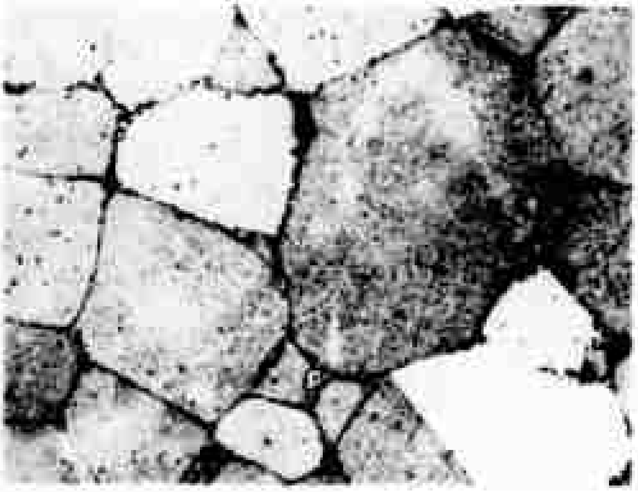

Figure 4

Same material as Figure 3 plus 2275°F, 2 hrs. A.C. Etched. 100X

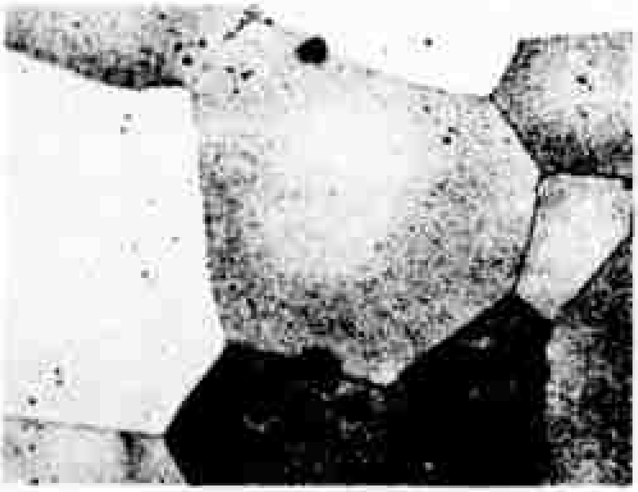

Figure 5

Same material as Figure 3 plus 2275°F, 5 hrs. A.C. Etched. 100X.

Figure 6. IN-100, low carbon, R.E.P. powder, -35 mesh. HIP @ 2275°F, 28,300 psi, 2 hrs. As pressed. Etched. 100X.

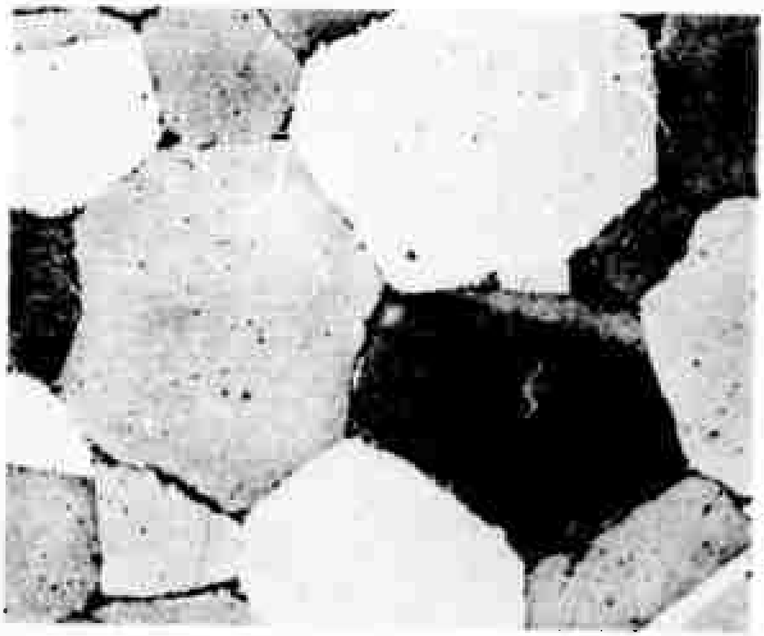

Figure 7. Same material as Figure 6, plus 2275°F, 1 hr. A.C. Etched. 100X.

Figure 8

IN-100, low carbon, R.E.P. powder, -35 mesh. Outgassed @ 2270°F, 1 hr. before vacuum sealing. HIP @ 2270°F, 28,700 psi, 2 hrs. + H.T. 2300°F, 2 hrs. A.C. Etched. 100X.

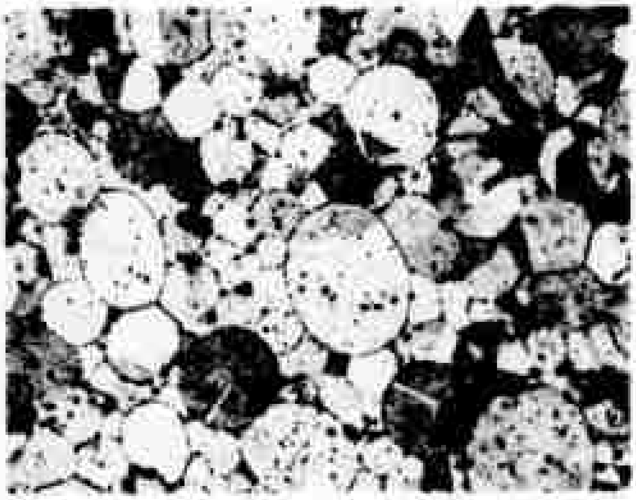

Figure 9

IN-100, normal carbon, R.E.P. powder, -35 mesh. Outgassed @ 2270°F, 1 hr. before vacuum sealing, HIP @ 2270°F, 28,700 psi, 2 hrs. + H.T. @ 2300°F, 2 hr. A.C. Etched. 100X.

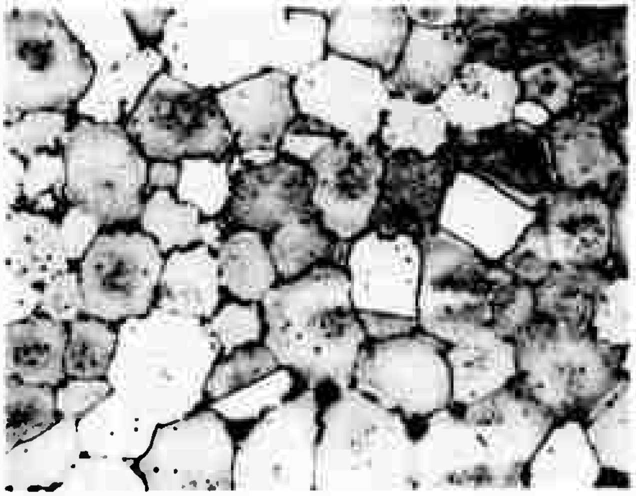

Figure 10

IN-100, low carbon, R.E.P. powder, -35 mesh. Extruded @ 2075°F, 25X + H.T. 2270°F, 15 min. A.C. Etched. 100X.

TASK II

Solidification Research

D. Apelian

R. Mehrabian

M.C. Flemings

I. INTRODUCTION

In this part of the program, a new process for atomization of metal powders was developed. The process, called "filatomization," entails atomization of an alloy melt by forcing it through porous ceramic filters.

Of all the various powder manufacturing processes available this particular process of filatomization is unique for various reasons: (i) filtration of undesired oxide and foreign particles occurs simultaneously with powder drop formation, (ii) the required experimental apparatus is not complicated--an attractive economic advantage, (iii) fairly spherical metal powders are produced, thus minimizing the surface area to volume ratio, and (iv) control of powder size is governed by the filters used.

A series of experiments, using pure aluminum and a 7075 aluminum alloy, were conducted to investigate the governing parameters for the production of metal powders by filatomization. The independent variables in this series of experiments were:

1. Filter material pore size
2. Temperature at which filatomized
3. Mode of pressure application
4. Geometry of setup and charge composition.

The effect of the above on the following dependent variables was investigated:

1. Required pressure
2. Size and distribution of powders formed
3. Fraction of melt successfully filatomized
4. Microstructure of metal powders
5. Mechanical properties of billets made by cold compaction and subsequent hot extrusion of the 7075 alloy powders.

II. APPARATUS AND PROCEDURE

A. Apparatus

An apparatus previously used in filtration studies of aluminum alloys was redesigned to carry out the experiments outlined in the previous section. A schematic of the apparatus for the production of metal powders through filters is shown in Figure 1. The overall experimental setup is shown in Figure 2.

The apparatus consists of a pressure vessel within which a graphite crucible is placed containing the metal charge and a filter assembly located below the charge. The crucible is covered with an insulating shield made out of fiberfrax. RF induction heating is employed within the chamber. The chamber is 10" in diameter by 8" high. This chamber is placed at a height of 7 to 8 feet to allow a long enough freefall distance for the metal powders to solidify. The liquid metal, which is melted in situ, is filatomized by pressuring the chamber with an inert gas.

The filter media employed (sintered discs of alumina or quartz) is completely contained within a graphite filter assembly, which in turn is mounted in the crucible with a taper fit. Hence, pressurization of the top of the melt forces liquid metal down through the filter, Figure 1.

Other specific features of the assembly shown in Figures 1 and 2 include the following:

1. A safety valve is located on top of the chamber.
2. An inflow and outflow valve, incorporating a pressure gauge is located on top of the chamber.
3. The chamber is connected to a vacuum pump through a 1/2 inch diameter pipe.
4. Watercooled feedthroughs for the RF coils are located on the side of the chamber. These are teflon insulated to electrically isolate the vessel from the RF coils.
5. A thermocouple feedthrough is located on the side of the chamber to permit measurement of the melt temperature.

A tapered graphite crucible was designed and machined as shown in Figure 1. The crucible is mounted on the base of the vessel by six stainless steel bolts utilizing an asbestos insulating gasket. With this construction, upon pressurization, the crucible is under pressure from all sides except the bottom, and a pressure differential is set within the crucible between the melt and the lower chamber.

The copper coils for the RF heating are arranged so that a uniform temperature profile exists along the entire length of the filter container assembly.

The particular design advantages of this apparatus are:

1. Accurate temperature control before and during filatomization is possible.
2. The vessel may be pressurized gradually or instantaneously, while the pressure differential is measured continuously.
3. Potential leakage problems around the crucible may be detected before the actual filatomization operation.

B. Production Procedure

The filter was mounted within the filter container assembly shown in Figure 1. The spherical drops (powders) exiting from the filter were exposed to the atmosphere; no inert gas was injected at the exit port. The powders were collected in a can located 5 feet below the filter thus allowing them to completely solidify before reaching the collector can. Sintered Al_2O_3 porous disc filters of 87-100μ and 31-36μ pore sizes and sintered quartz discs of 90-150μ and 40-90μ pore sizes were used. The alloys used for filatomization were 99.99% Aluminum and 7075 alloy of Al-7.3% Zn - 3.2% Mg-2% Cu -.25% Cr nominal composition. The 7075 alloy was prepared using pure zinc and magnesium, 99.99% Al, Al-50% Cu master alloy and an Al-20% Cr master alloy. The melt was degassed with chlorine prior to pouring.

The operational procedure for the following experiments was to melt about 200 grams of the alloy in a nitrogen atmosphere and superheat it to 800°C. The power was then gradually decreased reducing the melt temperature to a predetermined level, T_F. The pressure above the melt was gradually increased until metal drops (powders) started to exit from the filter. The procedure employed and the temperatures and pressures used are listed in Table I. Size distribution curves of the resulting powders obtained from the various filters were determined by sizing (sieve analysis) and weighing of the powders.

The remnant metal above the filter (metal which did not go through the filter), the powders and flakes produced, and the filter itself were all metallographically examined. Keller's etch was used for the microstructural investigation of the powders. Macroexamination of the powders and flakes was done by scanning electron microscopy. The Al_2O_3 content of the powders, flakes and the remnant metal above the filter was determined by chemical analysis. Powders made by this process were compared with 7075 commercial powders (made by centrifugal atomization) purchased from Reynolds Aluminum, and 7075 alloy of nominal composition, Al-7.5% Zn-2.4% Mg-1.0% Cu-0.2% Cr-1.1% Fe-1.0% Ni, splat cooled by J. P. Durand(1).

C. Classification and Processing of Powders

Pound lots of filatomized spherical powders and flakes were produced using various filters as described above. No particular powder or flake size was selected for the extrusion process, but rather all the filatomized spherical powders were mixed carefully and used for the extrusion. The size distribution of these powders was measured and calculated. The same was done for the filatomized flakes. The filatomized powders, filatomized flakes, commercial 7075 powders*, and the splat cooled 7075 flakes** were all cold compacted under 20,000 psi pressure into two 3 inch O.D. by 2 inch I.D. 6061-T6 aluminum cans. The location of the various powders and flakes in the cans was carefully noted for reference. The above were compacted to 70% density. The top caps of the cans were then welded on, and the cans were leak checked before evacuation.

The extrusion billets were evacuated at the solutionizing temperature of the alloy. For the filatomized powders and flakes and the Reynolds' powders a solution temperature of 476.2°C was employed. The

---

*Purchased from Reynolds.

**Made by J. P. Durand (1).

billets were heated under vacuum for 2 hours to reach the solution temperature, held at that temperature for an additional hour and furnace cooled. The billets were then sealed, soaked at 300°C for 4 hours and extruded at 300°C at a reduction ratio of 20 to 1. The extruded rods had a final diameter of 0.67" and a core diameter of 0.41".

The extruded rods were then machined down to the core diameter. Ten 0.75" long samples were cut from each extruded rod, and the solution temperature and ageing kinetics of the alloys were studied. All the solution treatments were given in an air furnace equipped with automatic control. Artificial ageing was done at 121°C (250°F) for various times.

D. Mechanical Testing

Tensile tests on all materials were performed with a standard 1/4 - 20 thread tensile specimen, with a 1.0" gauge length and 0.16" diameter. Several test specimens were machined from each billet. These specimens were then radially and longitudinally polished on a lathe with #600 emery paper. After cleaning in Acetone, the specimens were again radially polished on a lathe with wenol metal polish. All tensile tests were run on an Instron machine at a constant crosshead speed of 0.05 inch per minute. The elongation, reduction in area, yield strength and ultimate tensile strength were measured. Finally, the fractured surfaces of the tensile specimens were studied by scanning electron microscopy.

III. RESULTS AND DISCUSSION

A. Powder Formation

Experiments carried out in production of powders of pure aluminum and a modified 7075 alloy by filatomization have been summarized in Table I. The different variables (i.e., temperature, filter media, pressures, etc.) for each experiment are also listed in Table I.

Various size spherical powders made in Runs #1 and #18 are shown in Figure 3. Occasionally, liquid streams exiting from adjacent pores coalesced to form large liquid metal drops. Large drops thus formed did not completely solidify in flight and "splatted" in the collector container, forming flakes, Figure 3(e).

SEM view of spherical metal drops (powders) emerging from the pores of a sintered Al_2O_3 disc, with an average pore size of 87-100μ, is shown in Figure 4(a). The neck region of one of the powders is shown in Figure 4(b). The exiting stream of liquid metal becomes spherical in shape due to surface tension forces, and subsequently drop detachment occurs. Hauser and Edgerton(2) have investigated the steps of formation and detachment of drops from the end of vertical tubes. They show that a waist forms first and rapidly necks down into a stem which then breaks off close to the top of the drop. Harkins and Brown(3) have derived an expression for drop formation using a force balance between gravity and surface tension:

$$mg = \pi d \sigma f \left(\frac{d}{V^{1/3}} \right) \qquad (1)$$

where

mg = weight of drop

d = tip or orifice diameter

σ = surface tension

V = drop volume

$f \left(\frac{d}{V^{1/3}} \right)$ = an empirical correction factor that takes into account the shape of the drop. In case of an ideal spherical drop the value of this function becomes unity.

This type of analysis does not take into account formation of an oxide layer, solidification, or large temperature gradients that exist below the filter in filatomization.

A large number of available pores in the bottom of the filter are not utilized during drop (powder) formation, Figures 5(a) and (b). Liquid metal preferentially flows through paths of least resistance, causing a channeling phenomenon to occur. Increasing filatomization pressures leads to utilization of a greater number of pores, which in turn can cause consolidation of drops from adjacent pores (i.e., less than one drop diameter apart), Figures 5(c). In the extreme case, consolidation of many liquid drops results in formation of large drops which do not completely solidify in flight and splat against the collection container forming the flakes shown in Figure 3(e).

There is a correlation between superheat and size of drops (powders) forming when Al_2O_3 filters are used. Figures 6(a) and 6(b) show size distributions of the resulting powders from Run #11 (T_F=700°C) and Run #16 (T_F=742°C), respectively. A higher percentage of larger particles forms with increasing superheat, within the temperature ranges studied.

It was found that Al_2O_3 filters were more amenable to filatomization than the SiO_2 filters. SiO_2 filters of 90-150μ pore size were used in Run #8 (T_F=769°C) and Run #9 (T_F=650°C). In both runs large drops of the 7075 alloy were formed, which in turn splatted against the collection container below. Size distribution analysis of spherical drops formed through an SiO_2 filter, Run #4 (T_F=769°C) is shown in Figure 7(a).

Liquid aluminum wets SiO_2 much more readily than it does Al_2O_3⁽⁴⁾. Hence, in cases where drops of metal consolidate below the filter, large drops can easily spread out on the SiO_2 filters, leading to formation of the flakes described above. It is also possible that in SiO_2 filters the molten aluminum penetrates through more pores (i.e., less channeling occurs). This in turn would result in increased consolidation of drops, subsequent spreading, and thus formation of large drops.

Pressure control is an important variable for successful filatomization. Surpassing the critical pressure (the one required for drop formation through preferential channels) results in the formation of continuous and consolidated streams. Keith and Hixson(5) investigated the effect of pressure and flow rate on formation of drops at the tip of a vertical tube, Figure 7(b). At low flow rates, drops form individually at the pore tip and grow in size until the weight overcomes the interfacial tension and drop detachment occurs. This mechanism pertains to filatomization.

With increasing flow velocities, a point is reached where a very short continuous neck of liquid exists between the pore tip and the point of drop detachment. This velocity is called the jetting point. At high flow rates, the jet breakup point retreats to the pore tip and a nonuniform spray of drops results--point of atomization.

One of the attractive features of filatomization is that filtration and drop (powder) formation occur simultaneously. Figure 8(a) shows the oxide "cake" retained above the sintered SiO_2 disc filter, Run #4. Figure 8(b) shows the oxide skins connected with porosity found above the sintered Al_2O_3 disc filter employed in Run #16. It should also be possible to filter out undesirable secondary phases (exogenous inclusions) from a melt prior to powder formation.

The filter used in Run #14 had also been used in the four preceeding runs. Size distribution of powders obtained from Run #14 (T_F=742°C) and Run #16 (T_F=742°C, new filter) are shown in Figures 9 and 6(b) respectively. In Run #14, a larger percentage of -16+20 and -20+30 mesh powders were formed. Clogging of the interstices occurs as a filter is used successively, leading to liquid flow through other finer pores and resulting in the formation of finer powders. In Run #14 slightly larger pressures were required for flow of liquid metal (Δp for fine pores > Δp for large pores).

B. Structure of Filatomized and Commercial Powders

1. Spherical Powders

Figures 10(a) and 10(b) show SEM views of 300μ and 150μ size range pure aluminum powders obtained in Run #1. The powders are generally spherical in shape. Occasionally powders with stems or tips not completely detached were also observed, Figure 11(a). At a higher magnification, surface irregularities such as ripples, folds, and waves are observed, Figure 11. These are caused when the initial oxide layer tries to accommodate deformation experienced by the drop as solidification, shrinkage, and flight instabilities occur. Figure 10(c) shows a representative microstructure of the pure aluminum powders obtained in this study.

Filatomized spherical powders made from a modified 7075 aluminum alloy varied in their structure. Two distinct types of spherical powders were observed, Type (i) powders possessed a fine dendritic structure, and Type (ii) powders had no apparent dendritic structure.

Figure 12 shows SEM view of Type (i) powders. These are representative structures of the filatomized powders cold compacted and hot extruded into a billet. The different dendritic microstructures of these powders are shown in Figure 13. There is no evidence of porosity here, and the measured dendrite arm spacings were between 4-8μ, indicating cooling rates ranging from 10^2 to 10^4°C/sec.(6)

Figure 14(a) shows an SEM view of a Type (ii) 7075 aluminum alloy powder. This powder has a smooth surface with no apparent dendritic structure, and contains second phase particles that have precipitated throughout the structure. The microstructure of these powders are shown in Figures 14(b) and (c). It can be seen that what appears to be a fine dendritic structure at low magnifications, Figure 14(b), is really a distribution of second phase particles within the matrix, Figure 14(c). The absence of dendritic structures is due to the higher cooling rates experienced by these smaller Type (ii) powders. Some of the Type (ii) small powders (25-50μ diameter) have oscillatory nodes around their circumference, Figure 15. These particular powders are attached to each other by a cup-like layer. This may be due to collision and subsequent attachment during flight of two or more drops; the surface ridges being caused by aerodynamic rippling.(7)

The filatomized spherical powders reported above were chemically analyzed, and the Al_2O_3 content ranged between .07 - .12 wt. %.

2. Flakes

Figure 16(a) shows an SEM view of the fine dendritic structure on a filatomized flake of 7075 aluminum alloy. The dendrite arm spacings of the flakes ranged between 2-4μ, corresponding to relatively high cooling rates of 10^4 - 10^5°C/sec.(6)

The flakes generally have a "duplex" structure composed of fine and coarse dendrites, Figure 16(b). The coarse dendrites form during the flight of a large drop, while the higher cooling rates experienced by the drop upon "splatting" against the collector can result in the finer structures.

The Al_2O_3 content of the filatomized flakes, determined by chemical analysis, ranged between .15-.57 wt. %. As expected, the flakes had a much higher oxide content because of the large surface area to volume ratio.

3. Commercial 7075* Powder

SEM views of 7075 aluminum alloy powders produced by a centrifugal atomizer are shown in Figures 17(a) and (b). The powders are acicular in shape and are enveloped by a thick oxide layer. The shape of these powders is quite heterogeneous, and their size varies from 1 mm to 5 mm.

The microstructure of the powders is shown in Figures 17(c) and (d). Excessive porosity resulting from the atomization process is evident. Measured dendrite arm spacings are of the order of 7-8μ, corresponding to cooling rates of 5×10^2 to 10^3°C/sec.(6) Comparing the microstructures of these powders with those of the filatomized powders, Figure 13, the superiority of the latter both in lack of porosity and fineness of structure is evident.

*Obtained from Reynolds.

C. Processing and Structure of 7075 - T6 Extrusions

1. Processing

The filatomized spherical powders and flakes of the 7075 aluminum alloy were cold compacted and hot extruded into two separate billets. The spherical powders ranged in size from 100μ to 2000μ and were obtained with the Al_2O_3 filters. The filatomized flakes, 5-10 mm in length and 120-500μ thick, were obtained with the SiO_2 filters.

Extrusion billets of the filatomized and commercial powders, and a commercial bar of 7075 aluminum alloy were made under conditions shown in Table II. All powder compacts except sample D, Table II, were preheated to 475°C to 490°C for 1 hour to lower gas content of the compact and prevent subsequent blistering and delamination during solution heat treatment.(8) All the billets were soaked at 300°C for 4 hours and extruded at a reduction ratio of 20 to 1.

The transverse and longitudinal microstructures of the as-extruded spherical filatomized powders are shown in Figures 18(a) and (b), respectively. The structure is fibrous with no observable porosity. Hardness measurements along the transverse (average R_B = 30.18) and longitudinal (average R_B = 44.78) surfaces differed consistently due to the texture developed during the extrusion. Figures 18(c) and (d) show the same structures at a higher magnification, the second phase particles are aligned along the extrusion axis.

The transverse and longitudinal microstructures of the as-extruded filatomized flakes are shown in Figures 19(a) and (b), respectively. The structure is again fibrous with definite evidence of porosity. Figures 19(c) and (d) show the transverse and longitudinal microstructures of extruded commercially produced 7075 aluminum alloy powders.

All of the 7075 extrusions were heat treated to a T6 condition, which consists of a solution heat treatment to maximize the solid solubility of the alloying elements and artificial ageing to cause precipitation.

Samples of the extruded billet (filatomized spherical powders) were heat treated for various times and temperatures to determine the optimum solutionization temperature. Peak aged condition was determined by following the solution heat treatment with natural ageing for 24 hours and artificial ageing at 129°C for 24 hours. A solution heat treatment of 2 hours at 475°C was found to maximize solid solubility of the alloying elements as shown in Figure 20. Also, the best hardness values were obtained for this solution treatment followed by the ageing condition reported above, Table III.

Billets of the commercial powder and bar material, with a nominal composition of Al-5% Zn-1.45% Cu-2.7% Mg-0.17% Cr, were solution heat treated for 2 hours at 460°C. This heat treatment has been recommended by earlier workers.(9,1)

Billet E (Table II) was made from splat cooled flakes with a nominal composition of Al-7.5% Zn-2.4% Mg-1.0% Cu-0.20% Cr-1.1% Fe-1.0%Ni, and was included here for comparison.

2. Structure

The structure of the commercial 7075 - T6 billet F, (Table II), is shown in Figure 21(a). Large and well defined grains with a distribution of coarse (8-10μ) second phase particles are seen. The transverse microstructures of extruded 7075 - T6 powders are shown in Figures 21(b) - (d). Figures 21(b) and (c) show the structures from billets D and C, (Table II), respectively. The marked difference in porosity content of the two billets can be related to the preheat treatment given to the powders of billet C.(8) Structure of extrusion of filatomized flakes, billet B, is shown in Figure 21(d). Finally, the transverse and longitudinal microstructures of the extrusion made from filatomized spherical powders, billet A, (Table II), are shown in Figure 22.

It can be seen that the spherical filatomized powders which possess a minimum surface area to volume ratio, (i.e., minimum amount of oxide and surface contaminants) and have favorable packing characteristics, gave the soundest extrusion billet.

The porosity observed in extrusions of Figure 21 occurs during solution heat treatment followed by quenching and is caused by the gas content of the extrusion. The gas present is predominantly hydrogen dissolved or adsorbed during the atomization process (from H_2O and hydrates on surface of powders) and subsequent handling. The hydrogen remaining after the extrusion is (i) dissolved in the matrix, and/or (ii) adsorbed at grain boundaries and original pore sites. Upon quenching, the solubility of the gas is suddenly decreased markedly, causing the formation of gas pockets between the grains.

D. Mechanical Properties

The room temperature longitudinal tensile properties of the 7075 - T6 extrusions are given in Table IV. The values listed are average values from multiple tests. All tests were run at a cross-head speed of 0.05 inch/minute. The following observations can be made from Table IV:

(i) The highest reduction in area (42.4%) and elongation (15.1%) values were obtained in the extrusion made from filatomized spherical powders.

(ii) The best corresponding values for the extruded billet made of commercial powders were 11-14% and 7-9%, respectively.

(iii) The 7075 - T6 extrusion made of round bar stock had a slightly higher yield stress, but lower ductility than the filatomized powder extrusion.

(iv) The filatomized flake and splat cooled flake extrusions had relatively lower ductilities. However, the extrusion of splat cooled flakes had the highest strength properties.

Figure 23(a) - (c) show SEM fractographs of the 7075 - T6 extrusion of filatomized spherical powders, billet A, (Table II). The fracture is ductile without any delaminations, Figure 23(a), with the second phase particles attached to the ductile voids, Figures 23(b) and (c). Figure 23(d) - (f) show SEM fractographs of the 7075 - T6 extrusion of the filatomized flakes, billet B, (Table II). Severe delaminations associated with porosity are observed. Figures 23(e) and (f) are high magnification fractographs of a ductile region and surface of the delaminations, respectively.

SEM fractographs of the 7075 - T6 extrusion of commercial powders, billet C, (Table II), are shown in Figures 24(a) - (c). Delaminations accompanied by large regions that have fractured in a ductile manner are shown in Figure 24(b). Second phase particles which have remained within the voids are shown in Figure 24(c).

SEM fractographs of the 7075 - T6 extrusion of splat cooled flakes, billet E (Table II), are shown in Figures 24(d) - (f).

Figure 24(d) shows few delaminations accompanied by large regions fractured in a ductile manner. The fibrous nature of the delamination wall, and the fine constituent second phase particles within the voids are shown in Figures 24(e) and (f), respectively.

The filatomized spherical powders and flakes had undergone the same thermomechanical processing. However, the properties obtained differ markedly due to the oxide content and morphology of these powders. More specifically:

(i) The flakes have a higher surface area to volume ratio, and thus a higher oxide content.

(ii) During compaction, the surface oxide on the walls of the flakes causes weak bonding. The poor bonding of the oxide walls accompanied with longitudinal porosity, caused by the heat treatment, results in coarse fibrous delaminations.

(iii) Spherical powders pack more efficiently than do the flakes, sinter more completely, and contain a lower amount of porosity.

The superior ductilities measured in the extrusions made from filatomized spherical powders can be attributed to removal of oxide particles during "filatomization" and to the spherical morphology of the powders.

E. Summary

Pure Al and 7075 powders of spherical and flake morphology were made using Al_2O_3 and SiO_2 filters with 40-150μ pore size ranges. The range of metal drops forming below the filter is governed by (i) pore size and composition of the filter material, (ii) the temperature of filatomization, and (iii) the applied pressure.

(i) Channeling within the filter permits formation of drops without consolidation of the emerging streams. The extent of wetting between the liquid metal and the filter employed is important.

(ii) Size range of powders is influenced by the amount of superheat in the melt. Increasing superheat results in formation of larger drops.

(iii) The pressure range required for filatomization (i.e., 2-6 psi) can easily be accommodated by a hydrostatic head on the melt.

An alternative method is one where the area below the filter is exposed to a partial vacuum. One attractive aspect of this process is that filtration of undesirable second phases and oxides occurs simultaneously with powder formation. In all the experiments reported herein, aluminum oxide skins and "cakes" were found immediately above the filter. An alternative process is one in which filtration is combined with inert gas atomization. In this process, higher pressures would be employed to form consolidated metal streams below the filter. One or more inert gas jets directed toward the exiting liquid metal streams would then cause atomization.

The microstructures of the spherical powders produced by filatomization were found to be superior to the commercially produced powders, in particular, for their lack of porosity, fineness of structure, favorable morphology, and low oxide content. As a consequence, the extruded billet of this powder had a comparable strength and a much higher ductility than all other extrusions used in this study.

IV. CONCLUSIONS

1. A new process for production of powders of metal alloys was developed. The process called "filatomization" combines filtration of oxides and undesirable second phases with atomization of the melt.

2. Pure aluminum and a 7075 aluminum alloy were filatomized through sintered Al_2O_3 and SiO_2 disc filters with average pore sizes in the range of 40 to 150μ. The Al_2O_3 filters were found to be more amenable to filatomization of these alloys than the SiO_2 filters.

3. The size range of metal drops forming below the filter is governed by; (i) pore size and composition of the filter material, (ii) the temperature of filatomization, and (iii) the applied pressure.

4. The microstructures of the filatomized spherical powders of the 7075 alloy were superior to the commercially produced powders. The filatomized powders were free of porosity, had a fine microstructure with measured DAS values between 4-8μ, had low oxide contents.

5. Filatomized spherical powders and flakes, commercial powders, splat cooled flakes, and a 7075 commercial bar stock were all extruded into billets. After a T6 temper treatment, the microstructure of the extruded spherical filatomized powders was superior to all the others.

6. The longitudinal room temperature tensile properties of the 7075 - T6 filatomized spherical powder extrusion were; Y.S.--80,000 psi, U.T.S.--94,300 psi, R.A.--42.4%, and Elongation--15.1%. The corresponding values for the commercial powder extrusion were; Y.S.--75,000 psi, U.T.S.--87,300 psi, R.A.--11.5%, and Elongation--7.8%.

V. REFERENCES

1. Jean-Pierre Durand: "Properties of Splat Cooled 7075 Aluminum Alloys," M.S. Thesis, Massachusetts Institute of Technology, August, 1972.

2. E. A. Hauser, H. E. Edgerton, B. M. Holt and J. T. Cox, Jr., J. Phys. Chem., Vol. 40, (1936) p. 973.

3. W. D. Harkins, F. E. Brown, J. Am. Chem. Soc., Vol. 41 (1919) p. 499.

4. W. D. Kingery, J. of the Amer. Ceramic Soc., Vol. 37 (1954) p. 44.

5. F. W. Keith, A. N. Hixson, Ind. Eng. Chem., Vol. 47 (1955) pp. 258.

6. H. Matyja, B. C. Giessen, N. J. Grant, J. Inst. Metals, Vol. 96 (1968) p.30.

7. Professor C. S. Smith, M.I.T. -- private communications.

8. J. P. Lyle, W. S. Cebulak, "Fabrication of High Strength Aluminum Products from Powder," presented at the 18th Sagamore Army Materials Research Conference: Powder Metallurgy for High Performance Applications, September, 1971.

9. H. Y. Hunsicker, "The Metallurgy of Heat Treatment," Aluminum, Vol. 1, ASM, Metals Park, Ohio, 1967.

TABLE I

LIST OF FILATOMIZATION EXPERIMENTS

Run #	Sintered Filters Used	T_F	Alloy Used	Pressure Applied psi
1	Al_2O_3, 87-100μ, .5" opening	710°C	99.99% Al	7-8 then lowered to 4-5
2	Al_2O_3, 31-35μ, .75" opening	840°C	7075	7-14
3	SiO_2, 90-150μ, .75" opening	756°C	7075	2-4 and 10-15
4	SiO_2, 90-150μ, .75" opening	769°C	7075	10-12
5	Al_2O_3, 87-100μ, .75" opening	756.5°C	7075	3-5
6	Al_2O_3, 87-100μ, .75" opening previously infiltrated	732.5°C	7075	3-5
7	Al_2O_3, 87-100μ, .75" opening	760°C	7075	3-5
8	SiO_2, 90-150μ, .75" opening	769°C	7075	2-4 and 10-14
9	SiO_2, 90-150μ, .75" opening	650°C	7075	3-4
10	Al_2O_3, 87-100μ, .5" opening	697°C	7075	0-6
11	Al_2O_3, 87-100μ, .5" opening previously infiltrated	700°C	7075	5-6
12	Al_2O_3, 87-100μ, .5" opening previously infiltrated	721°C	7075	5-6
13	SiO_2, 90-150μ, .5" opening	685°C	7075	3-5
14	Al_2O_3, 87-100μ, .5" opening same filter as in runs # 10-12	742°C	7075	5-6
15	Al_2O_3, 87-100μ, .5" opening	742°C	7075	0-7
16	Al_2O_3, 87-100μ, .5" opening previously infiltrated, filter from run #15	742°C	7075	4-5
17	Al_2O_3, 87-100μ, .5" opening	700°C	99.99% Al	7, then lowered to 4-5
18	SiO_2, 40-90μ, .5" opening	687°C	7075	2-4
19	Al_2O_3, 87-100μ, .75" opening	700°C	99.99% Al	7, then lowered to 4-5

TABLE II

PROCESSING OF 7075 - T6 EXTRUSIONS

Billet Designation	Starting Material	Treatment Prior to Extrusion	Extrusion	Solution Heat Treatment	Ageing
A	Filatomized 7075 spherical powders	1 hour at 475°C under vacuum + 4 hours at 300°C	20:1 at 300°C	2 hours at 475°C	24 hours at 129°C
B	Filatomized 7075 flakes	"	"	"	"
C	Commercial 7075 powder	"	"	2 hours at 460°C	"
D	Commercial 7075 powder	4 hours at 300°C	"	"	"
E*	Modified 7075 splat cooled flakes	1 hour at 490°C under vacuum + 4 hours at 300°C	"	2 hours at 490°C	"
F	7075 - T6 round bar	4 hours at 300°C	"	2 hours at 460°C	3 days at room temperature + 24 hours at 129°C

---

*From J. P. Durand(1)

TABLE III

HARDNESS MEASUREMENTS AFTER DIFFERENT HEAT TREATMENTS OF EXTRUDED BILLETS OF FILATOMIZED POWDERS

Heat Treatment	After Water Quench R_B(Long)	R_B(Trans)	After Natural Ageing; (24 Hours at R.T.) R_B(Long)	R_B(Trans)	After Artificial Ageing (24 Hours at 129°C) R_B(Long)	R_B(Trans)
2 hours at 470°C	28	16.5	42.5	26	51	48
2 hours at 475°C	30	17	61	41	78	68
4 hours at 475°C	34	14.5	61.5	39	72	59
2 hours at 480°C	30.5	13	61	44	77	64
4 hours at 480°C	33	17	68	42	77	61
2 hours at 485°C	31	4	64.5	50	71	49
4 hours at 485°C	15	off scale	57	52	70	53
2 hours at 490°C	26	9	55	48	72	53
4 hours at 490°C	7.5	off scale	42	12	71	46

TABLE IV

TENSILE TEST RESULTS

Sample	Stress (psi)	UTS (psi)	Elongation %	Reduction of Area %	Remarks
A	80,000	94,300	15.1	42.4	Filatomized 7075 - T6 spherical powders ductile fracture with no delaminations
B	78,000	90,200	8.2	12.0	Filatomized 7075 - T6 flakes many fine delaminations accompanied by regions of ductile fracture, few coarse delaminations
C	75,000	87,300	7.8	11.5	Commercial 7075 - T6 powder few delaminations with large regions fractured in a ductile manner
D	68,200	81,900	9.0	13.9	Commercial 7075 - T6 powder severe delaminations accompanied by regions of ductile fracture.
E*	90,750	102,000	8.6	17.5	Splat cooled flakes of a modified 7075 - T6 alloy ductile fracture with few fine delaminations
F	86,200	93,000	11.2	32	7075 - T6 round bar

---

*from J. P. Durand.(1)

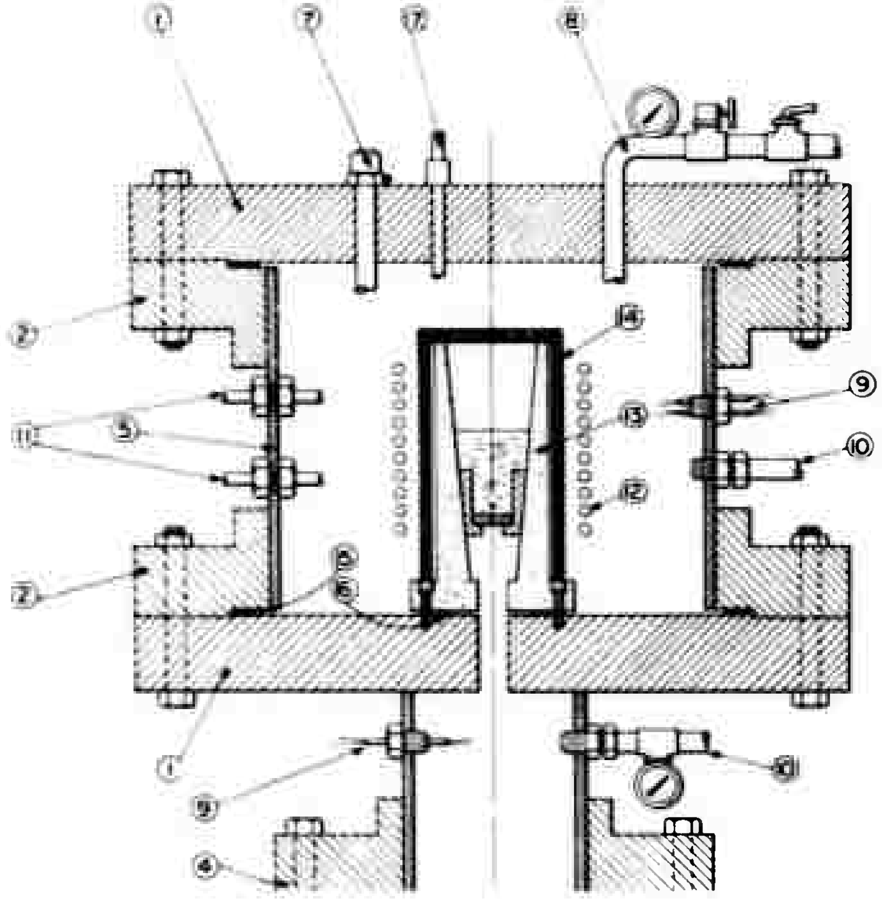

① 10"-300 LB BLIND FLANGES
② 10"-300 LB SLIP-ON FLANGES
③ 4"-600 LB BLIND FLANGE
④ 4"-600 LB SLIP-ON FLANGE
⑤ 10" SCH 80 BLK STEEL SEAM A-106 PIPE, 0"-8½" PE
⑥ 4" SCH 40 BLK STEEL SEAM A-53 PIPE, 0'-5" PE
⑦ SAFETY VALVE
⑧ PRESSURE INFLOW AND OUTFLOW AND PRESSURE GAUGE
⑨ THERMOCOUPLE FEEDTHROUGHS
⑩ ½" PIPE TO VACUUM PUMP
⑪ WATER INFLOW AND OUTFLOW FOR RF COILS
⑫ COILS
⑬ GRAPHITE CRUCIBLE
⑭ FIBERFRAX INSULATING SHIELD
⑮ GASKETS
⑯ INSULATING GASKET
⑰ CHECK VALVE FOR ATMOSPHERE CONTROL

Figure 1. Schematic of filatomization apparatus used in this study.

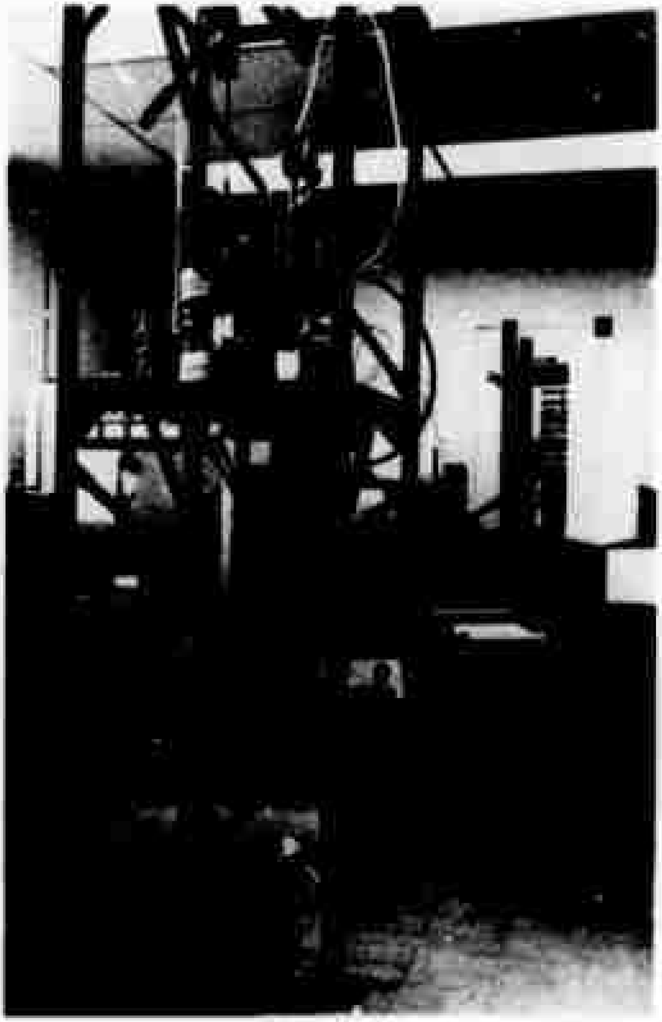

Figure 2. Photograph of filatomization apparatus.

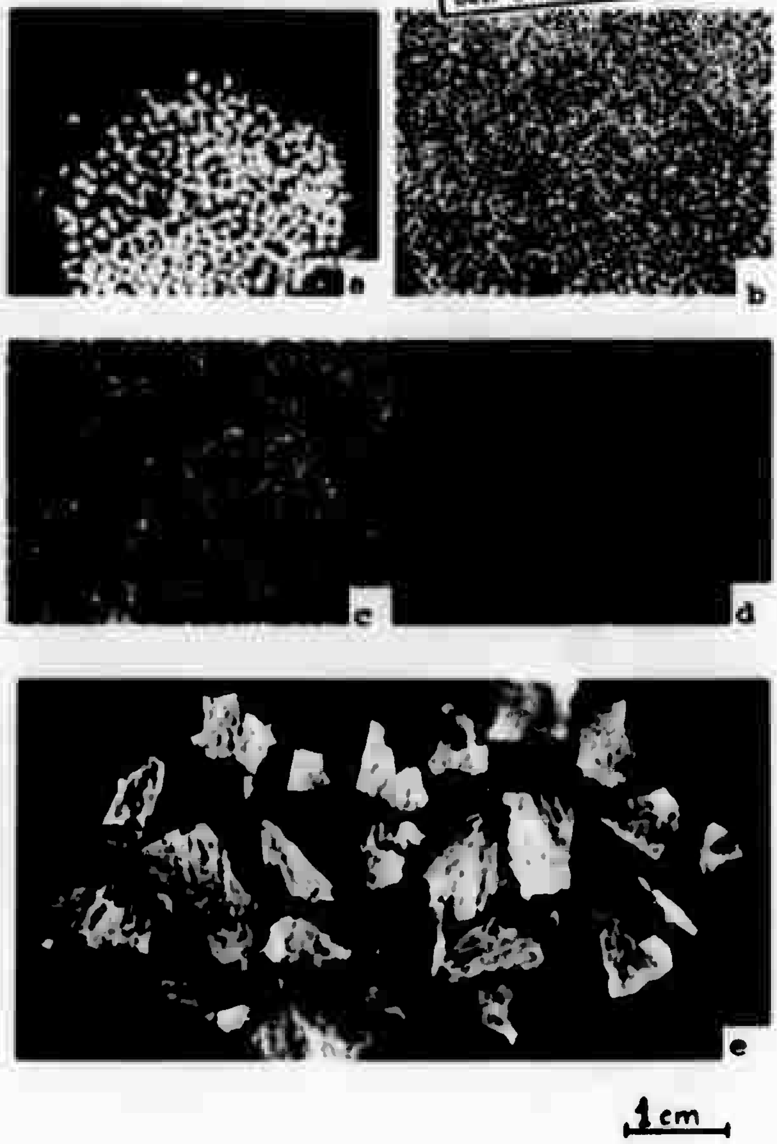

Figure 3. Filatomized powders of pure aluminum and 7075 aluminum alloy; (a) through (d) show pure aluminum powders produced by utilizing an Al_2O_3 filter, Run #1, mesh sizes are -16+20, -20+30, -30+50, and -50+100, respectively, (e) flakes of 7075 alloy produced utilizing a SiO_2 filter, Run #18, mesh size is -8+14.

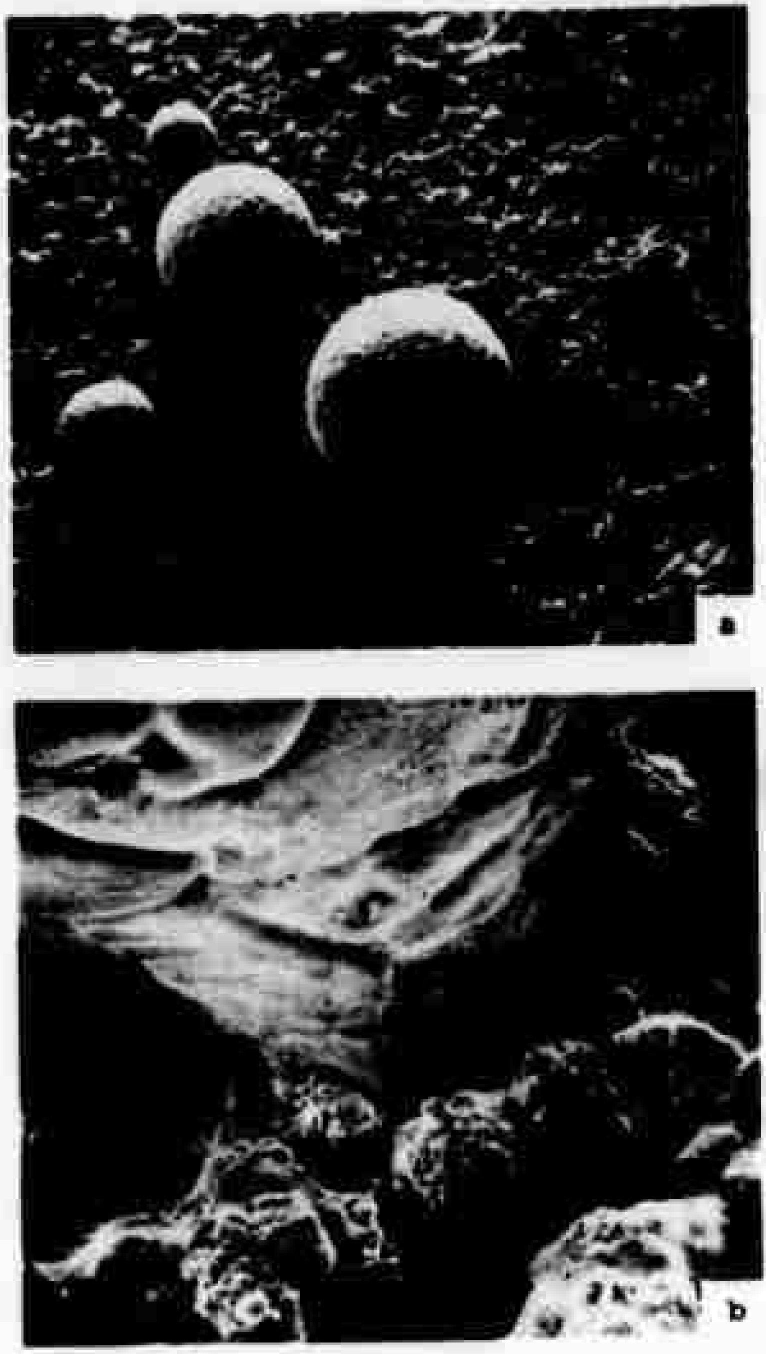

Figure 4. SEM view of pure aluminum powders emerging from a sintered Al_2O_3 filter, Run #1; (a) 23X, (b) 208X.

Figure 5. SEM view of pure aluminum powders emerging from a sintered Al_2O_3 filter; (a) and (b) are from Run #17 at 20X and 90X, respectively, (c) is from Run #19 at 75X.

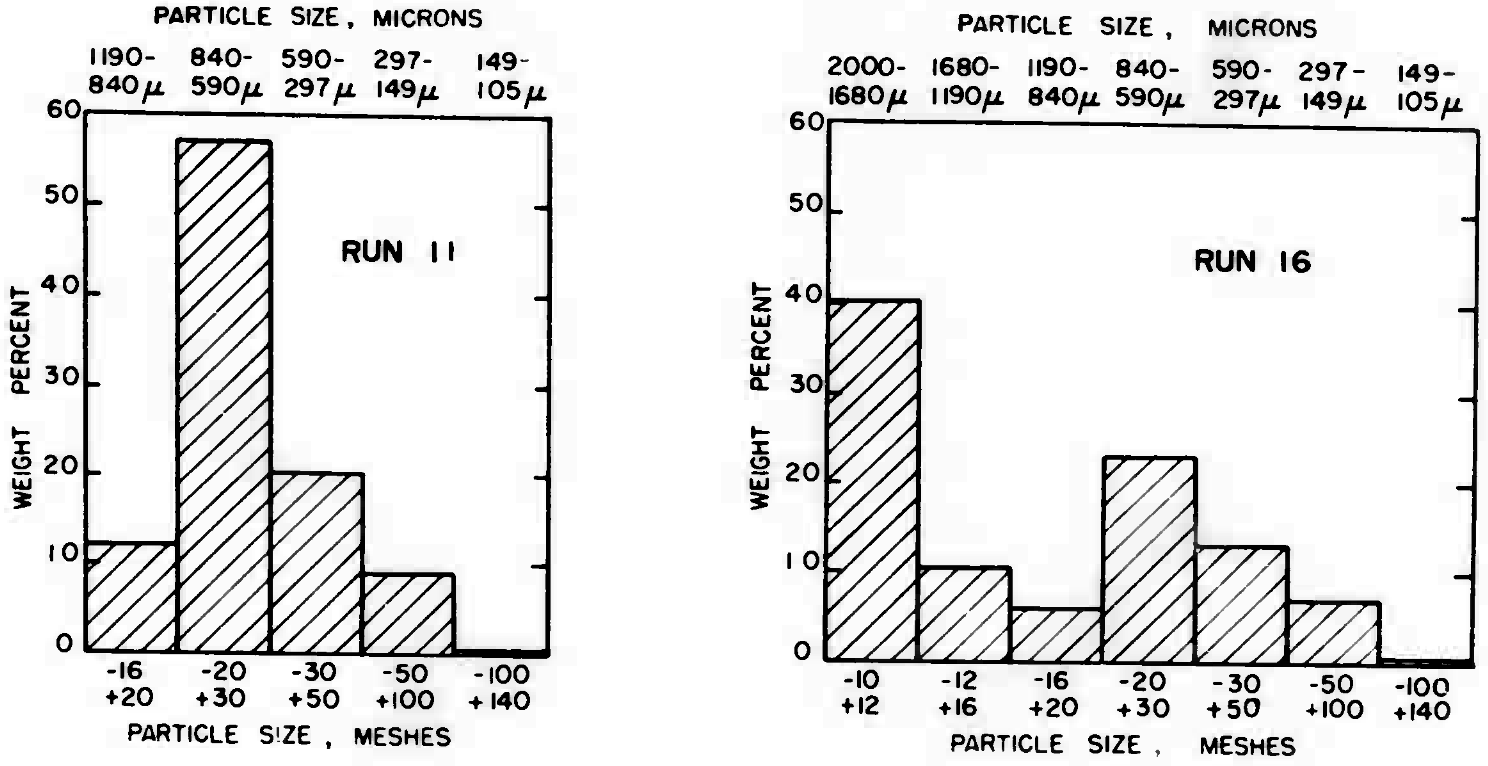

Figure 6. Size distributions of spherical 7075 aluminum alloy powders made utilizing Al_2O_3 filters; (a) Run #11, T_F=700°C, (b) Run #16, T_F=742°C.

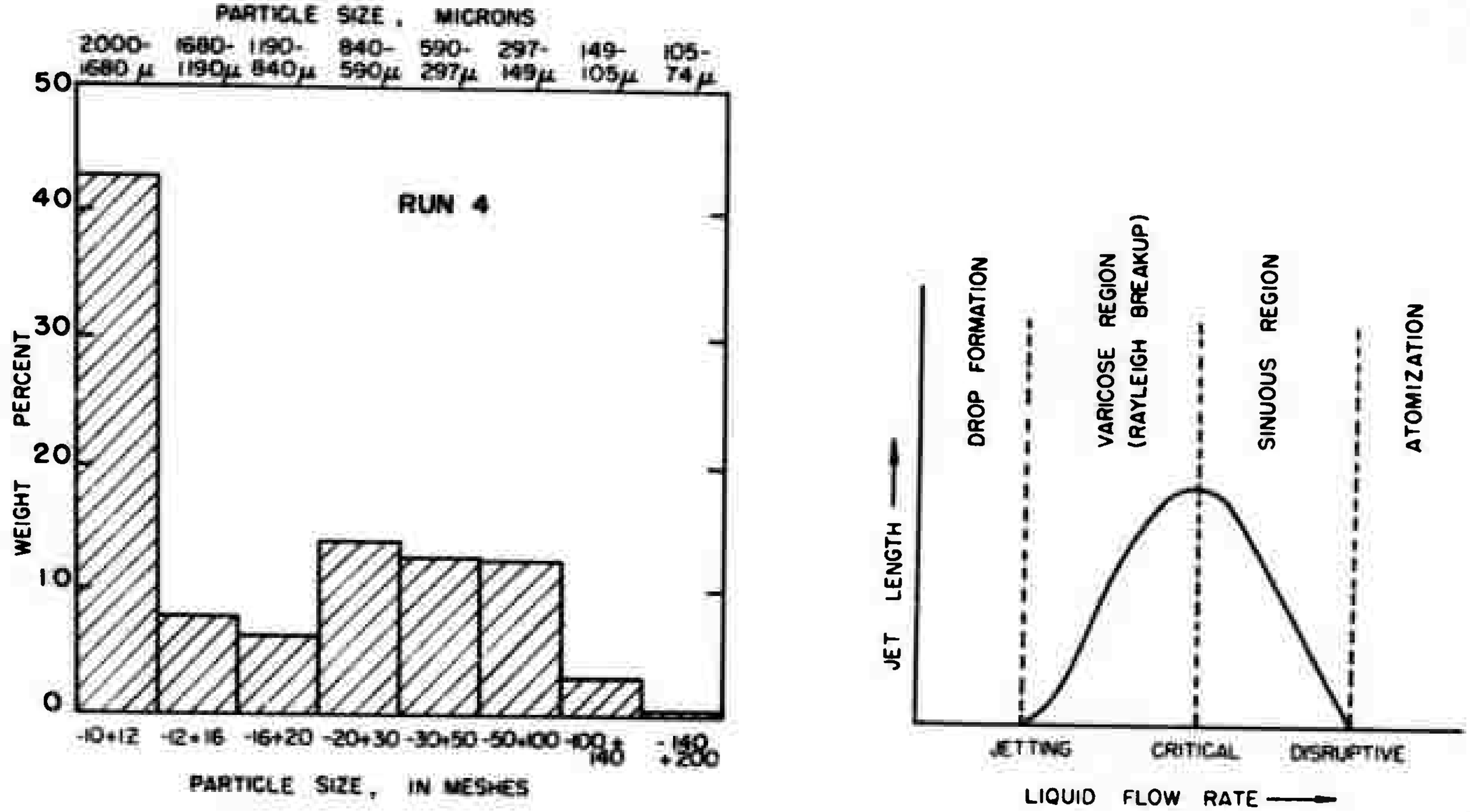

Figure 7. (a) Size distribution of spherical 7075 aluminum alloy powders made utilizing an SiO_2 filter, Run #4; (b) effect of flow rate on formation of drops at the tip of a vertical tube.(5)

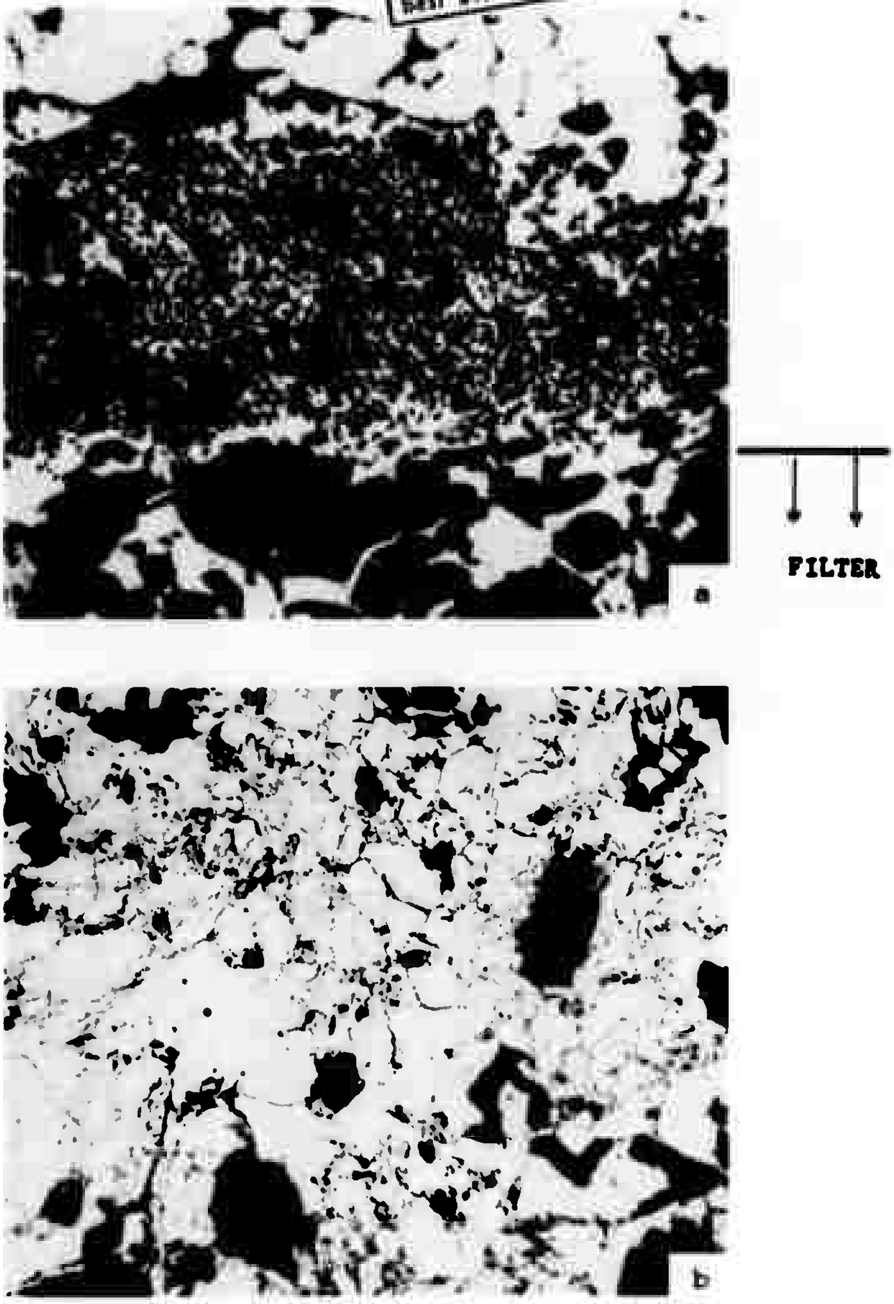

Figure 8. Photomicrographs showing filtration of aluminum oxides from 7075 aluminum alloy melts; (a) oxide "cake" observed above the SiO_2 filter used in Run #4, 80X, (b) oxide skins retained above the Al_2O_3 filter used in Run #16, 100X.

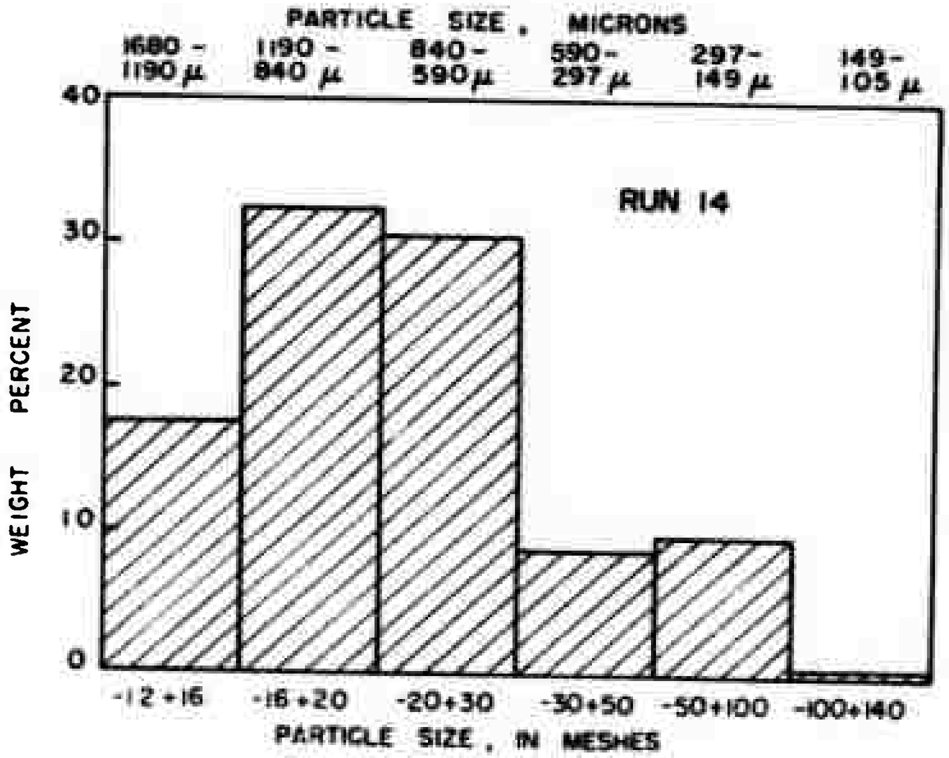

Figure 9. Size distribution of spherical 7075 aluminum alloy powders made in Run #14.

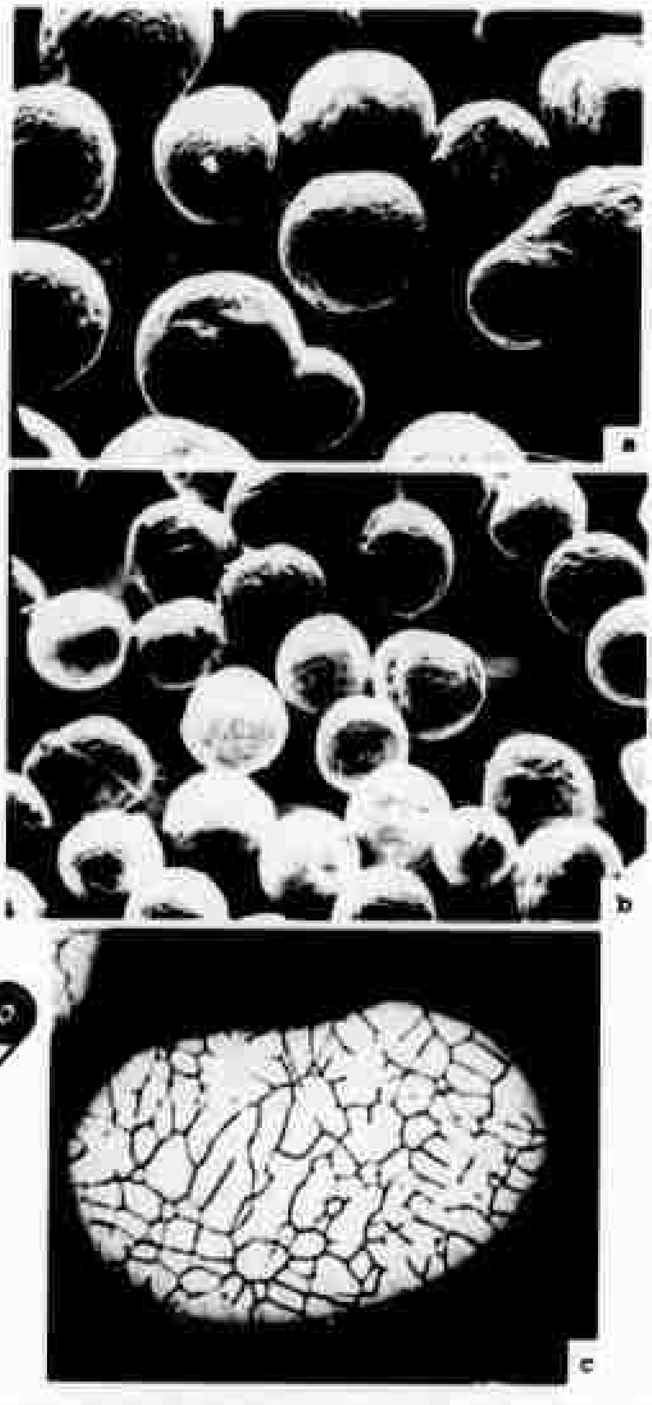

Figure 10. Structures of filatomized pure aluminum powders made in Run #1; (a) SEM view of ~300μ size powders, 51X, (b) SEM view of ~150μ size powders, 20X, (c) a representative microstructure of the powders

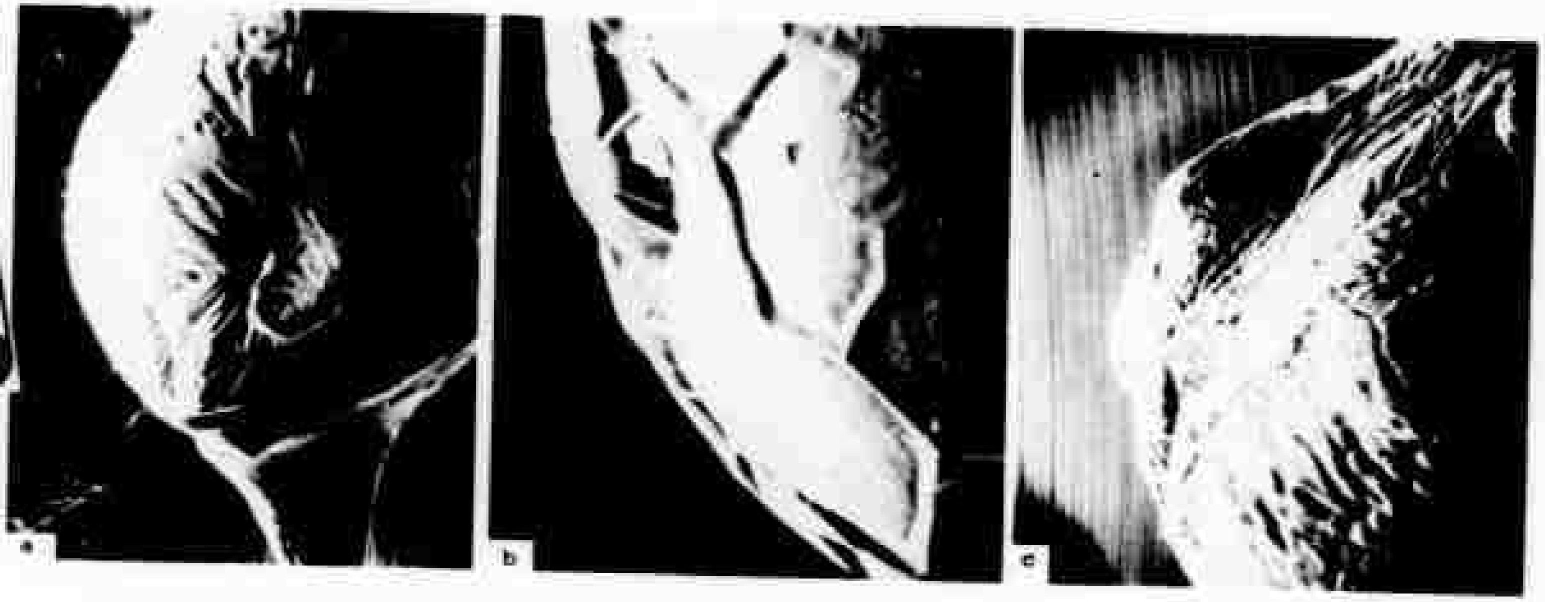

Figure 11. Surface irregularities of filatomized pure aluminum powders; (a) Run #1, 590X, (b) Run #17, 500X, (c) Run #19, 590X.

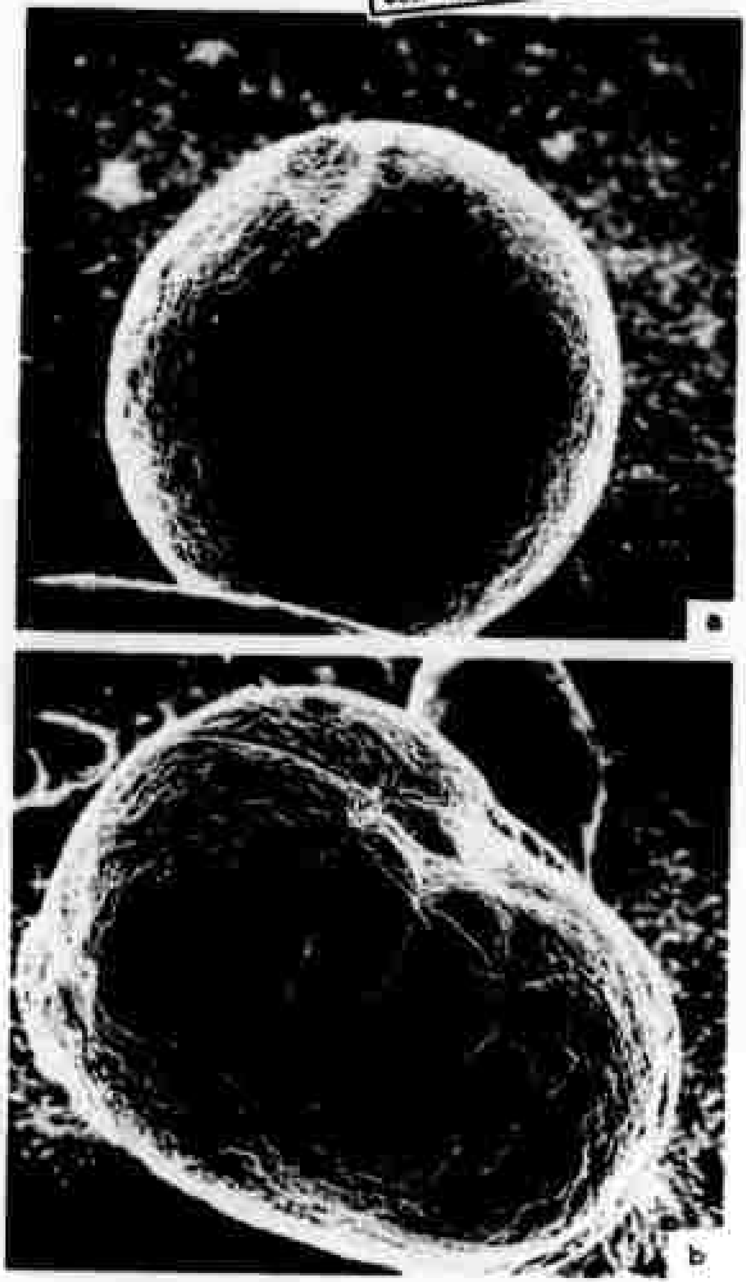

Figure 12. SEM view of filatomized spherical powder of 7075 aluminum alloy made in Run #16; (a) 110X, (b) 200X.

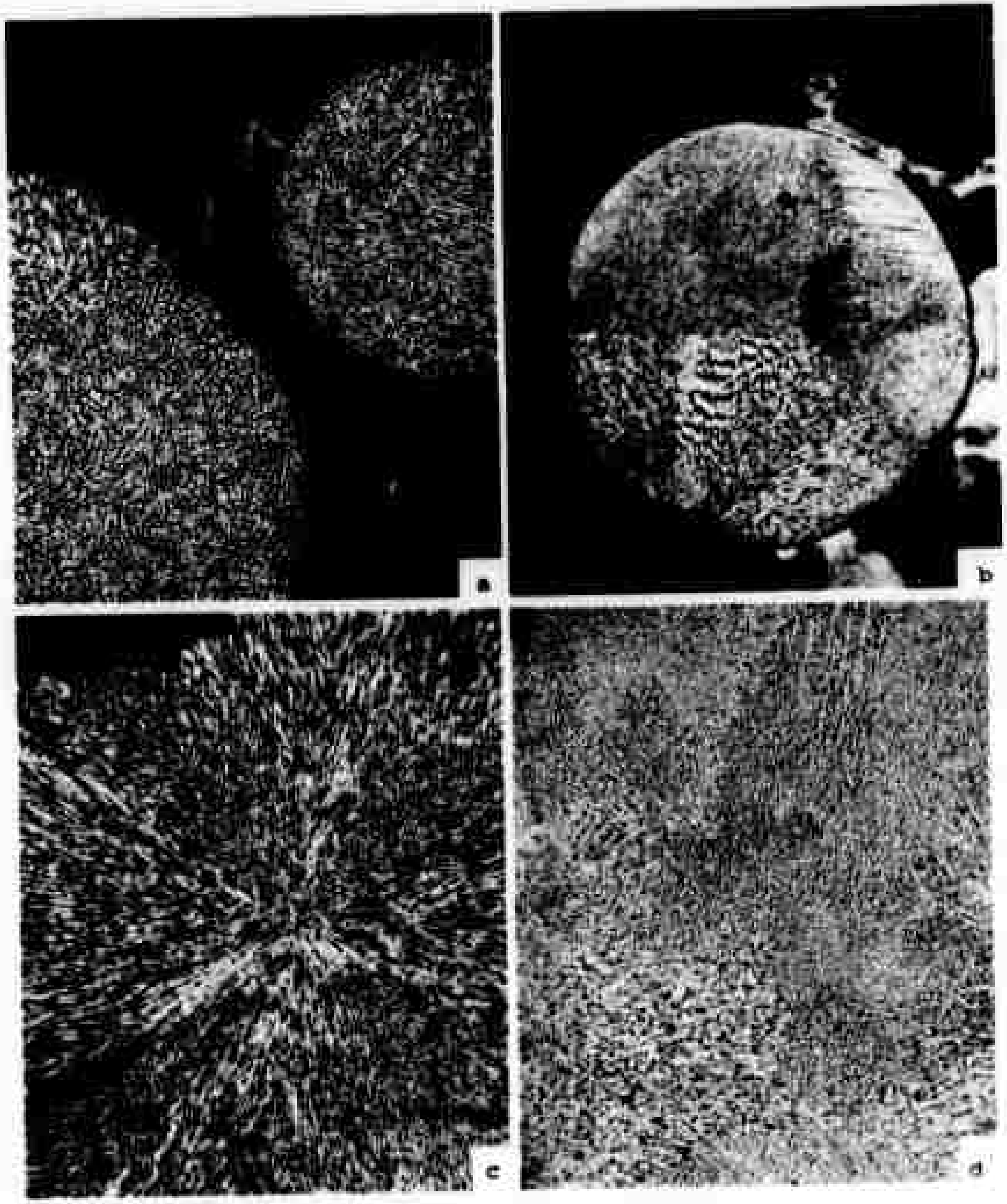

Figure 13. Microstructures of filatomized spherical powders of 7075 aluminum alloy obtained from different experiments; (a) Run #6, 100X, (b) Run #11, 100X, (c) Run #18, 200X, (d) Run #16, 100X.

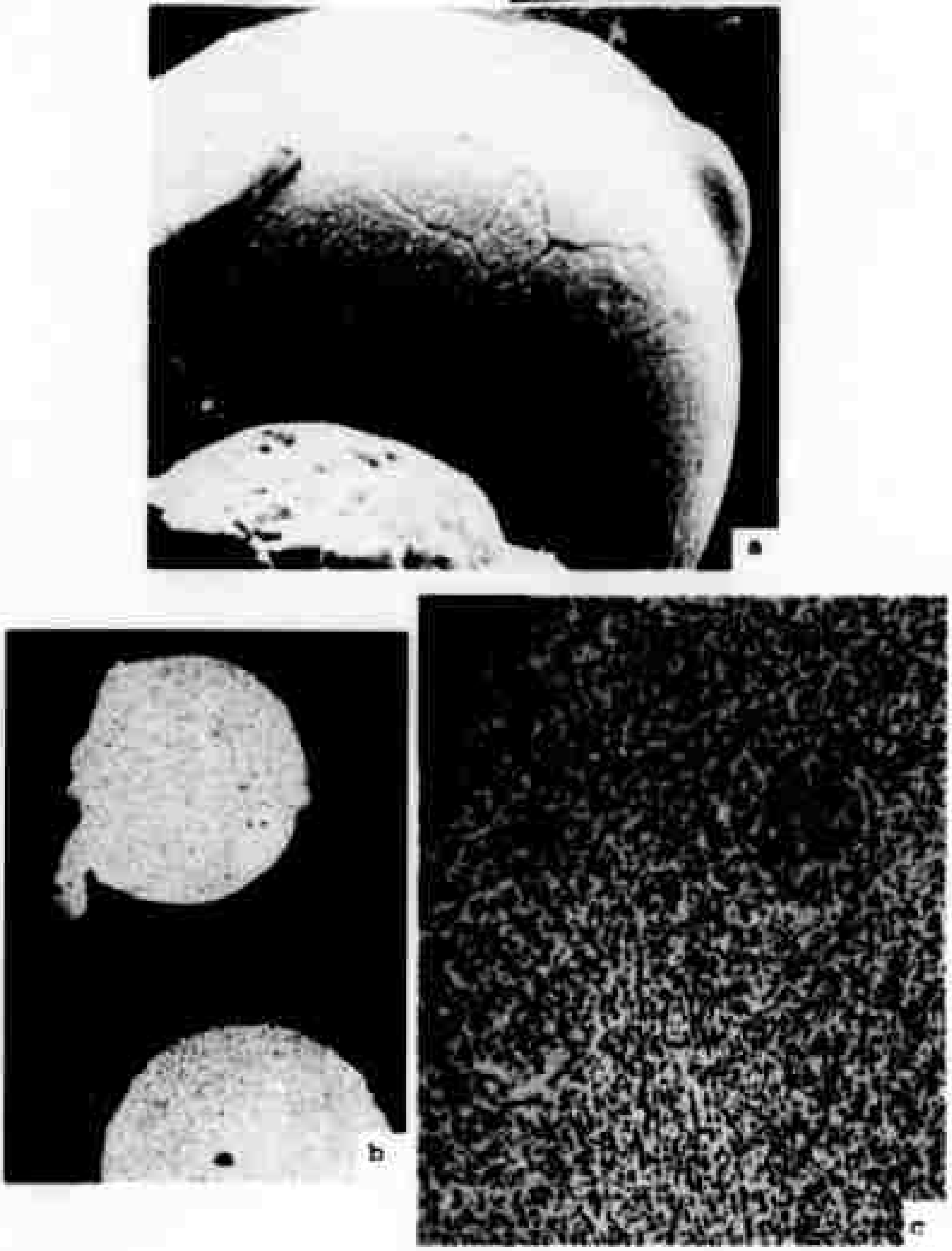

Figure 14. Structure of filatomized spherical powders of 7075 aluminum alloy made in Run #11, (a) SEM view of a powder, 540X, (b) and (c) show the microstructure of the powder at 100X and 500X, respectively.

Figure 15. Powders of 7075 aluminum alloy made in Run #11; (a) 1000X, (b) 500X.

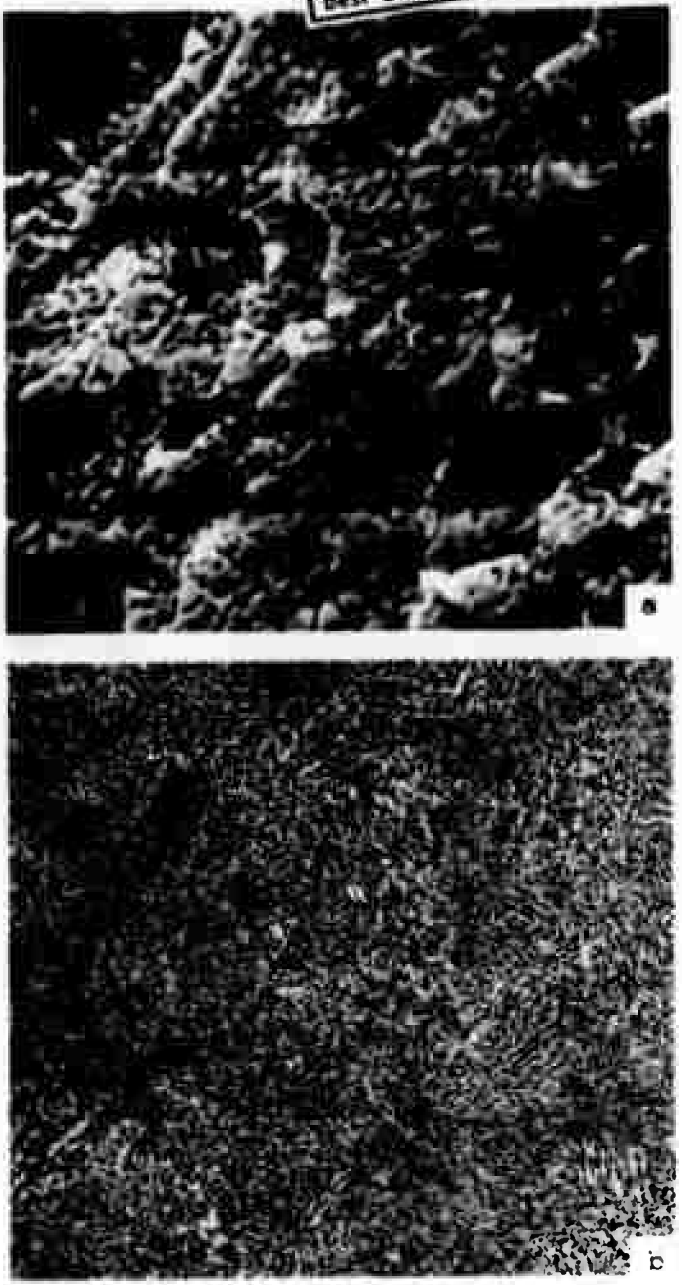

Figure 16. Structure of a filatomized flake of 7075 aluminum alloy made in Run #8; (a) SEM view, 2300X, (b) "duplen" dendritic structure due to sudden variation in cooling rate, 100X.

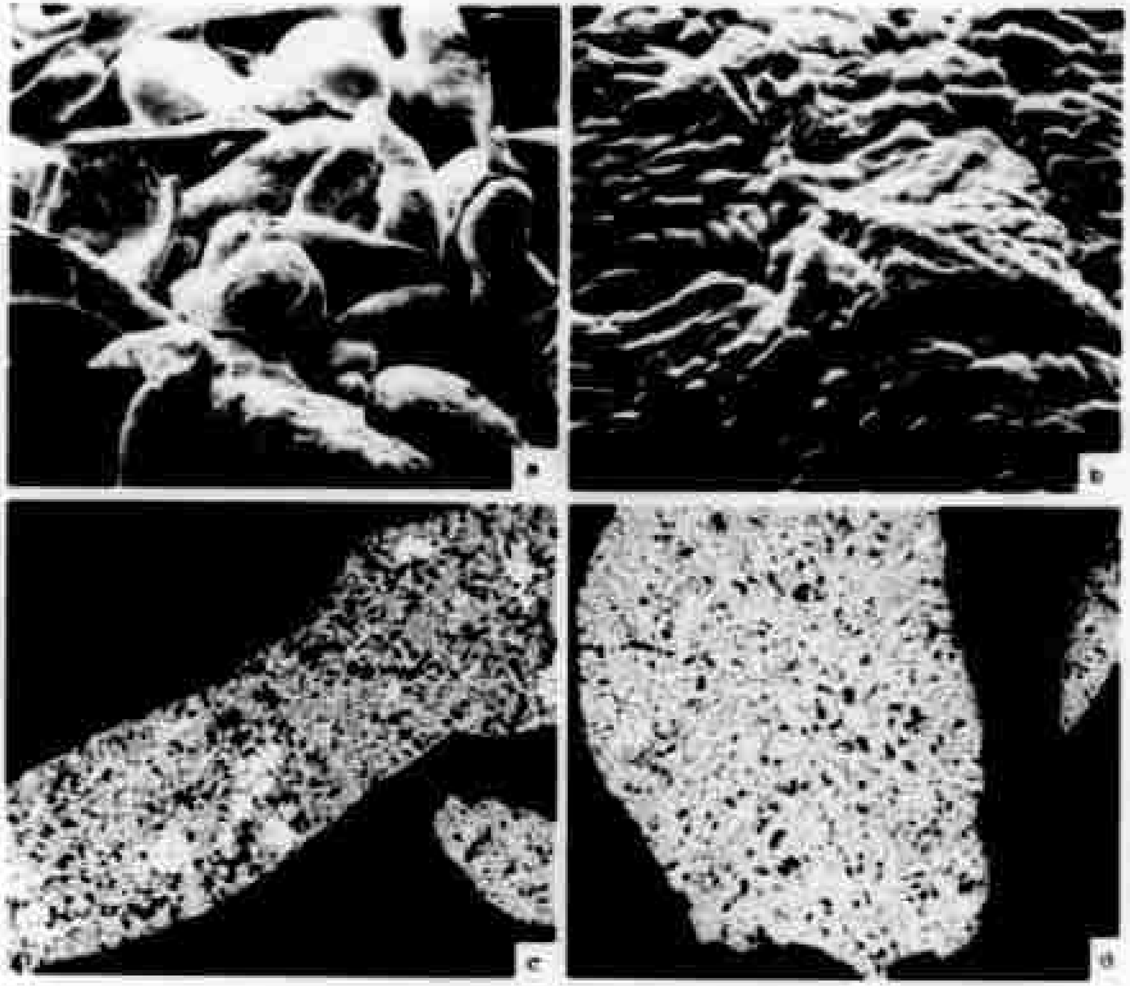

Figure 17. Structure of commercial 7075 aluminum alloy powders; (a) and (b) are SEM views at 24X and 140X, respectively. (c) and (d) show microstructure of the powders at 100X.

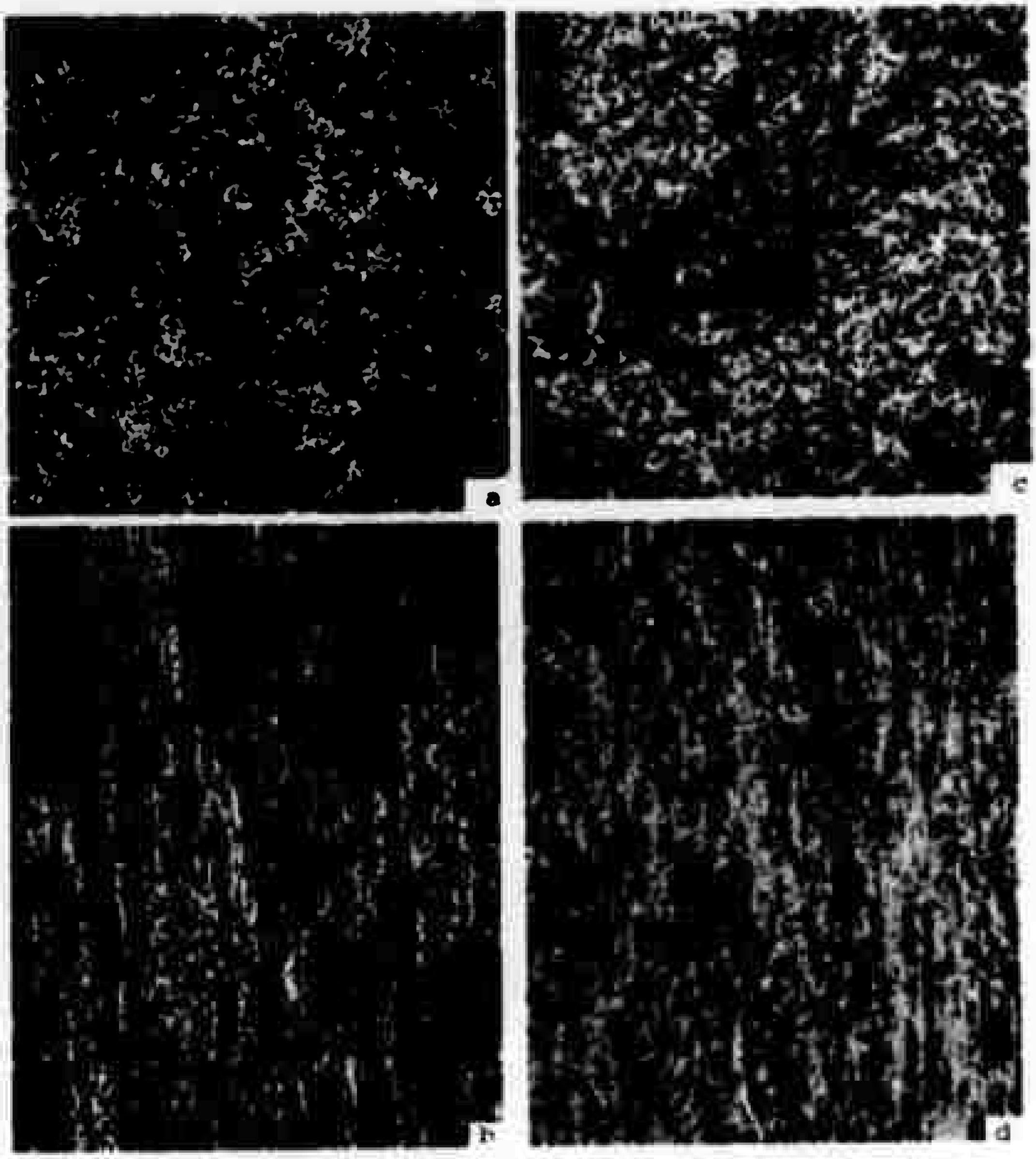

Figure 18. Structure of extruded billet made from filatomized spherical powders of 7075 aluminum alloy; (a) and (c) show the transverse microstructure at 100X and 500X, respectively, (b) and (d) show the longitudinal microstructure at 100X and 500X, respectively.

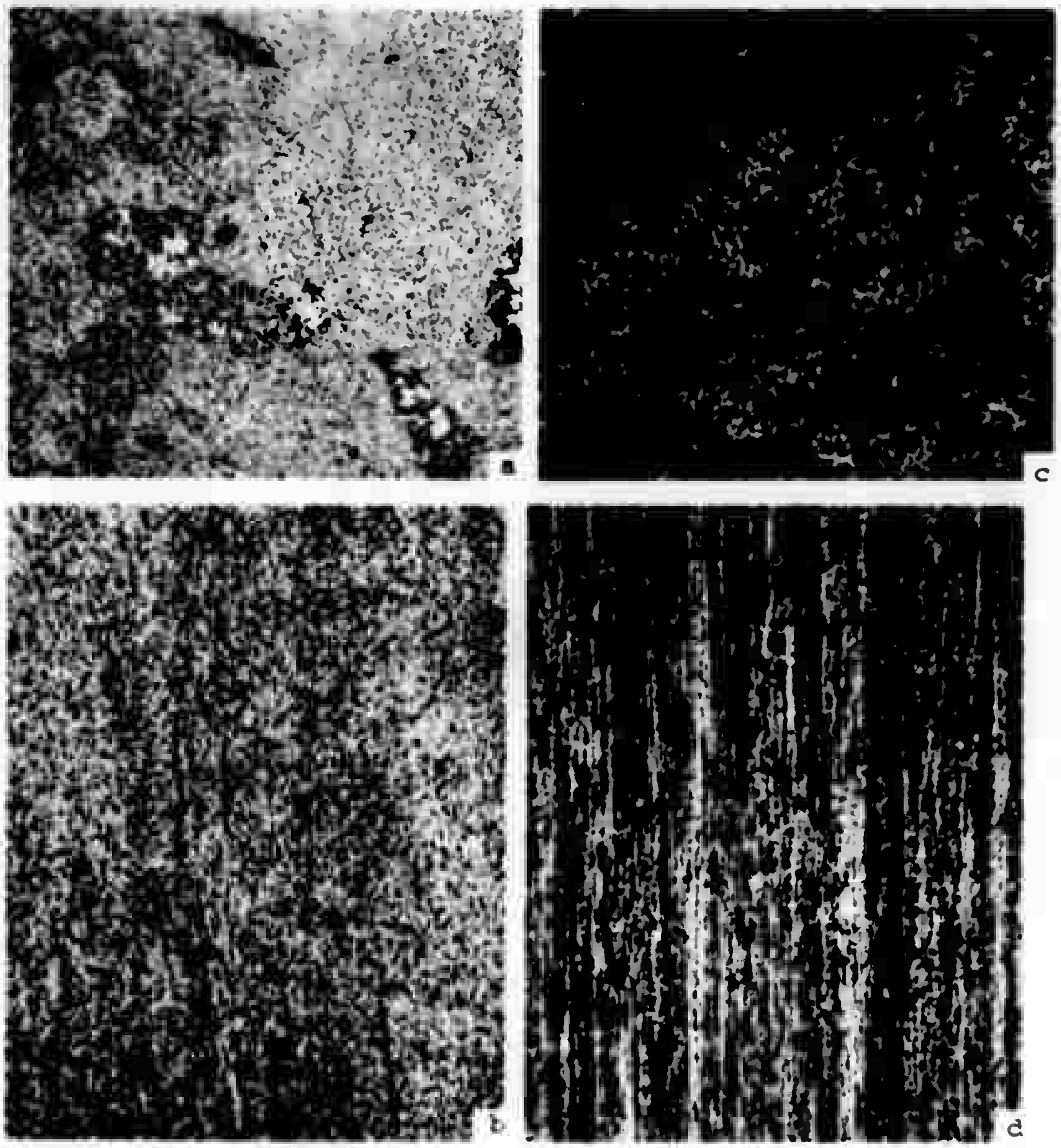

Figure 19. Structure of extruded billets of 7075 aluminum alloy powders; (a) and (b) show transverse and longitudinal microstructures of the billet made from filatomized flake, 100X, (c) and (d) show transverse and longitudinal microstructure of the billet made from commercial powders, 100X.

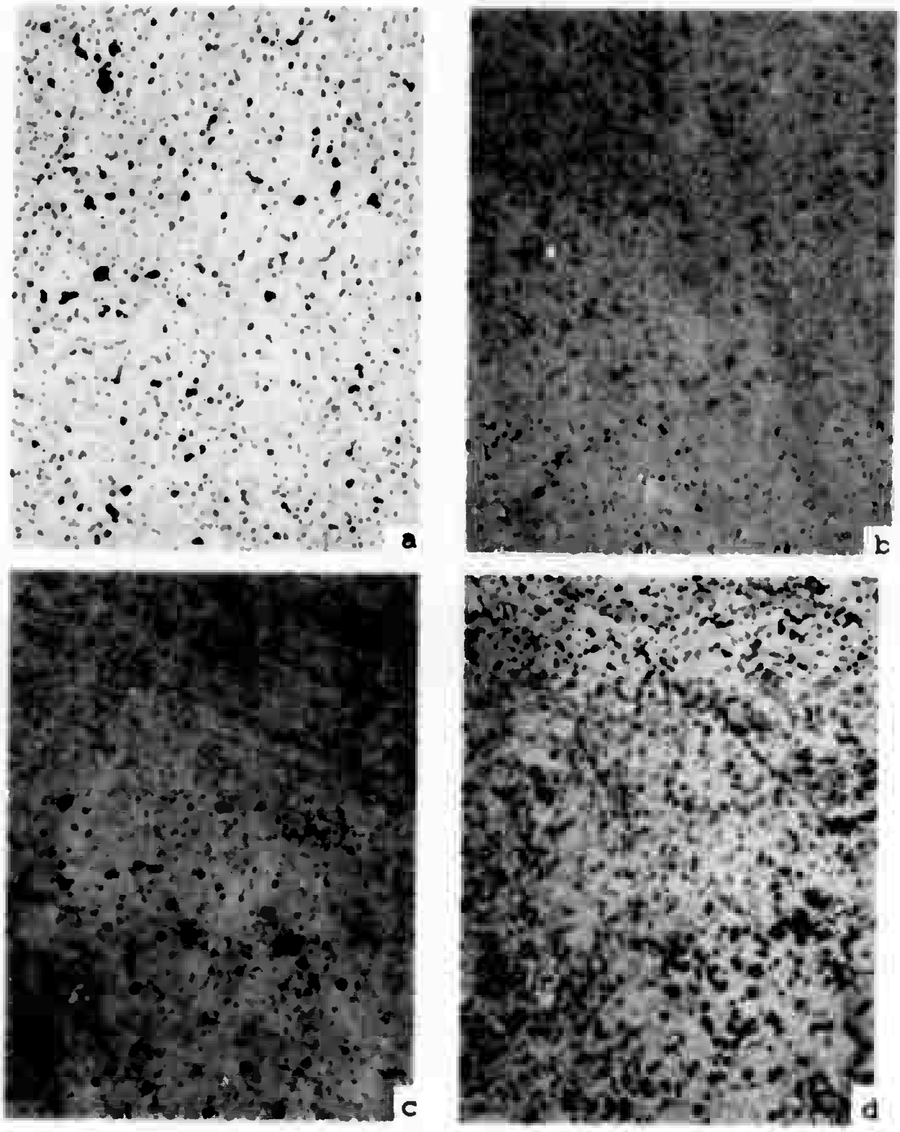

Figure 20. Microstructures of the extruded billet of 7075 aluminum alloy of filatomized spherical powders, in different solutionized conditions, 500X; (a), (b), (c), and (d) are from samples solutionized for 2 hours at 470°C, 475°C, 480°C and 490°C, respectively.

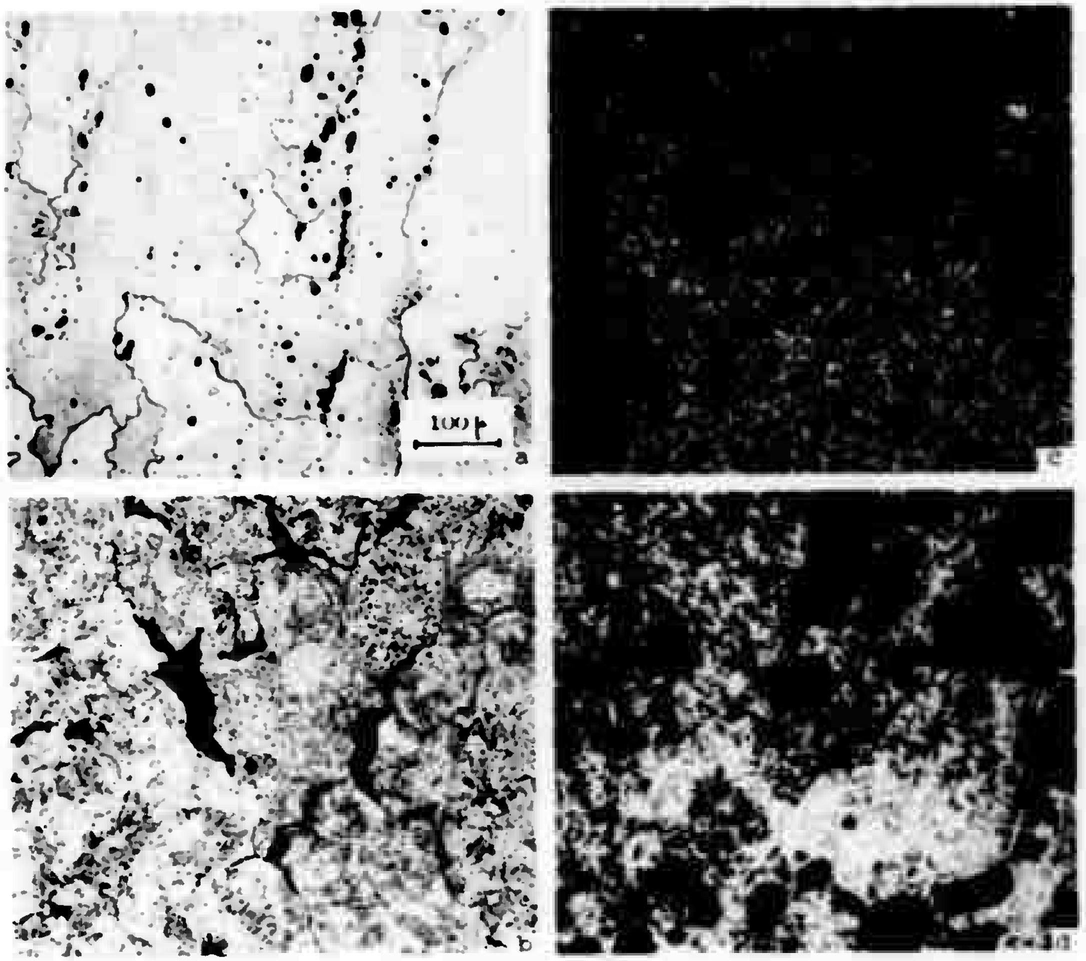

Figure 21. Transverse microstructures of 7075 - T6 extrusions reported in Table II; (a) commercial bar stock, billet F, 150X, (b) and (c) are extrusions of commercial powders D and C, respectively, 100X, (d) extrusion of filatomized flakes, billet B, 100X.

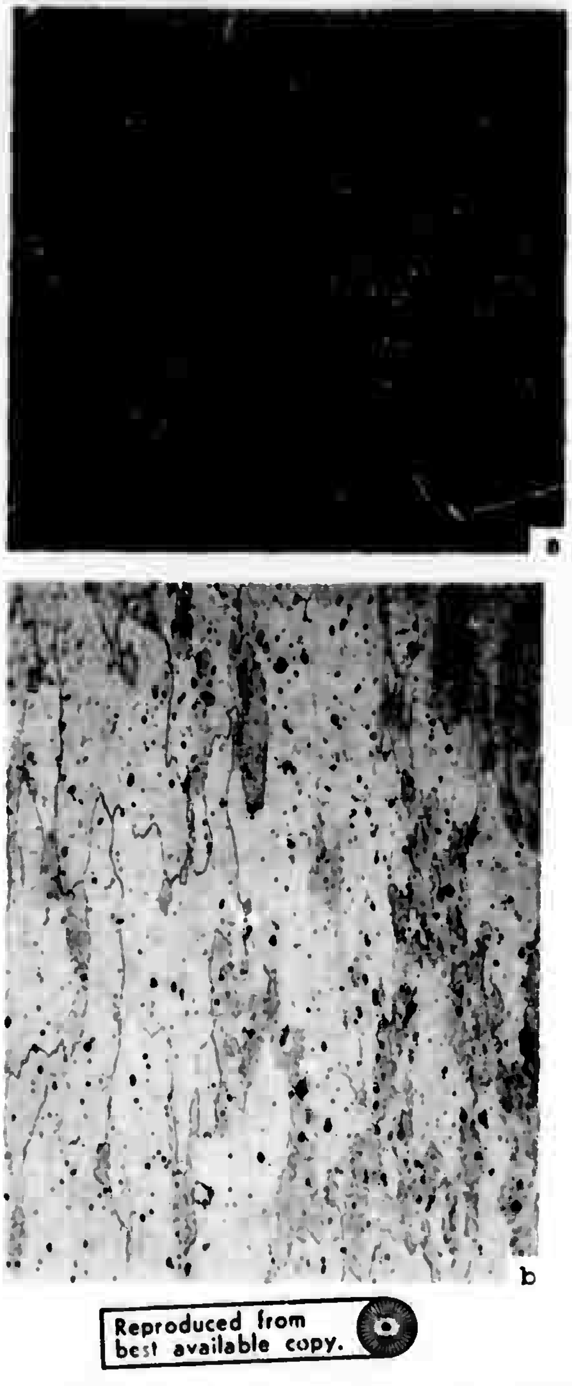

Figure 22. Microstructure of 7075 - T6 extrusion made from filatomized spherical powders, billet A (Table II), 100X; (a) transverse section, (b) longitudinal section.

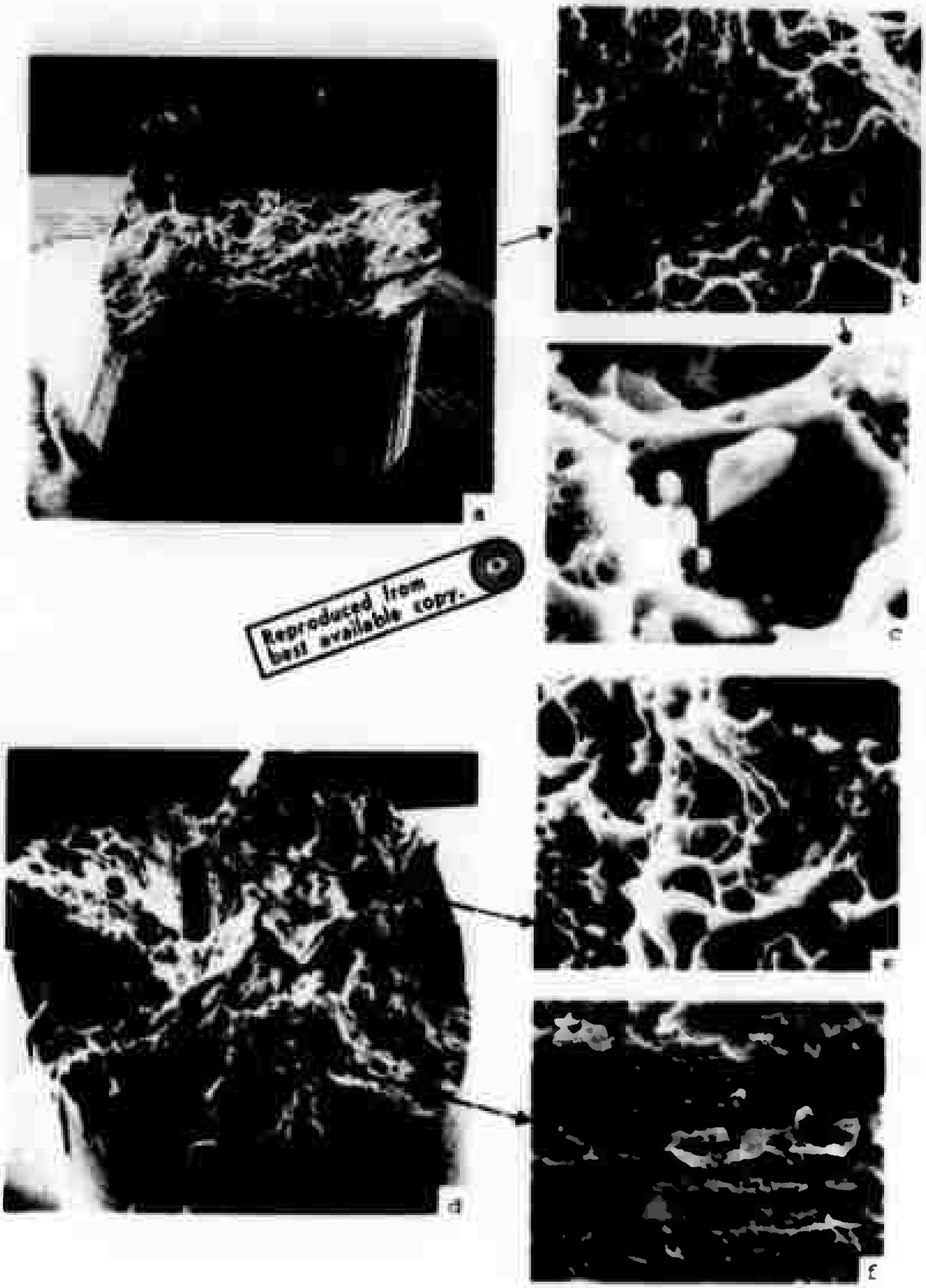

Figure 23. (a),(b),(c) SEM fractographs of 7075-T6 extrusion of filatomized spherical powders, billet A (Table II), 20X,950X, 4750X, respectively.
(d),(e),(f) SEM fractographs of 7075-T6 extrusion of filatomized flakes, billet B (Table II), 23X,2300X,2300X, respectively.

Figure 24. (a),(b),(c) SEM fractographs of extruded commercial 7075-T6 commercial powder, billet C (Table II), 27X, 260X, 2620X, respectively.
(d),(e),(f) SEM fractographs of extruded 7075-T6 splat cooled flakes, billet E (Table II), 22X, 120X, 2080X, respectively.

TASKS III and IV

Thermomechanical Treatment, Microstructure and Mechanical Properties

---

L.F.P. Van Swam

R.K. Robinson

M.M. Salama

R.M.N. Pelloux

A.S. Argon

N.J. Grant

MECHANICAL PROPERTIES OF 300 GRADE MARAGING STEELS

A. INTRODUCTION

The fatigue properties of 300 grade maraging steels have undergone extensive study during the past six months. In addition of the determination of S-N curves for commercial and powder metallurgy products in the aged condition in air and dry argon, crack propagation rates and low cycle fatigue properties have been measured. Crack propagation rates were measured in Vascomax 300 in both the annealed and aged condition in air as well as in dry argon. The test specimens were 3/8" thick plates (plane strain condition) and 1/16" thin sheet (plane stress condition). The cyclic stress-strain curve of aged Vascomax 300 was also determined.

In an attempt to improve the ductility and the fracture toughness of maraging 300 steel, a 2" thick bar of Vascomax 300 was hot rolled at 1600°F to 0.30" thickness. A decrease in grain size from 25 microns to 5 microns was accomplished. The reduction of area as measured in tensile testing showed little improvement but the fracture toughness was increased from 62.6 ksi $\sqrt{\text{inch}}$ for the 25 micron material and 71.3 ksi $\sqrt{\text{inch}}$ for the 5 micron material.

B. FATIGUE PROPERTIES

S-N curves for Vascomax 300 in the aged condition tested in air and dry argon (dewpoint -70°F) and for a powder metallurgy product tested in a air were reported earlier (1). All testing was done with a Baldwin SF-1U machine in tension-compression with a zero mean load. It was observed that the fatigue limit for 300 grade maraging steel was low compared to the yield strength. For most low and intermediate strength steels the ratio of fatigue strength to yield strength is about 0.5 (2). In the case of maraging steel, a yield strength of 260 ksi is easily obtained, the fatigue strength at 10^7 cycles however is only 100 ksi when the material is tested in dry argon (dewpoint -70°F). To get a better understanding of the fatigue mechanisms in maraging steel the following tests were carried out:

- Determination of crack propagation rates as a function of the stress intensity factor, under plane strain and plane stress testing conditions. Testing was done on annealed and aged specimens and a few tests were done in a dry argon atmosphere.
- Determination of the cyclic stress strain curve of aged maraging steel.
- Determination of the S-N curve of annealed maraging steel in dry argon.

The specific details and results of these tests are as follows.

1. Crack Propagation Rate

A 3/8" thick double cantilever beam test specimen was used to measure the crack propagation rate dl/dN as a function of the stress intensity factor range ΔK under plane strain conditions (see Figure 1). Crack length is measured with a telescope mounted on the loading frame and is accurate to 0.0005". The ΔK load calibration curves were taken from ASTM STP 410.

The results of these tests are shown in Figures 2 and 3. It is observed that the crack propagation rates for annealed and aged maraging steel are exactly identical. When testing was done in a dry argon atmosphere slightly lower crack propagation rates were found. The crack propagation rates for this material were measured under plane stress conditions with a 1/16" thick sheet of maraging 300 steel obtained from Vasco. Specimens of this material were made according to the drawing in Figure 1 and the ΔK load calibration curve was again obtained from ASTM STP 410. The results for the aged material are given in Figure 2 and for the annealed material in Figure 3. Testing was done with the crack growing in a direction parallel and perpendicular to the rolling direction. The material showed a pronounced degree of banding but the crack propagation rates in both directions are nearly equal. Surprisingly enough, the propagation rate in plane stress is higher than the propagation rate in plane strain. The opposite would be expected. This discrepancy might be due to the banding observed in the thin sheet or to a slightly different composition of the materials(they were not from the same heat). In any case, the difference is not large and the slopes of the growth rate curves are identical.

2. Cyclic Stress Strain

The cyclic stress strain curve for aged maraging steel was measured using the method proposed by Landgraf(3). Testing was done on a MTS hydraulic machine. The strain in a 1/4" diameter hourglass shape specimen was measured and used to control the machine. The strain was increased after every completed hysteresis loop. The plot for increasing strain obtained in this way is shown in Figure 4. Aged maraging 300 steel is shown to cyclically soften. A curve for annealed steel has not been obtained as yet but this material too is expected to soften, since the work hardening exponent is only 0.03 (1). Materials with a work hardening exponent less than 0.10 are usually observed to cyclically soften (3).

3. S-N Curve for Annealed Maraging Steel

Some preliminary results obtained in the same way as earlier testing on aged material show that the fatigue limit of annealed maraging 300 steel with a yield strength of 130 ksi is 60 ksi. This value is slightly below the ratio fatigue strength yield strength of 0.5 that can be expected (2).

In summary, we can say that the low fatigue strength of maraging steel must be due to the easiness with which fatigue cracks are initiated. The cyclic softening of these steels gives an effective yield strength in fatigue well below the yield strength observed in monotonic loading and this may account for the initiation of cracks at a load equal to 0.35 of the monotonic yield strength.

C. TENSILE STRENGTH AND FRACTURE TOUGHNESS OF FINE GRAINED VASCOMAX 300

As explained in the introduction, fine grained Vascomax 300 was obtained by hot rolling (at 1600°F) a 2 micron thick bar to 0.30" thickness.

Tensile testing in directions parallel and transverse to the rolling direction were done on material receiving the following heat treatments.

- 1 as received
- 2 as received plus 3 hours at 900°F ageing
- 3 1 hour 1500°F anneal
- 4 1 hour 1500°F anneal plus 3 hours at 900°F ageing

The results of these tests are summarized in Table I together with the results of commercial Vascomax 300. Only small differences are observed with the fine grained material in the aged condition being slightly stronger.

Fracture toughness testing according to ASTM E399 70T was done on

0.25" thick specimens with the notch parallel to the rolling direction. The test results are given in Table II along with test results of commercial material. The plane strain fracture toughness is seen to have increased from 62.6 ksi $\sqrt{\text{inch}}$ to 71.3 ksi $\sqrt{\text{inch}}$.

D. [illegible]

1. Semi-Annu[illegible]chnical Report No. 3, ARPA Order No. 1608, January, 1972.

2. McClintock, F.A. and A.S. Argon, *Mechanical Behavior of Materials*, Addison-Wesley, Reading, Massachusetts, 1966, p. 600.

3. Landgraf, R.W., "The Resistance of Metals to Cyclic Deformation", ASTM STP 467.

TABLE I

Tensile Properties of Fine Grain Vascomax 300 Compared to Commercial Vascomax 300

	Parallel to Rolling Direction			Transverse to Rolling Direction		
	R.A.	U.T.S.	0.2 %	R.A.	U.T.S.	0.2 %
As recieved	71.7	147.5	109.0	68.8	157.0	125.0
As received + 1 hour at 1500°F	74.6	146.0	118.0	68.4	146.0	112.0
Commercial 1 hour at 1500°F	74.0	145.5	129.9			
As recieved + 3 hours at 900°F	50.0	260.0	253.0	50.1	283.0	277.0
1 hour 1500°F + 3 hours at 900°F	55.7	281.0	276.0	48.5	286.0	280.0
Commercial 1 hour 1500°F + 3 hours 900°F	50.8	277.0	271.0			

TABLE II

Fracture Toughness of Fine Grain Vascomax 300 Compared to Commercial Vascomax 300

	Load* lbs.	N cycles	K_{IC} ksi $\sqrt{in.}$	R_c**
Fine grain as received + 3 hours 900°F	625	26,000	73.2	53
	625	31,000	70.2	53
	625	24,500	70.0	53
Commercial 1 hour 1500°F + 3 hours 900°F	700	17,000	61.6	53
	625	19,500	62.7	54
	625	20,500	63.3	54

* Load indicates the load used to propagate the last .025" of the fatigue crack.

** The hardness was measured after toughness testing to check for proper heat treatment.

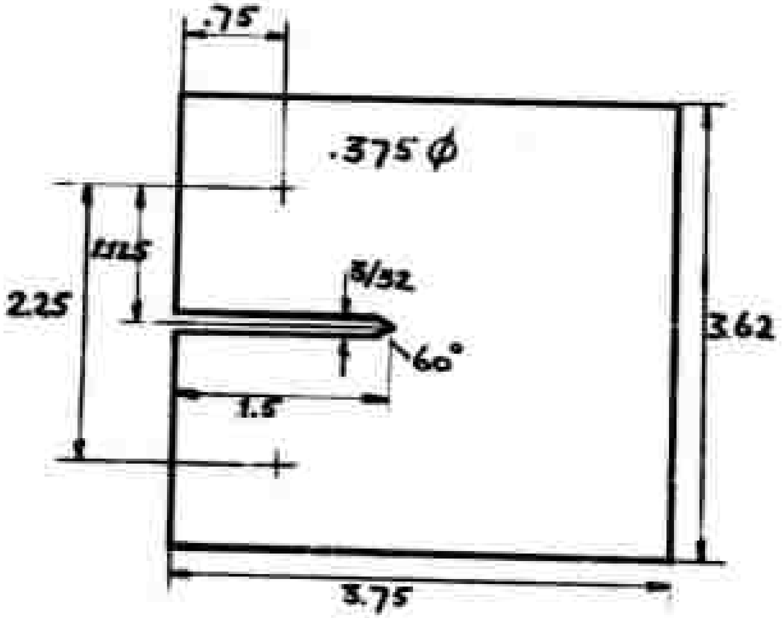

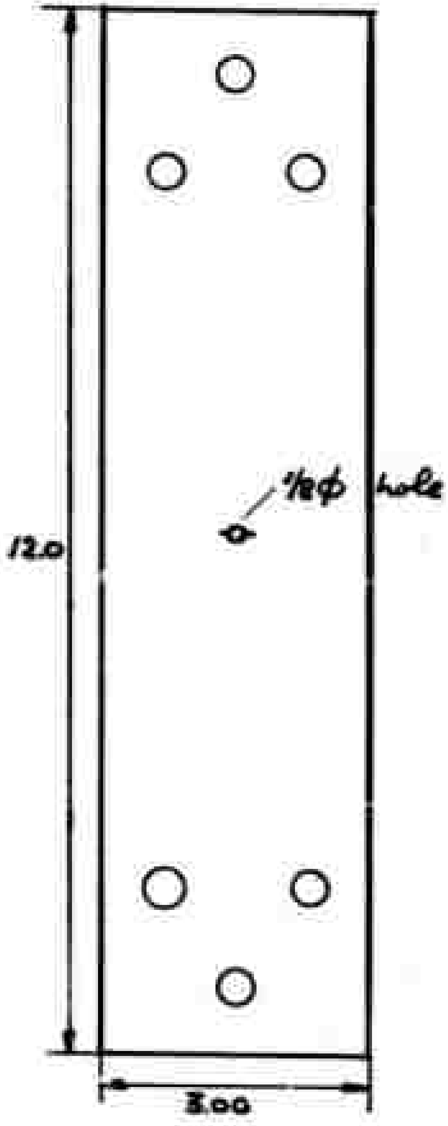

Figure 1 - Crack propagation specimens: above for testing under plane strain conditions, to right for plane stress.

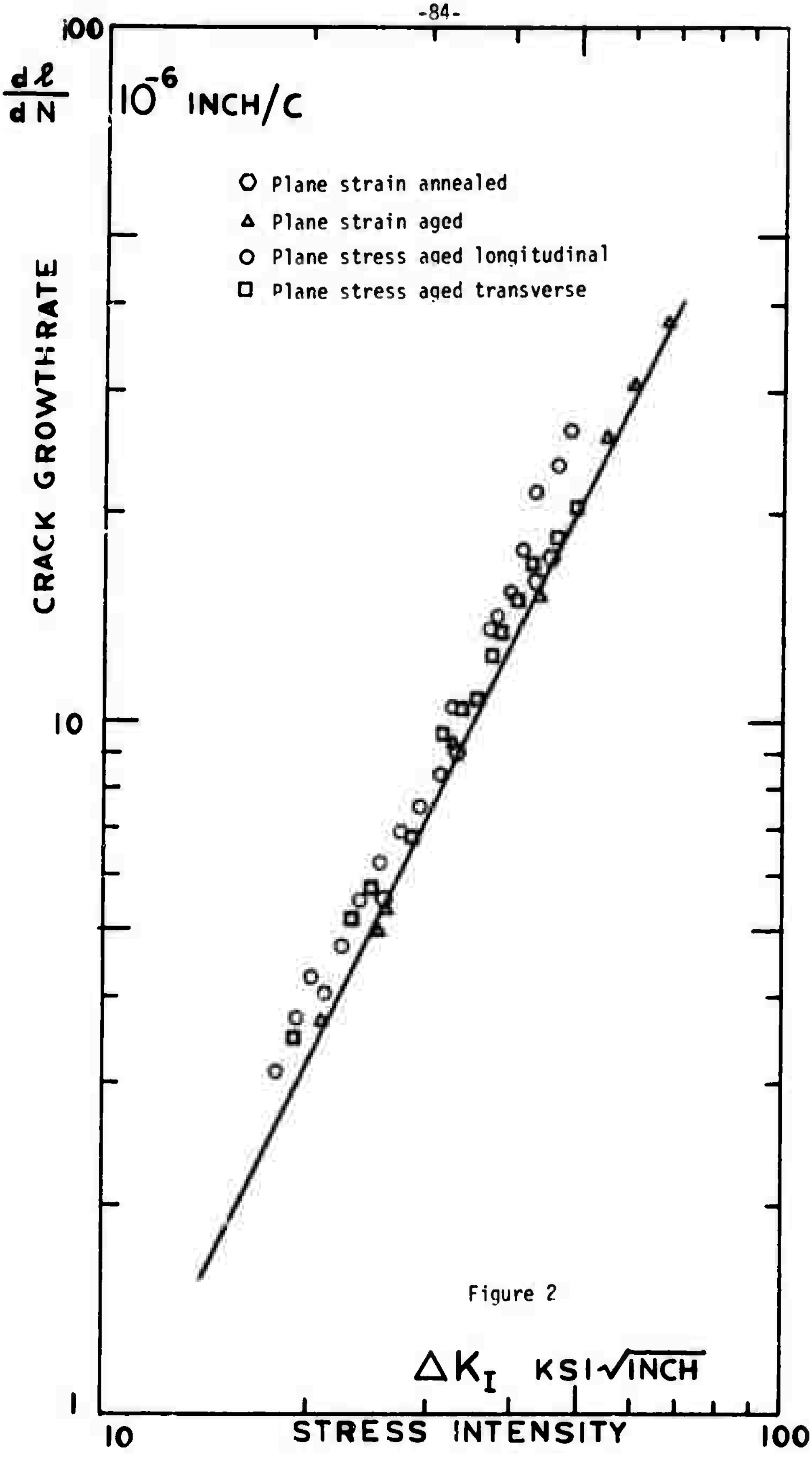
100
$\frac{d\ell}{dN}$ 10^{-6} INCH/C
CRACK GROWTHRATE
○ Plane strain annealed
△ Plane strain aged
○ Plane stress aged longitudinal
□ Plane stress aged transverse
10
1
ΔK_I KSI$\sqrt{\text{INCH}}$
10
STRESS INTENSITY
100

Figure 2

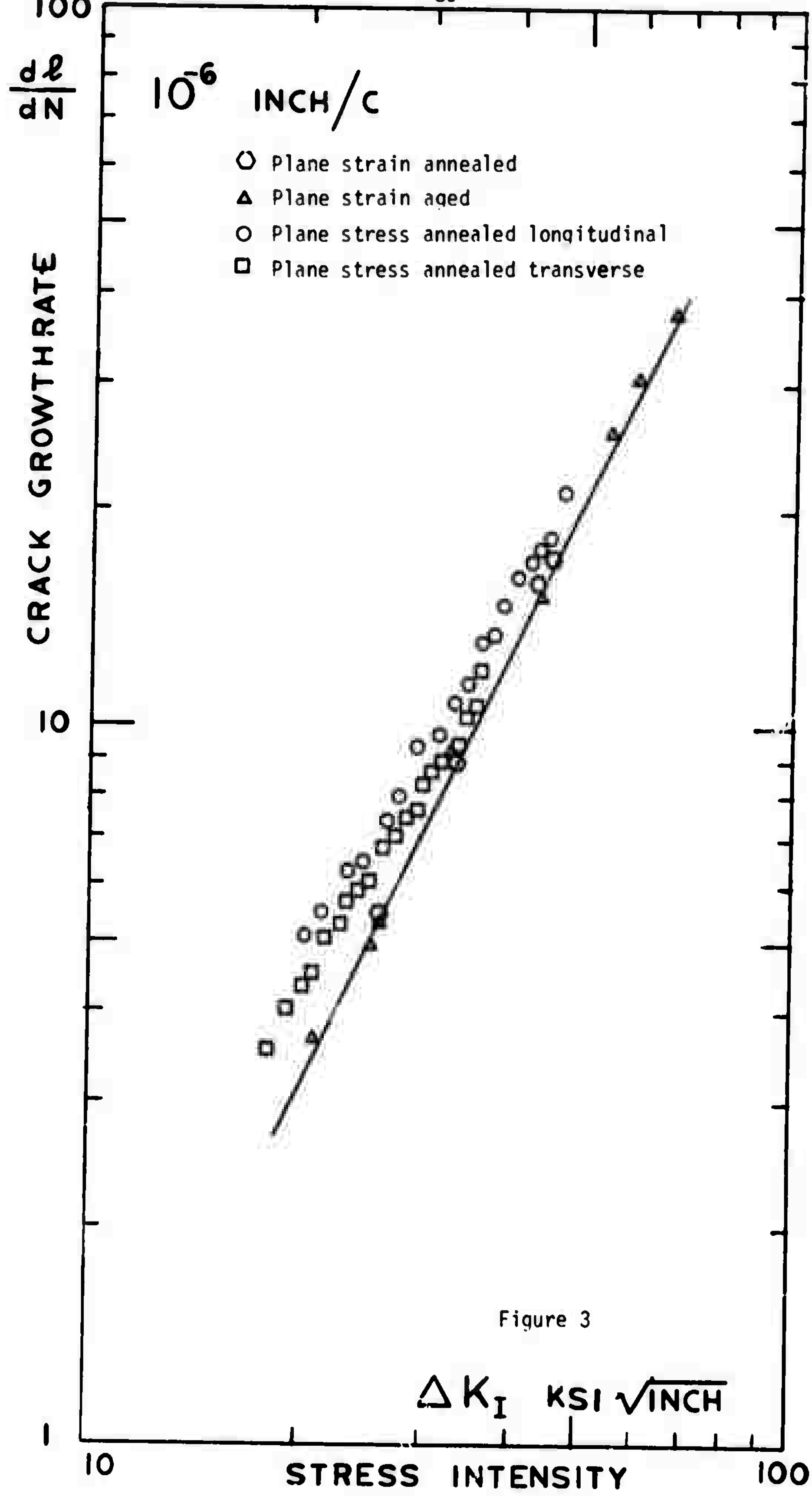
100
$\frac{d\ell}{dN}$
10^{-6} INCH/C
⬡ Plane strain annealed
△ Plane strain aged
○ Plane stress annealed longitudinal
□ Plane stress annealed transverse
CRACK GROWTHRATE
10
1
ΔK_I KSI $\sqrt{\text{INCH}}$
10
STRESS INTENSITY
100

Figure 3

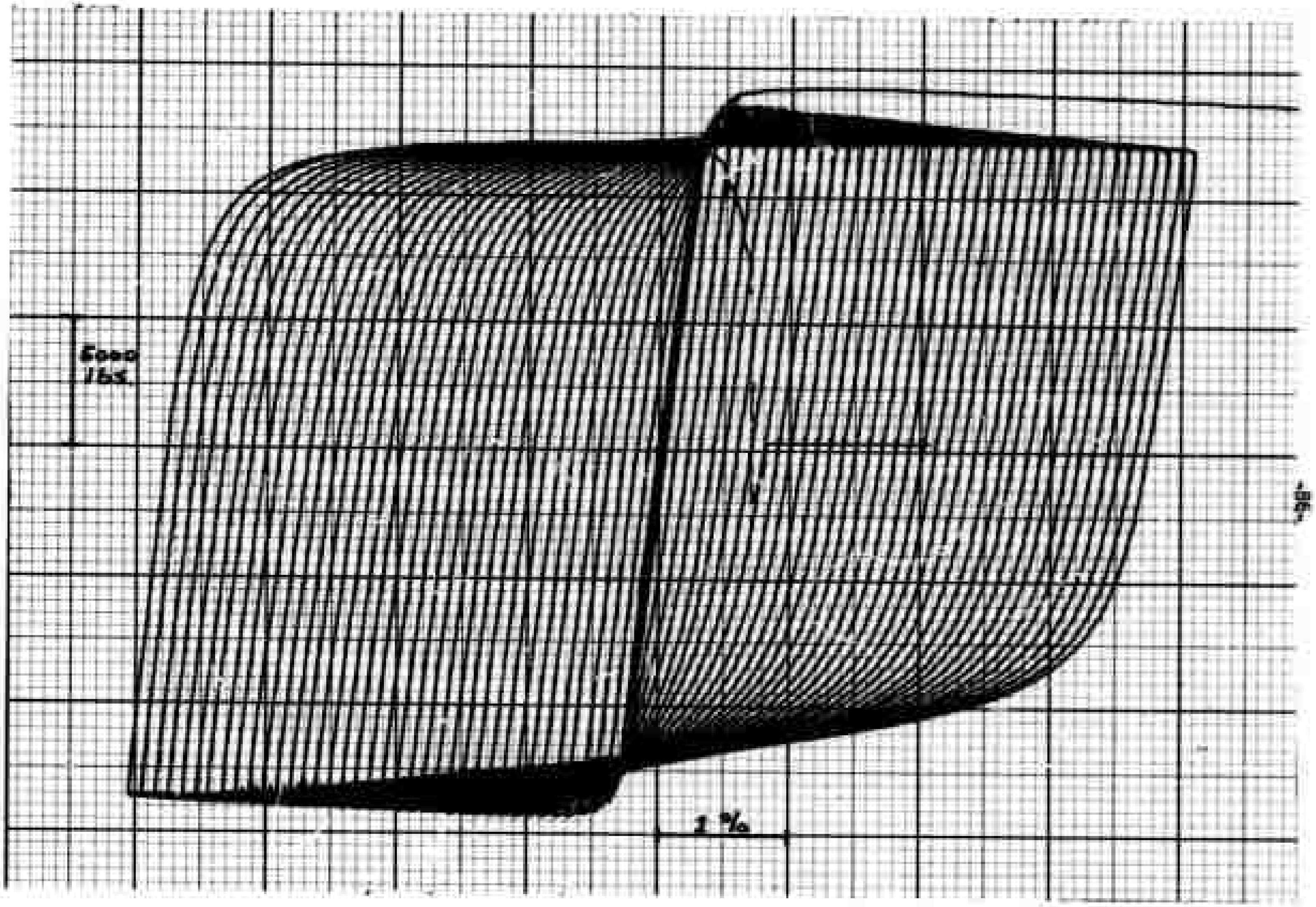

Figure 4 - Stress strain hysterisisloops for aged Vascomax 300. Increasing strain.

THERMOMECHANICAL TREATMENT, MICROSTRUCTURE AND MECHANICAL PROPERTIES OF COBALT-BASE SUPERALLOYS

A. INTRODUCTION

Progress in this program area since the last report[1] includes the following:

New Compositions[2]

(1) A nominal two atom percent HfC-Cobalt base alloy was a) vacuum atomized using dissolved hydrogen gas to break up the melt into droplets (CH7-H2) and b) spin atomized using surface tension to break up a thin molten stream (CH8-C1).

(2) A commercial casting alloy composition, MAR-M-509, was modified by adding more precipitation hardeners (carbon, tungsten and tantalum) and subsequently steam atomized into coarse powders (C52-06).

TMT and Processing

(1) A HIP'ed and hot rolled P/M MAR-M-509 alloy (C51-05-HR) was given a 1 hour at 2250°F anneal and subsequently cross-rolled 40% at 1200, 1400, 1600 and 1800°F, respectively.

(2) All HIP-plus-extruded material (C51-01, C21-01, C52-06, CH2-01-HEH, CH6-H1 and CH7-H2) is being subjected to swage-anneal treatments consisting of alternating cycles of cold swaging 10-15% RA followed by intermediate anneals at 1500°F and 1800°F (plus 2100°F for CH6-H1).

(3) Two P/M MAR-M-509 alloys (C51-03,4 and C51-03) which were HIP'ed and tested according to the previous report[1] were re-HIP'ed at 2325°F and

2300°F for two and four hours, respectively.

(4) High temperature annealing treatments near the incipient melting point of the 3 atom % HfC-Cobalt alloy (CH6-H1) and at the incipient melting point of the P/M MAR-M-509 alloy greatly improved the 1800°F stress rupture property values of these alloys increasing the stress for 100 hour rupture life from 5 to 8.5 ksi and from 2.5 to 11 ksi, respectively.

(5) The 3 atom % HfC-Cobalt alloy is extremely resistant to softening and structural change right up to its incipient melting point of approximately 2450°F.

(6) Warm working (2:1 rolling at 1200, 1400, 1600 and 1800°F) the HIP + hot rolled P/M MAR-M-509 (C51-05-HRR) greatly increased the room temperature yield and ultimate strengths, 150 and 188 ksi to 300 and 308 ksi, but reduced the 1800°F, 8 ksi rupture life from 6 to 1.5 hours.

Structure and Properties

(1) Room temperature hardness, tensile strength and charpy fracture toughness values and elevated temperature tensile and stress rupture values are being determined on all sound alloys after each major TMT or processing change.

(2) Microhardness, X-ray diffraction, differential thermal analysis and metallographic examination are being used to determine structural change and stability as a function of the prior history of each alloy.

(3) Powder metallurgy MAR-M-509 alloy undergoes a massive secondary recrystallization reaction concomitant with solutioning of a carbide phase (possibly $Cr_{23}C_6$) between 2200-2300°F with the large recrystallized grains bounded by finer grains and impurities located along prior particle

boundaries and extrusion stringers.

(4) Extruded product from low oxygen (<500 ppm) steam atomized coarse powders of MAR-M-509 retained its structural integrity after remelting and solidification whereas high oxygen ($\overset{\sim}{>}$1000 ppm) steam atomized and low oxygen hydrogen-vacuum atomized cobalt alloys undergo swelling and distortion when remelted due to the formation of gross porosity.

B. DISCUSSION

New Compositions

The chemical compositions of all cobalt alloys produced to date are summarized in Tables I (without Hf) and II (with Hf).

A modified MAR-M-509 alloy (#C52-06-HE), containing higher amounts of tantalum, tungsten and carbon, was steam atomized into coarse powders and subsequently HIP'ed and extruded (Figure 1). The rapid quenching (atomization) of molten metals should allow for greater quantities of precipitating and solid solutioning constituents to be added without suffering the usual penalties of segregation associated with conventional casting.

Two new cobalt-hafnium alloys were prepared at the two atom percent HfC level but one alloy (CH8-C1) had greater than stoichiometric carbon (0.2 wt % extra) for the purpose of enhancing low-to-intermediate strength via the precipitation of less stable chromium and molybdenum carbides. Additionally, the spin atomization or atomization using surface tension to break up fine molten metal streams into droplets was used for this composition. The other Co-2 atom % HfC alloy, CH7-H2-HE, was a stoichiometric composition providing a complete series of stoichiometric HfC alloys at the 1, 2 and 3 atom percent levels. Probelms encountered with the melting and atomization of the 3 atom percent Co-HfC alloy (CH6-H1-HE) preclude any immediate consideration for going higher in hafnium (>9-10 wt. %) content.

Structure and Stability

One attractive processing route for P/M superalloys is to form wrought-type blanks or preforms by any of the conventional consolidation processes, e.g., HIP, extrusion, rolling, etc.; super plastically form or forge the blank into the final shape and thermally treat the part to restore optimum properties for the intended service application. In some alloys, this processing sequence involves taking a casting alloy composition, making it into wrought product via P/M and finally restoring the cast-type properties by thermally treating. Such is the case with the commercial cobalt base alloy, MAR-M-509, and to a much lesser extent, the cobalt-hafnium alloys.

Some of the heat treatment and hardness data are indicated in Table III. Of particular interest is the MAR-M-509 and the Co-3HfC alloy's response to the one hour anneals. MAR-M-509 appears to soften substantially at ≈2290°F whereas Co-3HfC is reasonably stable up to 2444°F.

It is known that unlike their cast counterparts, the mechanical properties of P/M cobalt base superalloys are drastically affected by thermal treatments (see the next section). X-ray diffraction analysis (Table IV) and differential thermal analysis (Table V) were used to supplement hardness and metallography evaluations. A thorough description of methods and apparatus used will be described in the next report. The differential thermal analysis unit is capable of variable temperature operation up to 1600°C and by suitable calibration (Figure 2) can be operated as a calorimeter over a wide range of heating and cooling rates.

The highlights of an evaluation of P/M MAR-M-509 (C51-01-HE) follows:

Temperature	Comments
R.T.	As HIP + Extruded material is two phase consisting of a fine-grained (3-4μ) matrix (111 texture) containing a 1/2-1 1/2μ precipitate (complex carbide).
R.T. to 2150°F	Slight dissolution of carbide occurs at ≈2150°F with slight increase in the matrix lattice parameter.
2150°F to 2250 ± 25°F	Some softening of alloy occurs as more carbides dissolve, further expanding lattice. Grains and precipitates coarsen uniformly.
2250 ± 25°F to 2350°F	Major carbide solutioning and alloy softening with massive parasitic grain growth (secondary recrystallization) occurs resulting in a 220 texture. Maximum lattice parameter expansion occurs at 2350°F. Gradual degradation of single carbide phase into two phases - one a coarse lamellar phase and the other a dark fine eutectic phase with multi-concave boundaries (Figure 3 and see reference 3 for identification of phases with similar appearance).
2350-2425°F	Incipient melting occurs with maximum 220 texture resulting from parasitic grain growth but max parasite grains stabilize at ≈300μ while min g.s. increases as a function of increasing temperature (to about 70μ). Less alloying elements remained in supersaturated solid solution as temperature increased. Increasing amounts of an additional white phase believed to be Cr_7C_3 formed with increasing temperature (Figure 4). Amount of cast-type structure at grain boundaries increased with temperature.

Temperature	Comments
2425°F	Major phase melting occurred.

All steam atomized MAR-M-509 type alloy compositions behaved similarly except for those with high oxygen (>1000 ppm)contents. The high oxygen alloys were warm worked (rolled 2:1) hardening the alloy from R_c 18 to R_c 53 and released (calorimetrically) about 4 cal/gram at 1150°C (2100°F). Upon melting, a massive grey phase formed giving the appearance of large porosity in the resolidified matrix (Figure 5). It is believed that this phase may be some sort of an oxy-silicate spinel undergoing melting at about 1220°C (2230°F).

The cobalt-3% hafnium alloys exhibited superior stability up to incipient melting at about 2450 at which temperature swelling and gross porosity occur in the matrix. The causes of this porosity and further analysis of the stability of these types of alloys are under current evaluation.

Properties

The room temperature tensile properties of all alloys are shown in Table VI. Note the unusually high strength values for the warm rolled sheet bar (C51-05-HR). The lack of ductility is believed to be due to the high oxygen content in this alloy.

Stress rupture test data are indicated in Tables VII and VIII and plotted in Figures 6 and 7. The beneficial effects of the thermal treatments are evident in both classes of alloys even into the incipient melting region of MAR-M-509. The effect of thermal treatments on the very stable Co-3 atom percent HfC alloy are shown in Figures 8 and 9. Compare the structural change of a 1 hour treatment at 1340°C (2444°F) with that of the as-extruded structure in Figure 8. Observe the significant effect this treatment had on the 10 ksi, 1800°F stress rupture life indicated in Figure 9, going from 3 hours as-extruded to 36 hours after heat treatment at 1340°C.

C. REFERENCES

1. Semi-Annual Technical Report No. 3, Task III, pp. 77-112.
2. Semi-Annual Technical Report No. 4, Tasks I and II, pp. 1-74.
3. M.J. Woulds and T.R. Cass, "Recent Developments in MAR-M-509", Cobalt No. 42, (March, 1969), pp. 3-13.

Table I - MAR-M-509 Cobalt-Base P/M

Alloy Compositions and Processing History

Element Wt. %	C51-LIT- Cast Nominal	C51-01- HE	C51-03,4 H7	C51-03*** H8	C51-04*** H9	C51-05 HR	CZ1-01 HE	C52-06 HE
C	0.6	0.62	see	0.65	0.65	0.52	0.8	0.75
Cr	23.8	25.6		24.0	24.0	24.0	nom	23
Ni	10.0	12.4	next	11.0	11.0	11.0	nom	10
W	7.0	6.9		7.5	7.5	7.5	nom	9
Ta	3.5	2.75	two	4.0	4.0	4.0	nom	5
Zr	0.5	0.35		0.6	0.6	0.6	3.0*	0.5
Ti	0.2	0.14	alloys	0.25	0.25	0.25	nom	0.2'
Si	<0.4	0.8*					0.8*	1.0*
B	0.01*	0.01*		0.05	0.05	0.05	0.01*	
O**		200		900	1000	916	700	400
Bal Co	--	--	--	--	--	--	--	
HIP-T(°F)		2175	2000	2300	2150	2300	2175	
t(hrs)		1	2	2	2	1	1	
p(ksi)		15	28	28.4	26.6	28	15	
EXTR-T(°F)		2000					2000	2050
ratio		15:2					11:1	20:1
ROLL-T(°F)						2100		
RA						6:1		
Re-Process						Cross Roll		
T(°F)						1200,1400 1600,1800		
t(hrs)								
p(ksi)								
RA						2:1		

Table II - Co-Hf P/M and Cast Alloy Compositions and Processing History

Element Wt. %	CH1-A1-Cast	CH1-M1-Cast	CH1-01 Melt Dip	CH2-01 HE	CH3-01*** Powder	CH4-M1 Cast	CH5-01* Powder	CH6-H1 HE	CH7-H2-HE	CH8-C1*** Powder
C	0.24	0.28	0.25	0.20	0.55	0.65	0.58	0.62	0.43	.62
Cr	19.9	18.6	19.9*	20.5	19.0	21.3*	20.0	21.3	20.8	21
Ni	9.2	8.5	9.2*	9.18	8.5	10.2*	9.0	9.9	10.0	10
Mo	5.6	6.8	5.6*	5.5	5.3	5.0*	5.0	5.0	5.7	7
Hf	4.0	2.5	4.0*	2.6	9.4	11.0	11.8	8.9	7.8	6.2
Si	0.02		0.02*	0.84			1.0			
B				0.04*	0.05		0.05			
O**	24	82	49	460	3300	90	2200	310	253	
N								96		
H								10		
Bal Co										
HIP-T(°F)				2100		2275				
t(hrs)				1		2				
p(ksi)				14.5		27.3				
Extr-T(°F)				2000				2000	2050	
ratio				16:1				22:1	20:1	
ROLL-T(°F)						2100				
RA						5:1				
Re-Process				HIP						
T(°F)				2300						
t(hrs)				1						
p(ksi)				27						

* charged to melt except C and O

** in ppm

*** aim composition except C and O

Table III - P/M Cobalt Base Alloys (HIP + Extruded) - Heat Treatment and Hardness Data

Heat Treatment Temp(°F)	time(hrs)	MAR-M-509 (Nominal) C51-01-HE	MAR-M-509 (Hi Zr) CZ1-01-HE	MAR-M-509 (Hi W-Ta-C) C52-06-HE	Co-1HfC (1 atom%) CH2-01-HE	Co-2HfC (2 atom%) CH7-H2-HE	Co-3HfC) (3 atom%) CH6-H1-HE
None-as Extruded		43*/	43*/	43*/	36*/39	35X*/	40X*/
2170°F							
	25	38/41	38X/		32/34		
	120	36/38	37/		30/31		
2190°F	1	38/					
2225°F							
	25	28/34	37X/		27X/30		
	120	31/35	36X/		27/34		
2264°F	1						
2280°F	1	30-40/					
	4	32-34	39/		26/32		
	24	32/39	30/		30/33		
	116						
	120	24/27	26/		25/33		
°F	1	30/					
2300°F	1						
	4						
2336°F	1						
2350°F	1	32/					
	4						
+2300°F	4	31/36	36/31X		/35		
	25	31/30	37/39		/36		
2354°F	1						39/
2372°F	1						
2380°F	1				18/		38/
2390°F	1						
2400°F	16						
2408°F	1				26X/		36X/
2426°F							
	2	26/			10/		34/
	17						
2444°F	1						28X/
2465°F	1						R_B86/
2500°F	1	19/					

*XX/XX first number is R_c hardness number; second number is HK_{500} microhardness converted to equivalent R_c

Table IV - P/M MAR-M-509 -
X-Ray Diffraction Data*

Alloy	Prior History	2θ		Intensity 220/111		$W_{1/2\ max}/Ht$ (111)		$W_{1/2\ max}/Ht$ (220)	
		111	220	(L)	(T)	(L)	(T)	(L)	(T)
C51-01-HE	as extruded	67.3	130.1	1.9	.16	.06	.01	.12	.20
C51-01-HET10.5	2170°F-25 hrs.	67.3	130.1	1.9		.04		.06	
C51-01-HET10.4	2170°F-120 hrs.	67.3	129.9	2.4		.04		.06	
C51-01-HET2	2190°F-1 hr.	67.2	129.8		.22		.01		.16
C51-01-HET11.7	2225°F-25 hrs.	67.3	129.8	1.9		.24		.16	
C51-01-HET11.6	2225°F-120 hrs.								
C51-01-HET21	2264°F-1 hr.	67.2	129.4		1.3		.29		.58
C51-01-HET 7	2280°F-1 hr.	67.1	129.6		.17		.01		.21
C51-01-HET 5	2280°F-1 hr.	67.1	129.4		7.4		.02		.01
C51-01-HET 1	2280°F-1.5 hrs.	67.3	130.4		1.2		.05		.19
C51-01-HET9.3	2280°F-4 hrs.	67.2	129.6	.47		.03		.19	
C51-01-HET9.2	2280°F-24 hrs.	67.2	129.5	.16		.02		.84	
C51-01-HET9.1	2280°F-120 hrs.	67.3	129.4		1.0		.065		.42
C51-01-HET13A6	2280°F-120 hrs. A6	67.4	130.3	1.42		.035		.08	
C51-01-HET8	2290°F-1 hr.								
C51-01-HET8A4	2290°F-1 hr. A4	67.4	130.4	.66		.23		.71	
C51-01-HET22	2300°F-1 hr.	67.3	129.7		.51		.31		.74
C51-01-HET16	2300°F-4 hrs.	67.2	129.6		9.6		.054		.02
C51-01-HET23	2336°F-1 hr.	67.2	129.6	2.6		.11		.33	
C51-01-HET4	2350°F-1 hr.	67.0	129.1		23.4		.085		.017
C51-01-HET4A5	2350°F-1 hr. A5	67.4	130.2		4.4		.25		.36
C51-01-HET24	2354°F-1 hr.	67.1	129.6		.38		.06		1.5
C51-01-HET27	2380°F-1 hr.	67.0	129.3	.29		.032		.58	
C51-01-HET27A6	2380°F-1 hr. A6	67.4	130.3	1.00		.19		.51	
C51-01-HET28	2408°F-1 hr.	67.0	129.4		1.32		.04		.11
C51-01-HET29	2426°F-1 hr.	67.2	129.6	.55		.02		.13	
C51-01-HET29A6	2426°F-1 hr. A6	67.3	130.2	.59		.03		.22	
C51-01-HET3	2500°F-1 hr.	67.1	129.3		10.0		.12		.024

Table IV - P/M MAR-M-509 -
X-Ray Diffraction Data* (cont'd)

Alloy	Prior History	2θ		Intensity 220/111		W/Ht (111)		W/Ht (220)	
		111	220	(L)	(T)	(L)	(T)	(L)	(T)
C51-01	Cold Working								
C51-01-HET5	2280°F-1 hr.	67.1	129.4		7.4		.02		.01
C51-01-HET5S30	2280°F + swage 30%	67.3	130.0		.22		.02		.45
C51-01-HET5S41	2280°F + swage 41%	67.2	130.5		.10		.01		1.5
C51-01-HET5S41A10	2280°F + swage + A10	67.4	130.8		.10		.01		1.4
C51-01-HET5S41A2	2280°F + swage + A12	67.4	130.8		.11		.01		0.33
C51-01-HET5S41A4	2280°F + swage + A14	67.6	130.5		.34		.01		0.10
C51-01-HET5S41A6	2280°F + swage + A16	67.5	130.5		.45		.01		.11
C51-03,4-H7	HIP 2 hrs. at 2000°F	67.4	130.5	.59	1.84	.01	.03	.08	.07
C51-04-H9	HIP 2 hrs. at 2150°F	67.5	130.4	1.14	4.4	.02	.02	.08	.02
C51-03-H8	HIP 2 hrs. at 2300°F	67.3	130.1	.80		.03		.11	
C51-03-H8T27	HIP 2 hrs. + 1 hr. at 2380°F	66.9	129.5	1.51		.07		0.13	
C51-05-HR	HIP + ROLLED 6:1 at 2100°F	67.6	130.2	.06	.10	.01	.01	.095	.33
C51-05-HR	HIP + 1 hr. at 2264°F	67.2	130.1	.80		.05		.24	
C51-05-HR	HIP + 1 hr. at 2300°F	67.3	129.8	1.59		0.02		.045	
C51-05-HR	HIP + 1 hr. at 2336°F	67.3	129.9	5.33		.06		.03	

* Cr K_α,3°, MR, 0.2° SLIT,40 KV, 20 ma,2°/in/min.
Calculated average intensities for random fine grain structure 200/111=.47, 220/111=.78

Table V

Cobalt-Base Alloys - Differential Thermal Analysis

HEATING ANALYSIS*

Alloy	DTA run #	Temp. range of interest	Temperature Scale °C/min	Temperature rate °C/min	1st Effect Temp. °C	1st Effect Energy cal/gm	2nd Effect Temp. °C	2nd Effect Energy cal/gm	Major Melting Temp °C	Major Melting Energy cal/gm	PEAK TEMPERATURE** T °C	PEAK TEMPERATURE** time hrs.	PEAK TEMPERATURE** cool °C/min
MAR-M-509 Extruded													
C51-01-Powder	23	1000-1550	1	10	1070X	0.1	1265N	4.1	1296	≈80	1550		10
C51-01-HE	29	900-1475	1	10	1184N	4.2	1285N	0.8	1303	>40	1475		10
C51-01-HE	30	900-1310	1	10	1152N	0.1	1256N	5.7			1296	1	N_2
***C51-01-HE	36	750-1290	0.2	10	1080X	1.1	1175N	3.1			1280	.5	N_2
C51-01-HE	37	750-1280	0.1	10	1173N	<0.1	1220N	0.2			1270	.5	N_2
C51-01-HE	38	750-1330	1.0	10	1170N		1274N	10.0			1317	.5	N_2
C52-06-HE	27	1000-1475	1	10	1170N	0.4	1290N	9.5	1328	>40	1475		10
C52-06-HE	28	900-1475	2	10	N.O.		1267N	19	1343	≈23	1475		10
2nd cycle	28	900-1475	2	10	N.O.		1256N	7.2	1328	>20	1475		10
MAR-M-509 Rolled													
C51-05-HRR1	32	820-1450	2	20	1166X	4.0	1292X	1.8	1400	>20	1450		20
2nd cycle		820-1450	2	20	1227N	≈4	1339N	≈2	1390	>20	1450		20
C51-05-HRR2	33	830-1450	2	20	1144X	≈4	1288X	3	1394	>20	1450		20
2nd cycle		830-1450	2	20	1227N		N.O.		1382		1450		20
C51-05-HRR3	34	830-1380	0.2	20	1152X	3	1285X	2			1362	.03	N_2
C51-05-HRR4	35	830-1320	0.1	20	1148X	4					1287	.01	N_2
Co-HfC Extruded													
2 atom % HfC													
CH7-H2-HE	24	1000-1500	1	10	1123N	<.1	1216N	<.1	1337	>20	1500		10
2nd cycle	25	1000-1475	1	10	1100X	≈.1	1220?	<.1	1306	>20	1475		10
CH7-H2-HE	25	1000-1475	1	10	1123X	.6	1206X	≈.3	1310	>20	1475		10
2nd cycle		1000-1500	1	10	N.O.		1252N	≈.3	1318	>20	1500		10
CH7-H2-HE	26	1000-1475	1	10	N.O.		1220N	≈.3					
3 atom % HfC													
CH6-H1-HE		820-1450	2	20	N.O.		N.O.		1360	>20	1450		20
2nd cycle		820-1450	2	20	1238N	.4	1263N	1.5	1339	>20	1450		20

* N=endothermic, X=exothermic, N.O.=none observed

** Time of peak temperature is several minutes when programmed cooling rates are used. N_2=quenched using liquid N_2 vapors after holding at peak temperature for indicated time period (≈ 40°C/sec)

*** All tests run under flowing argon except DTA Run #36.

Table VI

Cobalt Alloys-Room Temperature Tensile Properties

Alloy	Prior History	YS 0.2% KSI	UTS KSI	Elong. %	R.A. %
P/M MAR-M-509					
C51-01-HE	HIP,EXTR.	135	190	11	8
C51-01-HE	HIP,EXTR.	123	195	17	14
C51-01-HET13A6*	HIP,EXTR., 116 hrs. at 2280°F	94	166	11	8
C51-01-HET25A6	HIP,EXTR., 1 hr. at 2354°F	92	120	1	1
C51-01-HR(Long.)	HIP,ROLLED 6:1 at 2100°F	150	188	2	2
C51-01-HR(Trans.)	HIP,ROLLED 6:1 at 2100°F	155	193	2	2
C51-01-HRR1	HIP,CROSS-ROLLED + 2:1 at 1800°F	239	251	<2	nil
C51-01-HRR2	HIP,CROSS-ROLLED + 2:1 at 1600°F	271	271	<1	nil
C51-01-HRR3	HIP,CROSS-ROLLED + 2:1 at 1400°F	305	307	<1	nil
C51-01-HRR4	HIP,CROSS-ROLLED + 2:1 at 1200°F	298	308	<1	nil
CZ1-01-HE	HIP,EXTR (HiZr)	129	188	6	7
C52-06-HE	HIP,EXTR. (Hi W,Ta,C)	138	182	3	2
P/M Co-HfC 1 atom % HfC					
CH2-01-HE	HIP,EXTR.	98	142	4	6
CH2-01-HEH1	HIP,EXTR.,ReHIP 4 hrs. at 2200°F	97	137	11	10
CH2-01-HEH2	HIP,EXTR.,ReHIP 1 hr. at 2300°F	70	111	5	5
CH2-01-HEH2T15	HIP,EXTR.,ReHIP + 4 hrs. at 2350°F	100	130	9	5
2 atom % HfC					
CH7-H2-HE	HIP,EXTR.	105	154	7	5
3 atom % HfC					
CH6-H1-HE	HIP,EXTR.	132	187	4	4
CH6-H1-HET26T34	HIP,EXTR. + 17 hrs. at 2426°F	75	104	8	7
Cast Co-HfC 3 atom % HfC					
CH4-M1-CRA6	CAST,ROLLED 5:1 at 2100°F	148	170	12	8

* A6 = aged 1600-1650°F for 20 hours.

Table VII

Stress Rupture Data-1800°F

Alloy	Prior History	Stress (Initial) KSI	Rupture Life hours	Rupture Ductilities	
				Elong.	R.A.
P/M MAR-M-509					
C51-01-HET16A6*	HIP,EXTR., + 4 hrs. at 2300°F	6	170	7	1
		10	2.4	50	38
C51-01-HET16T24A6	HIP,EXTR., + 1 hr. at 2354°F	10	137	4	4
		15	9.3	14	9
C51-01-HET25A6	HIP,EXTR., + 1 hr. at 2354°F	15	11.5	9	2
C51-05-HR	HIP,ROLL 6:1 at 2100°F	8**	6	-	-
C51-05-HRR1	HIP,ROLL 6:1 + roll 2:1 at 1800°F	8	2.2	24	10
C51-05-HRR2	HIP,ROLL 6:1 + roll 2:1 at 1600°F	8	0.9	21	14
C51-05-HRR3	HIP,ROLL 6:1 + roll 2:1 at 1400°F	8	1.2	43	23
C51-05-HRR4	HIP,ROLL 6:1 + roll 2:1 at 1200°F	8	1.3	26	18
P/M Co-HfC					
1 atom %					
CH2-01-HEH2T15A6	HIP,EXTR., HIP at 2300°F + 4 hrs. at 2350°F	6	1,170***	16	11
		8	30	50	18
		10	14	20	6
2 atom %					
CH7-H2-HE	HIP,EXTR.	5	39	78	37
		10	2	70	38
3 atom %					
CH6-H1-HE	HIP,EXTR.	5	104	52	29
		10	3.3	84	65
		15	0.4	82	60
CH6-H1-HET 28	HIP,EXTR. + 1 hr. at 2408°F	10	10.7	58	36
CH6-H1-HET 29	HIP,EXTR. + 1 hr. at 2426°F	10	22.6	48	32
CH6-H1-HET 32	HIP,EXTR. + 1 hr. at 2444°F	10	36.2	34	20
CH6-H1-HET 26T34	HIP,EXTR. + 17 hrs. at 2426°F	10	8.3	18	7

* A6=Aged 20 hrs. at 1600-1650°F

** Interpolated from prior data

*** Temp. varies from 1700 to 1800°F.

Table VIII Cobalt Alloys - 1800°F, 100 Hour Life Stress Rupture Data

	Stress (ksi)	Elong.
MAR-M-509		
HIP + EXTR.	2.5	50-120
HIP + ROLL	3.8	20
HIP + EXTR. + 116 hrs at 2280°F	4.8	40
HIP + EXTR. + 1 hr at 2290°F	7.5	10
HIP + EXTR. + 1 hr at 2350°F	11	4-14
Hi Zr Modification		
HIP + EXTR.	4.8	40
Hi W, Ta, C Modification		
HIP + EXTR.		
Co-HfC Alloys		
HIP + EXTR.		
1 atom % HfC	4	30-70
2 atom % HfC	4	≈70
3 atom % HfC	5.2	50
HIP + EXTR. + Heat Treat		
*1 atom % HfC	6.5	≈30
**3 atom % HfC	≈8.5	-

---

* re-HIP 1 hr. at 2300°F, additional heat treatment 4 hrs. at 2350°F did not affect.

** estimated based on 10 ksi, 1800°F life of 36 hours after 1 hour at 2444°F.

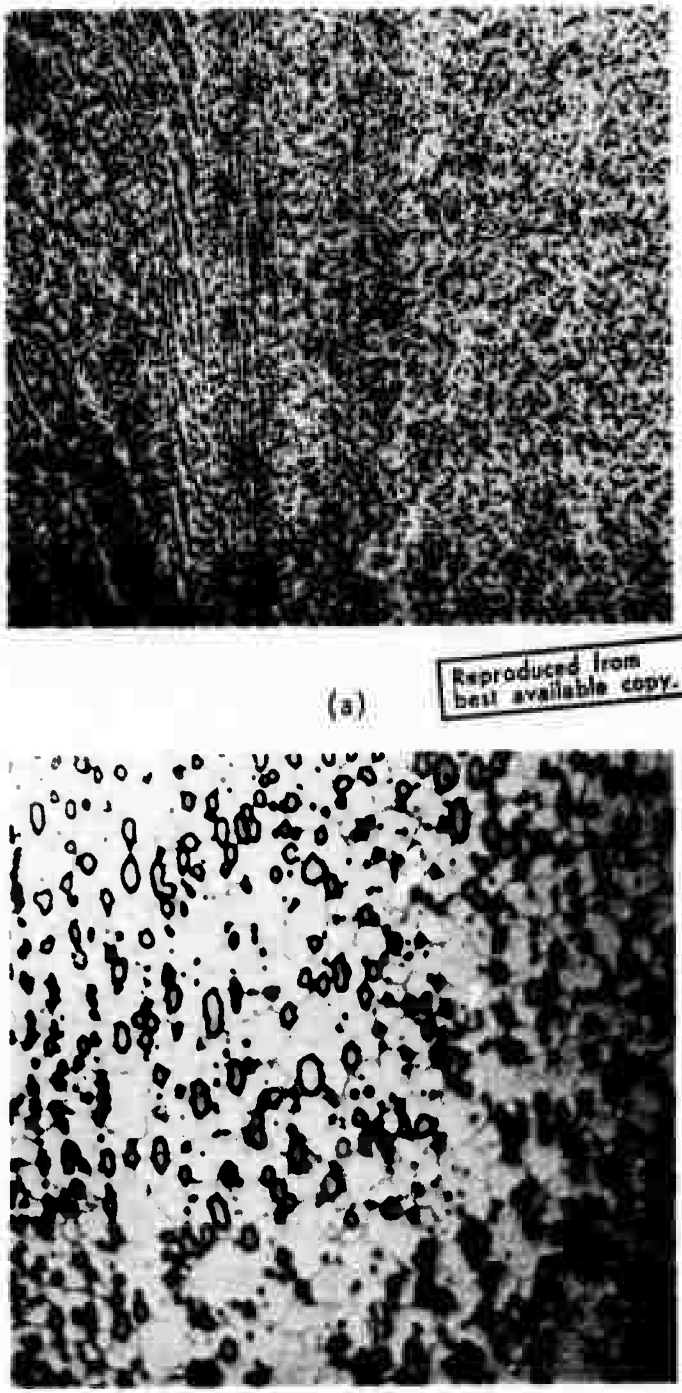

(a)

(b)

Figure 1 - As HIP + Extruded MAR-M-509 alloy modified with additional tantalum tungsten and carbon (0.75 wt. %). Longitudinal section. Etched. (a) 300X, (b) 1500X.

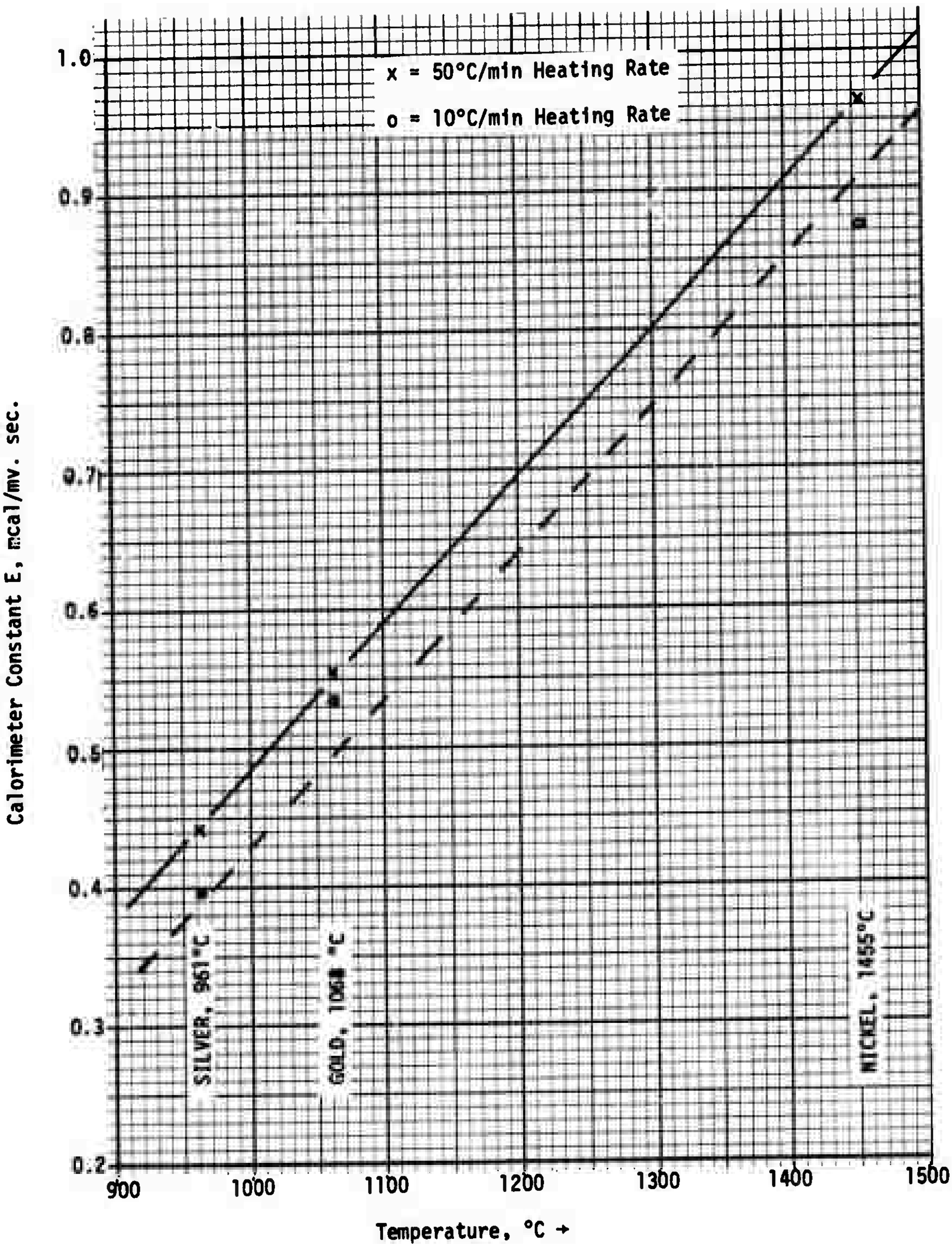

Figure 2- Heat Flow Constant Calibration Curve for 1600°C DTA Cell at Two Heating Rates (10 and 50°C/min.).

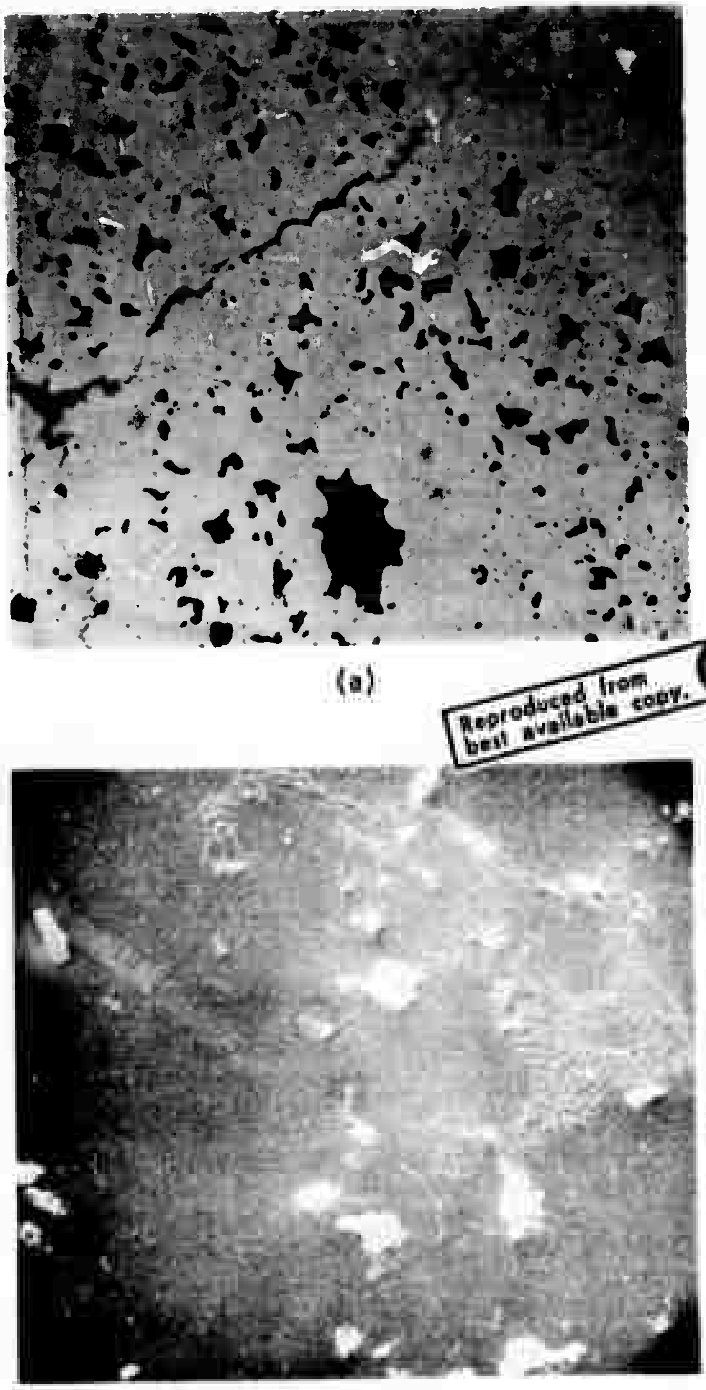

(a)

(b)

Figure 3 - $M_{23}C_6$ phases in P/M MAR-M-509, (a) After holding at 1296°C (2365°F) for 1 hour followed by N_2 vapor quench. Etched. 750X. (b) SEM profile of modified MAR-M-509 alloy after remelting. Etched. 500X.

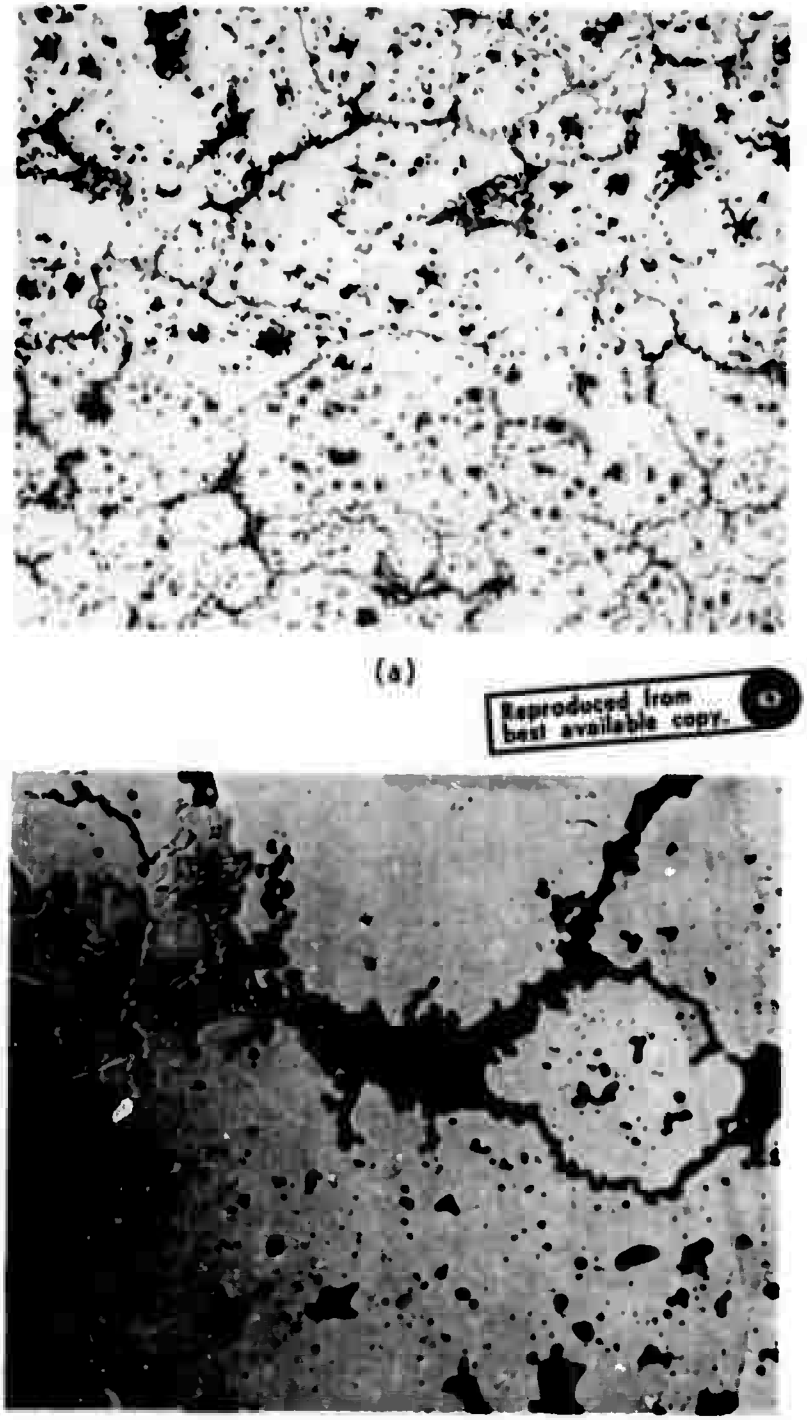
(a)

(b)

Figure 4 - P/M MAR-M-509 alloy after holding 2 hours at 1330°C (2426°F) and air cooled. (a) Etched. 150X. (b) Etched to reveal four major types of phases after partial melting. 750X.

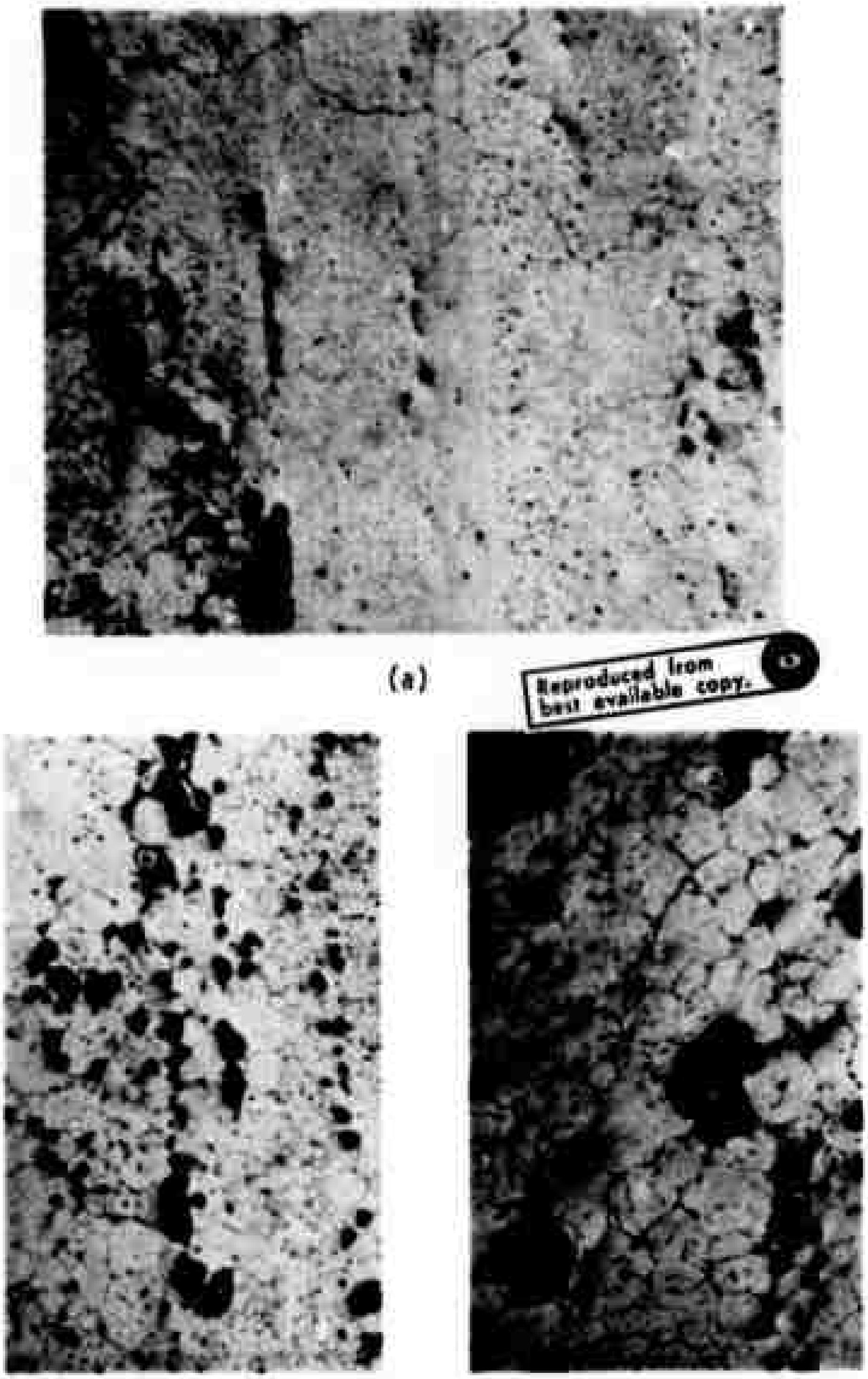

(a)

(b)

(c)

Figure 5 - Porosity and massive grey phase forming in high oxygen (≥1000 ppm) HIP + hot rolled P/M MAR-M-509 after holding 2 hours at (a) 1240°C (2264°F), (b) 1260°C (2300°F), and (c) 1280°C (2331°F). Etched. 150X.

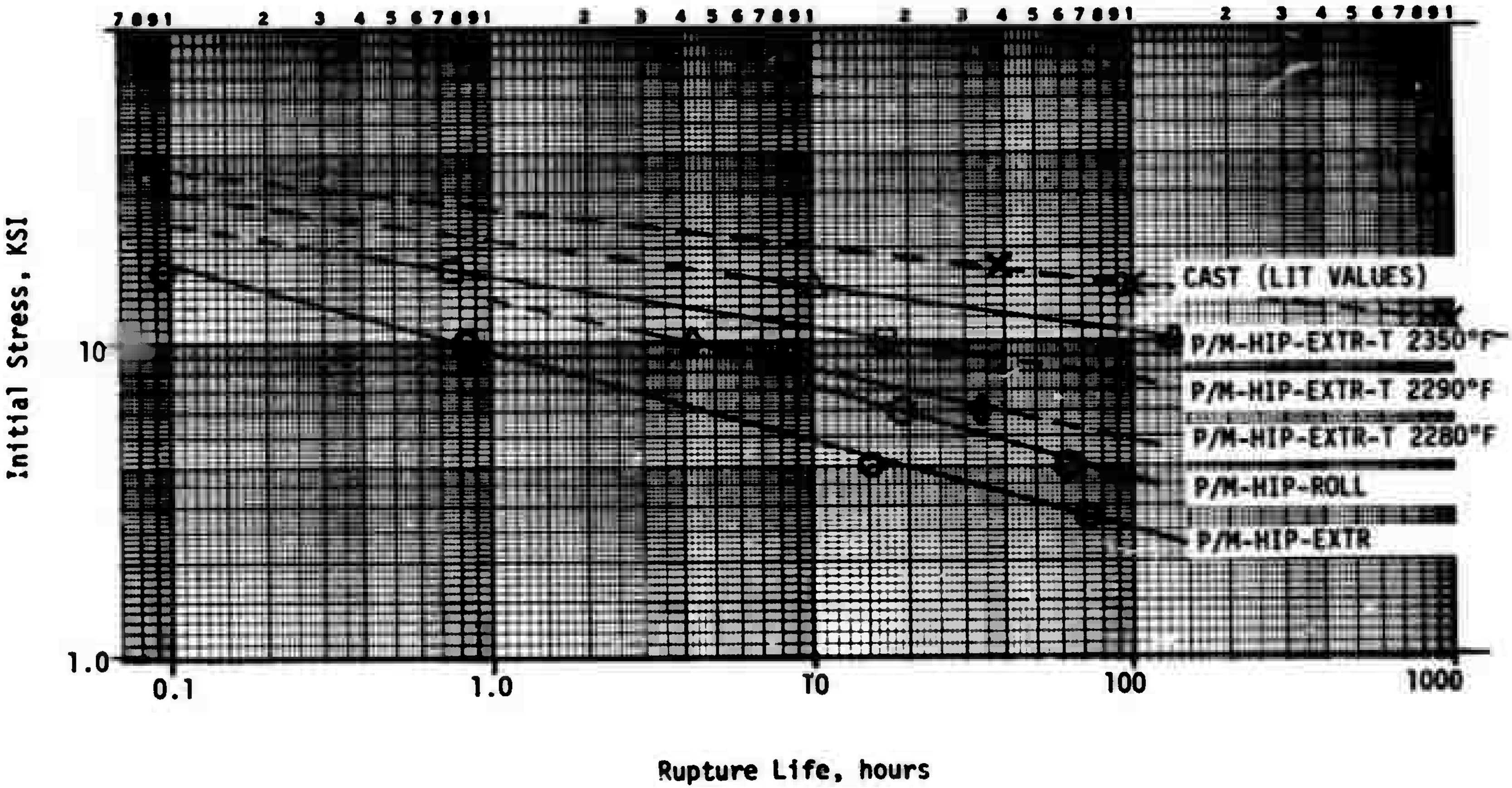

Figure 6
MAR-M-509 Stress Rupture Data at 1800°F

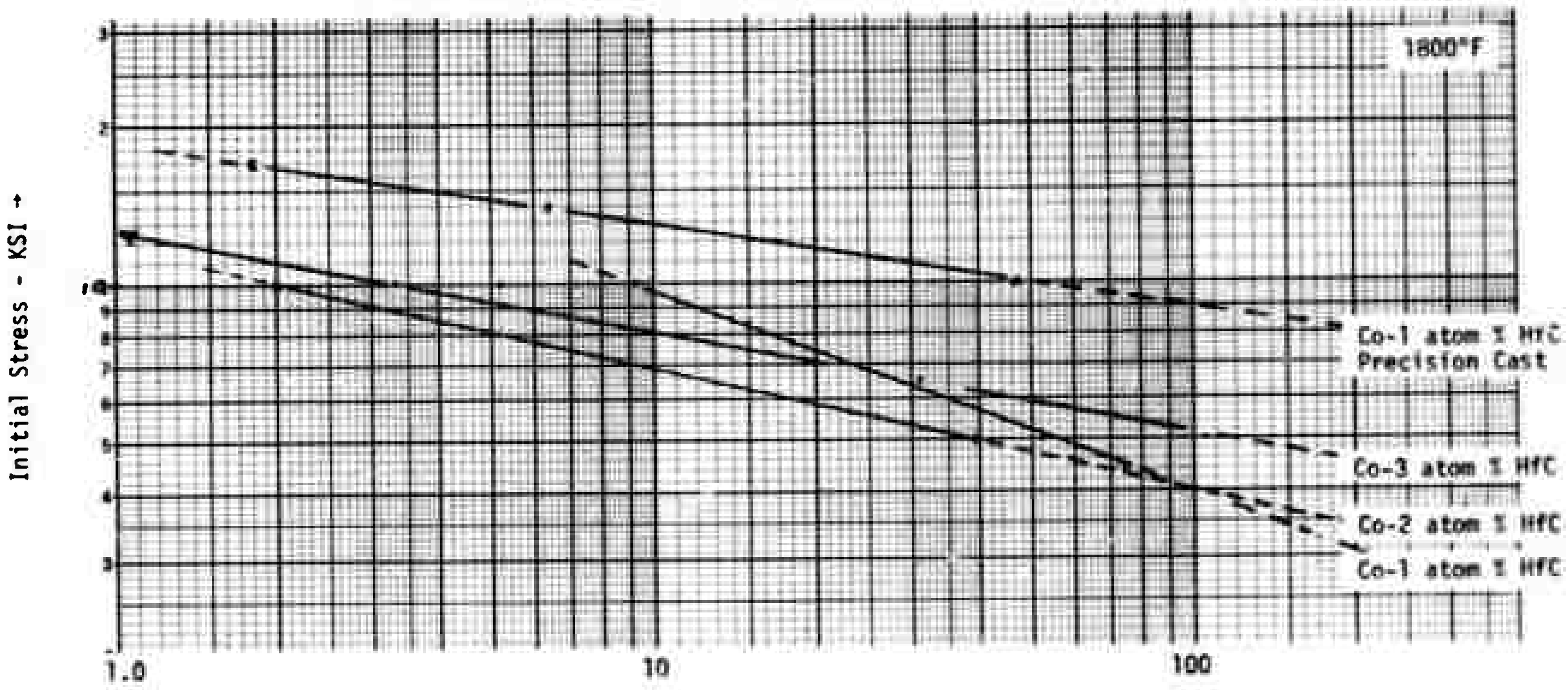

Rupture Life, hours →

Figure 7
Stress Rupture Curves for P/M Co-HfC Alloys in the HIP + Extruded Condition

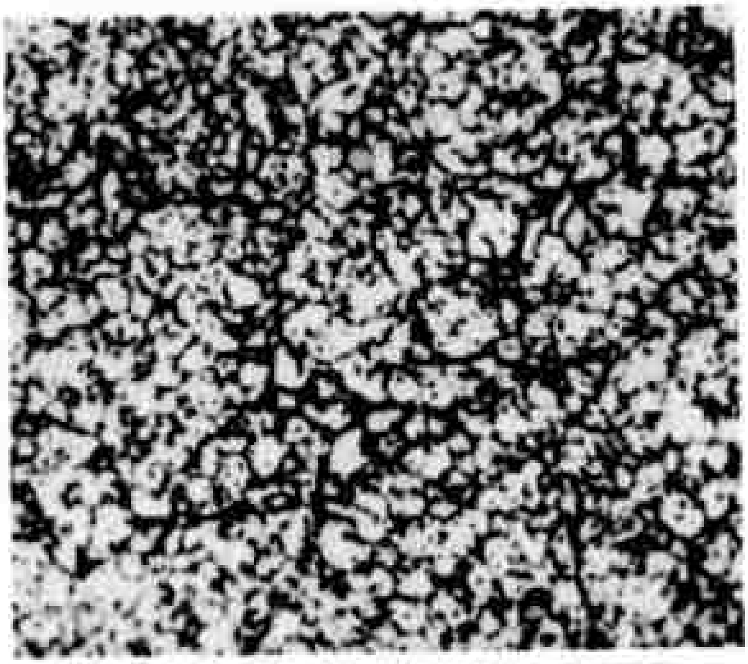

(a)

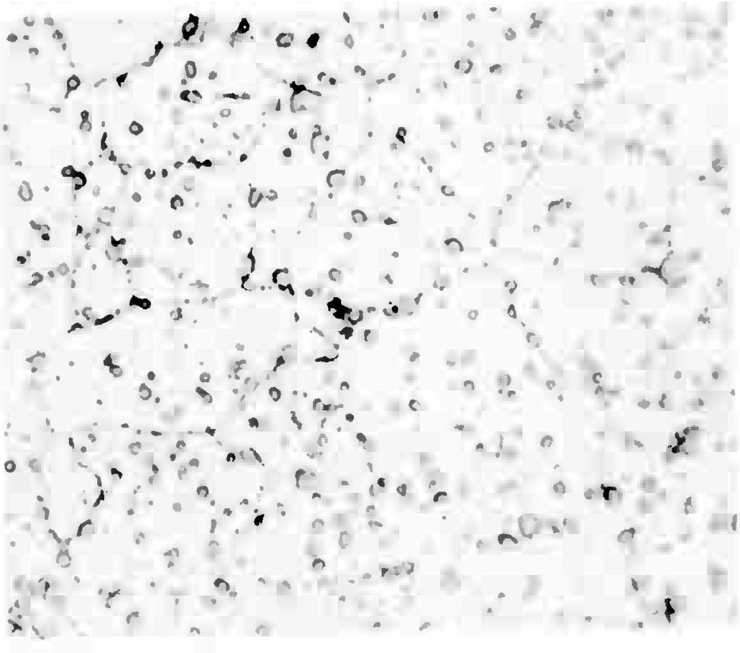

(b)

Figure 8 - HIP + Extruded P/M Co-3 atom % HfC alloy in (a) as extruded condition and (b) after 1 hour at 1340°C (2444°F) and air cooled. Etched. 1500X.

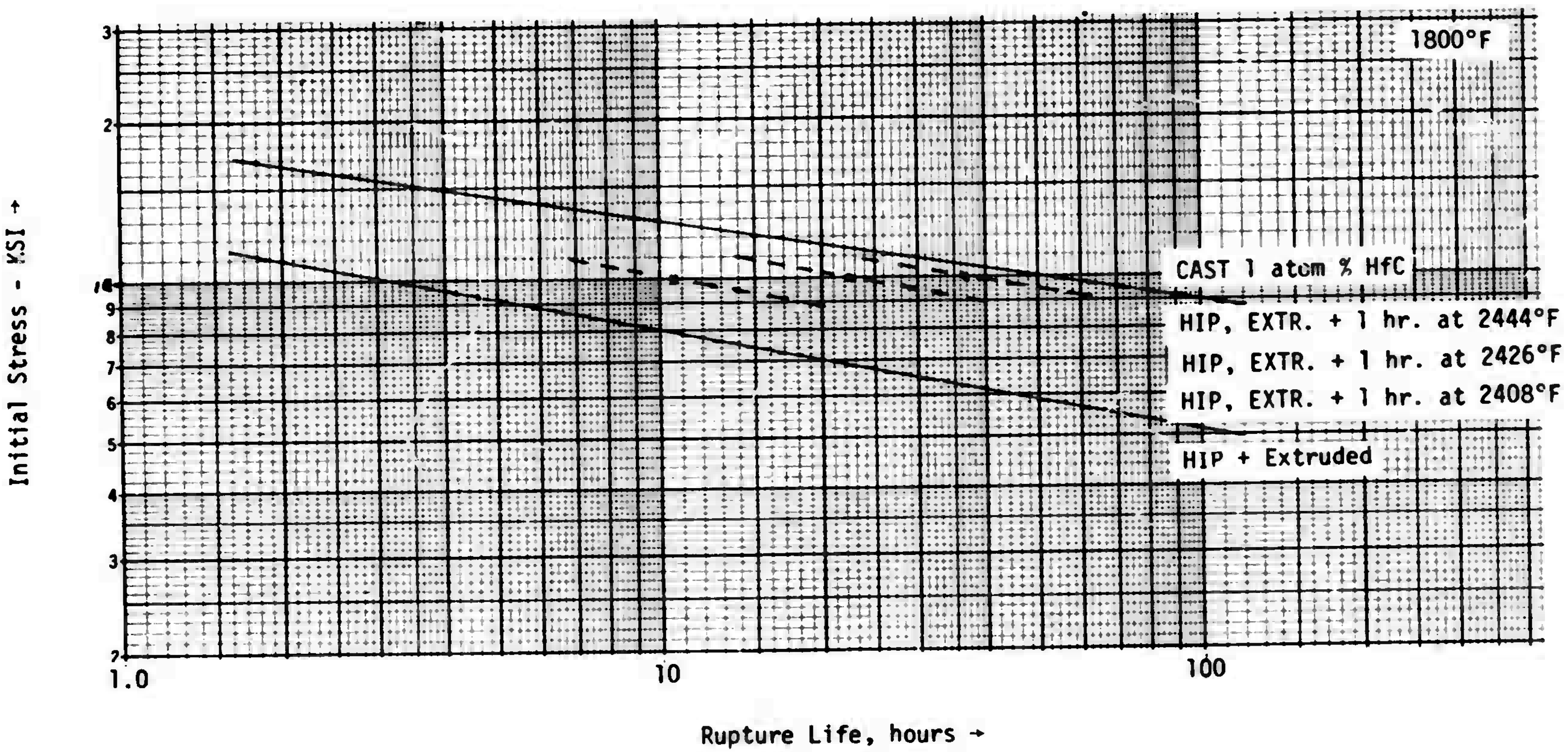

Figure 9
Effect of 1-hour Coarsening Treatments on 10 KSI Rupture Lives of Co-3 atom % HfC Alloy

DUCTILE FRACTURE EXPERIMENTS ON SPHEROIDIZED MEDIUM CARBON STEEL IN COMBINED TENSION AND TORSION

by

M.M. Salama, R.M. Pelloux and A.S. Argon

A. INTRODUCTION

Ductile fracture has been recognized to be a micromechanics plasticity problem in plastic matrices with more or less deformable inclusions[1]. The process consists of two fundamental parts: a) nucleation of holes by the separation of inclusions from the plastically deforming matrix, b) plastic growth of the nucleated inclusions followed by development of tensile or shear localization zones. Some progress has been made by modelling the hole nucleation stage around the hypothesis that a critical tensile stress is required across at least part of the inclusion-matrix surface to initiate tensile cavitation which is produced by a plastic drag of the less deformable inclusion on the plastically deforming surroundings[2]. The experiments to be described below investigate the effect of changing deformation conditions resulting from changing directions of principal plastic strain on the nature of the hole nucleation and growth process. Based on the earlier work of Backofen, et.al.[3], the combination of tension and torsion was chosen as the mode of the experiments.

B. EXPERIMENTAL PROCEDURE

After some preliminary experiments with hot isostatically pressed atomized maraging steels it was decided to experiment with a more readily available and less expensive spheroidized medium carbon (1045) steel. As demonstrated earlier[2], this material is ideally suited for such experiments in that it furnishes a nearly equiaxed, non-deformable iron carbide inclusion in a ductile iron matrix of relatively low strain hardening capacity.

Bars of 3/4" diameter of 1045 steel were spheroidized by just quenching-in a very fine lamellar martensite from 900°C followed by ageing for several days at 700°C. The iron carbide inclusions obtained in this way are shown in Figure 1. The inclusions are relatively equiaxed. The size distribution of the carbide inclusions was determined and is given as a frequency distribution of sizes in Figure 2. The average grain size of the matrix was around 5 microns. Their shapes were also equiaxed. The stress strain curve of the spheroidized steel is given in Figure 3. Since the mean spacing between particles is of the order of tens of microns, no rise of flow stress should result from the particles. A certain small amount of increase of strain hardening rate due to elimination of displacement incompatibilities around the carbide particles is inevitable. This will be ignored and the stress strain curve of Figure 3 will be taken as the plastic resistance of the unhindered plastic matrix.

Tests were performed with conventional tensile and solid bar torsion specimens. Tensile tests were carried out on an Instron machine, while the torsion tests were done on a specially instrumented lathe with a strain gauge equipped torque dynamometer in the fail-stock.

The axial force was regulated to be zero during the torsion tests to avoid development of axial forces resulting from changing of specimen length which can result from the development of plastic anisotropy. The strain rates were in the range of 10^{-2} sec^{-1} in both types of tests.

C. EXPERIMENTAL RESULTS

The types of experiments which were performed are listed in Table I, and the collection of the majority of the fractured specimens is given in Figure 4.

The pure torsion test (#1) was of interest for the study of hole nucleation around the inclusions in a simple shear field free of a macroscopic dilational tri-axial stress component. Not surprisingly the fracture surface was typical of ductile torsion fractures with a fracture plane angle $\alpha=0$ from the plane normal to the specimen axis. The sheared torsion bar was sectioned along the axis for the study of separated inclusions. No significant number of separated inclusions were found away from the sheared-off surface. In view of the fact that section in the plane of principal tensile extension might have been more discriminating for revealing separated inclusions, the experiment is considered inconclusive-though not inconsistent with the expectations of minimal growth of separated inclusions. Although no detailed study could be made of the shear localization process leading to separation, it is suspected that it is of the type analyzed by McClintock, et.al.[4]. The scanning electron micrograph of the fracture surface of this specimen (Figure 5) shows that although the dimples are strongly elongated in the direction of maximum tensile extension, localization and separation have occurred on a plane normal to the specimen axis.

Specimens 2-4 were initially strained in torsion to steadily increasing torsional pre-strains followed by separation in tension. As shown in Figure 6 and also in Table I, increasing torsional pre-strain reduces the required subsequent tensile strain for fracture indicating that a certain amount of hole growth and cavitational localization has occurred in torsion in the absence of a deliberately applied dilational stress component. The geometric evidence of the production of damage in torsion is the angle α of the fracture surface with the plane normal to the specimen axis. These angles α given in Table I correlate closely with the complement to the total angle of shear and demonstrate that some localization occurs early on planes of maximum shear which then persist as the planes of continuing damage as they are rotated around by shear. Further localization and eventual tensile separation occurs on these planes. The rise in the tensile fracture stress of the torsion-tension tested specimens over the fracture stress in the specimens tested in tension alone, shown in Figure 6 is a result of the additional strain hardening in the former specimens which have equivalent strains to fracture that are about 25% higher than those of the latter. The fracture surface dimples of specimens 2-4 show little distortion and are more typical of those in tension specimens, indicating that the final stages of hole growth under a dilational tri-axial stress has largely erased any distortion of the shear deformation.

One specimen (#5) was twisted forward and backward by a shear strain of 0.82 followed by final separation in tension. Since the shear damage zones in these specimens are parallel after the torsion cycle there is little reduction the the subsequent tensile strain from that in a specimen fractured in tension alone. Furthermore, as Figure 4 shows the fracture surface is a normal cup-and-cone and has no helicoidal nature at all. This suggests that if the shear localization zones generated by the initial pre-twisting cycle are parallel to the tensile axis they are almost completely ineffective in nucleating tensile localization zones. Consequently, the final equivalent strain to fracture in this specimen was the largest of all.

Specimens 6-8 were tested in tension alone and were used for a quantitative study of the dependence of hole nucleation on triaxial stress. Specimen 6 which fractured and 7-8 which were not carried all the way to fracture were sectioned axially and examined in the scanning electron microscope. The change in the fraction of separated inclusions of the total number present are plotted for the three specimens in Figure 7 as a function of the distance away from the median plane. The three curves demonstrate that as the neck becomes increasingly acute the triaxial stresses rise in the center of the specimens more and more inclusions separate. Finally at fracture fully 55% of all inclusions show separation from the matrix. Visual examination disclosed that the separated inclusions are preferrentially the large ones, and then primarily those large inclusions which have as nearest neighbors other large inclusions. Comparison of these results with the frequency distribution of Figure 2 suggests that inclusions with a size less than 0.85 micron are not very effective in nucleation of holes in spheroidized steel.

D. DISCUSSION OF RESULTS

The experiments discussed above demonstrate clearly that the process of hole growth and cavitational localization is clearly a path dependent process in which the dilational tri-axial stress is not the only important parameter. The large tensile strain to fracture in the specimen which was subjected to a half cycle of torsional shear is a clear demonstration of this. Although hole nucleation can occur in a dilation-free, stress state, it is not generally appreciated that localization of deformation can also occur in shear where the central process must clearly be a reduction of load carrying capacity in a zone in which a sizeable fraction of inclusions have separated. If this zone is not entirely planar it is quite possible that local dilational stresses could be set up across the somewhat inclined planes of localization as deformation stays preferrentially on them.

These experiments demonstrate clearly that ductile fracture can not be successfully characterized by any single criterion based on a deformation state but requires the solution of the incremental micromechanics plasticity problem of hole growth.

E. REFERENCES

1. F.A. McClintock and A.S. Argon, Mechanical Behavior of Materials, Addison Wesley, Reading, Massachusetts (1966).

2. A.S. Argon and J. Im, Semi-Annual Technical Report No. 2 ARPA Contract No. DAHC15-70-C-0283, (Task IV, p. 124) (1971).

3. W.A. Backofen, A.J. Shaler and B.B. Hundy, Trans. ASM, 46, p. 655 (1954).

4. F. A. McClintock, S.M. Kaplan and C.A. Berg, Int. J. Fracture Mech., 2, p. 614, (1966).

Table I - Summary of Experiments

Specimen Number	Testing Procedure	Max. Shear Pre-Strain	Tensile Post-Strain	Total Equivalent Strain to Fracture	α	α' $\frac{\pi}{2}-\tan^{-1}\gamma$
1	torsion	1.47	0	0.85	0	1.20
2	torsion-tension	0.39	1.08	1.30	1.22	1.04
3	torsion-tension	0.82	0.83	1.30	1.05	0.80
4	torsion-tension	0.95	0.35	0.90	0.79	
5	torsion-reverse-tension	±0.82	1.02	1.97		
6	tension	0	1.16	1.16		
7	tension	0	0.57	0.57*		
8	tension	0	0.38	0.38*		

* Test not carried to fracture.

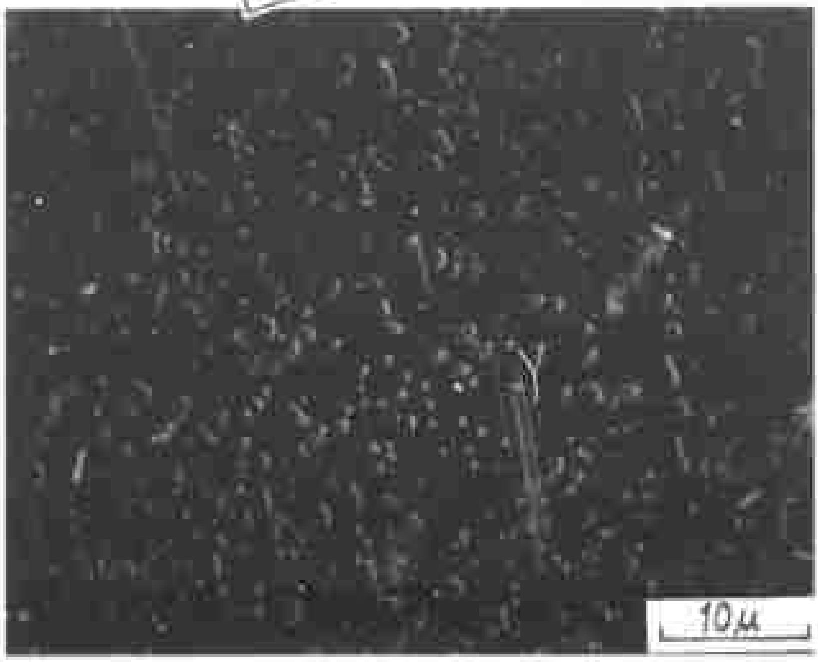

Figure 1 - Carbide inclusions in spheroidized 1045 steel.

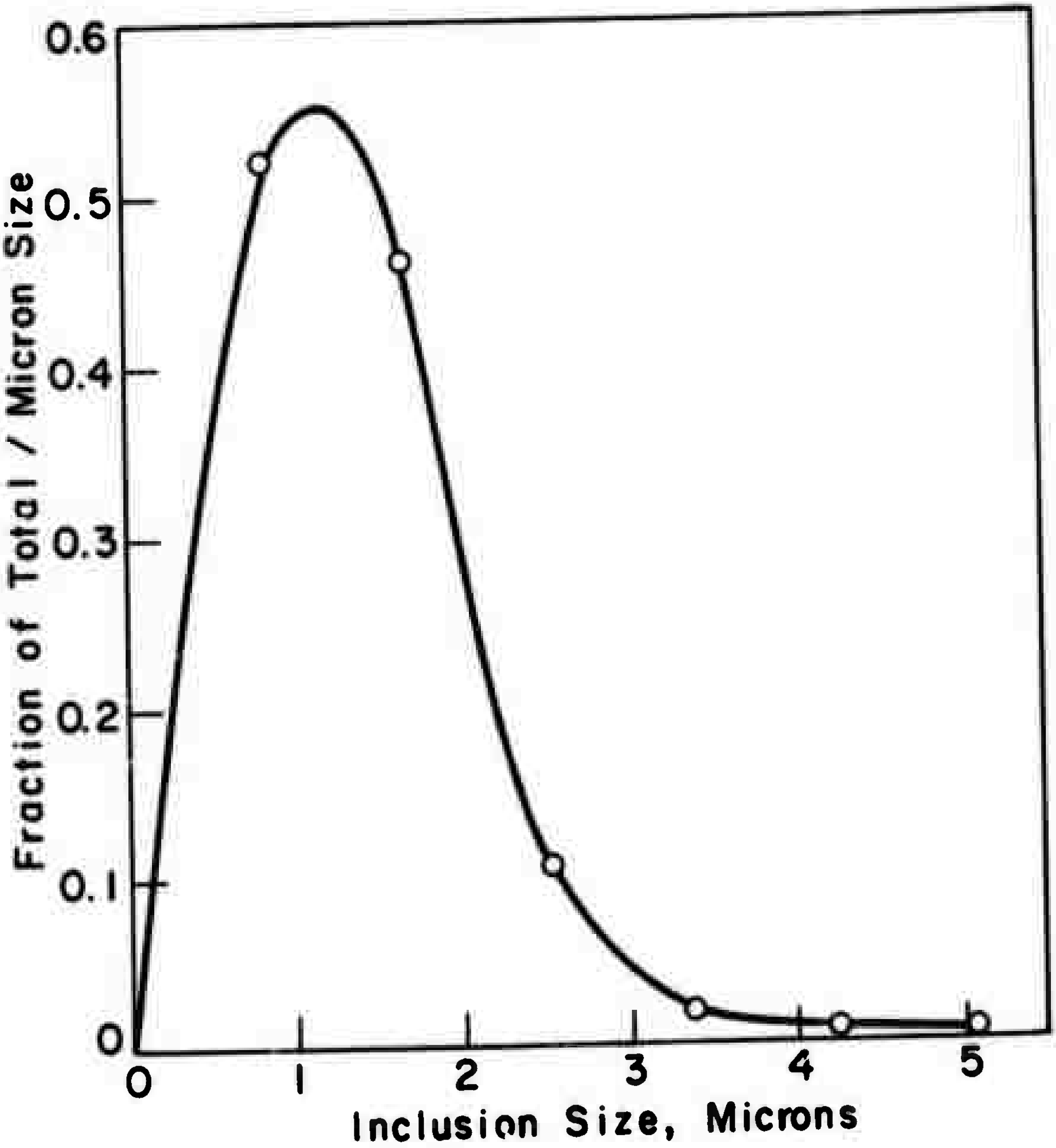

Figure 2 - Frequency distribution of sizes of carbide inclusions in spheroidized 1045 steel.

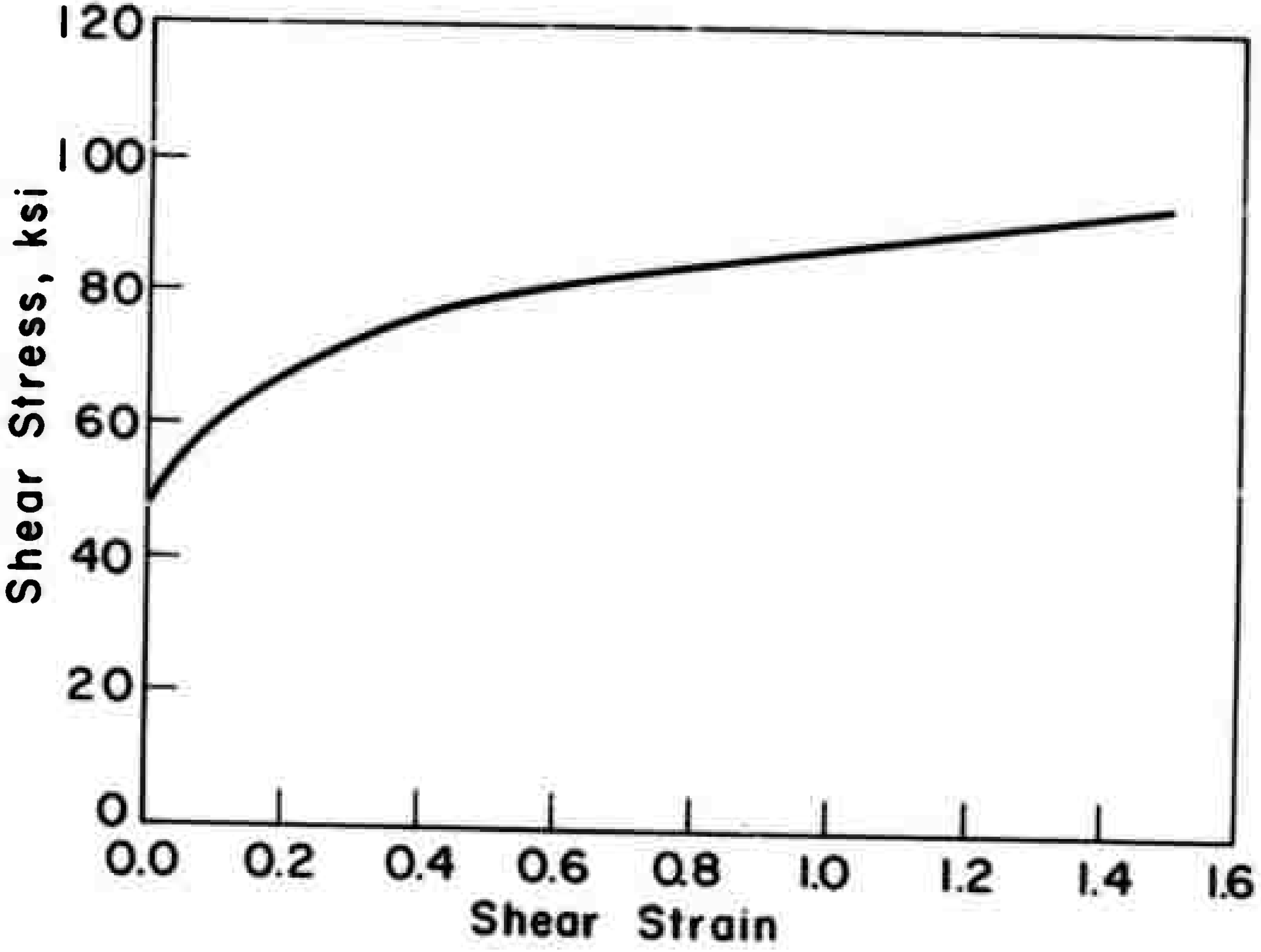

Figure 3 - Stress strain curve of spheroidized 1045 steel.

Figure 4 - General appearances of fracture surfaces of the six specimens deformed to fracture.

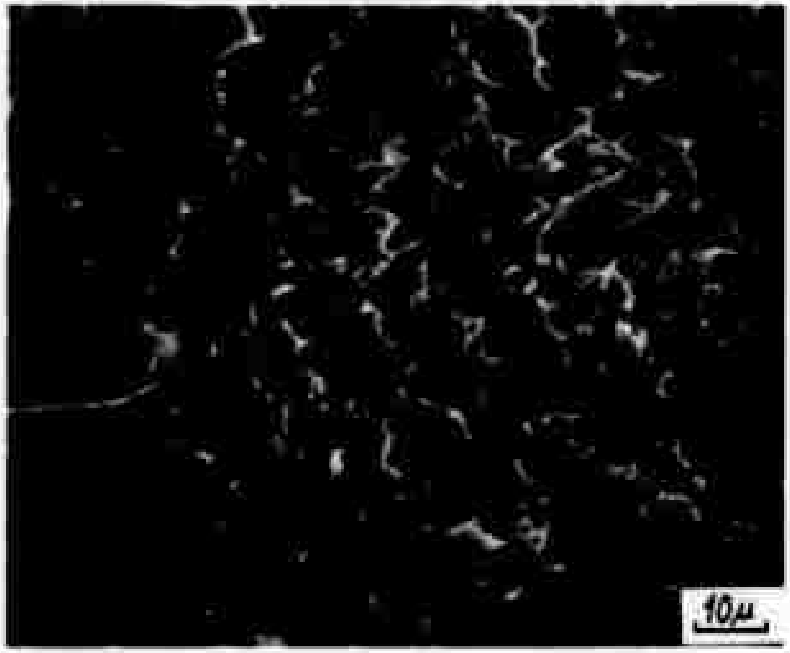

Figure 5 - Scanning electron micrograph of fracture surface of specimen #1 fractured in torsion.

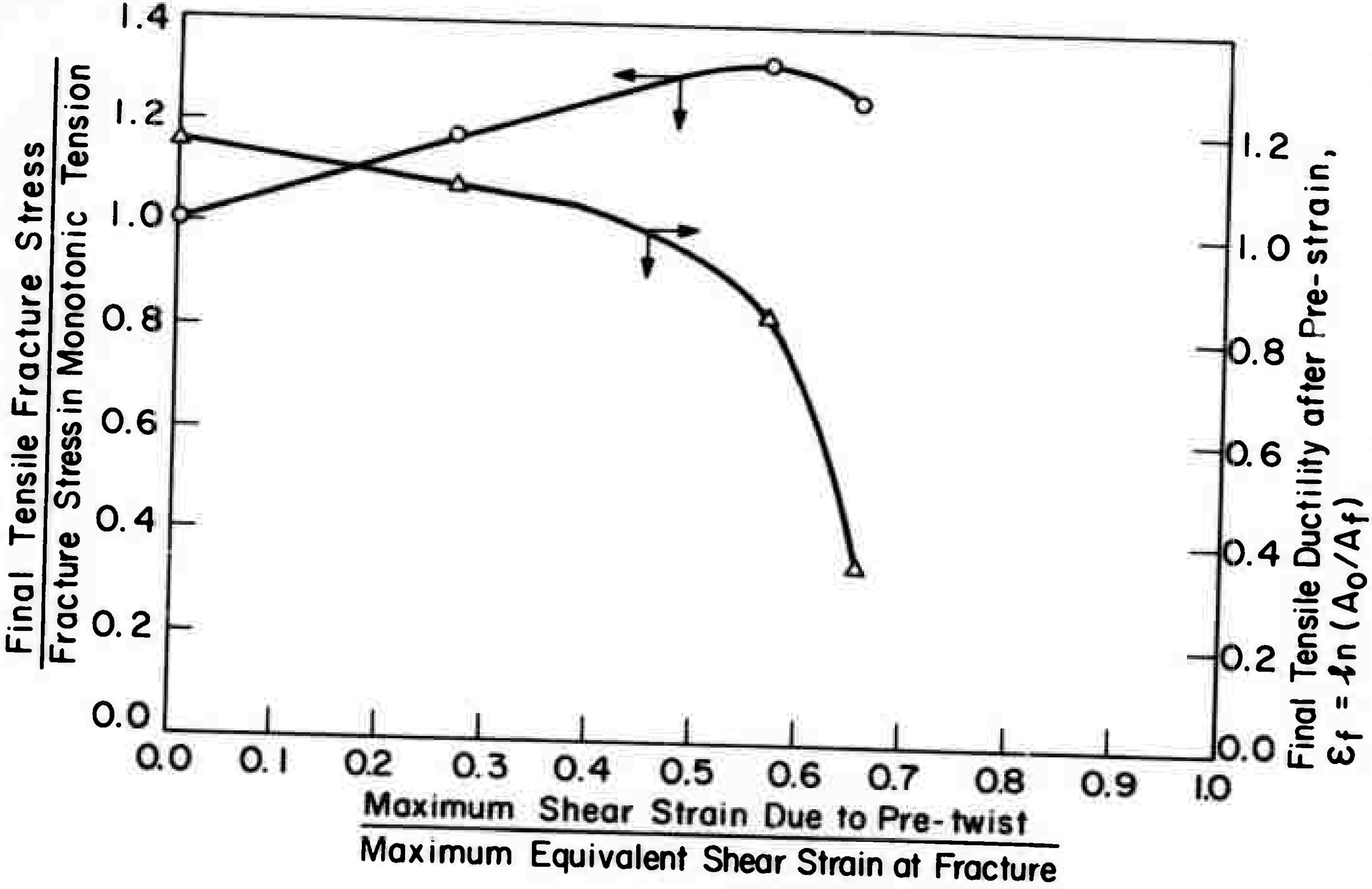

Figure 6 - Reduction in tensile ductility following unidirectional torsion, increase of tensile fracture stress resulting from additional strain hardening imparted during the torsional pre-straining.

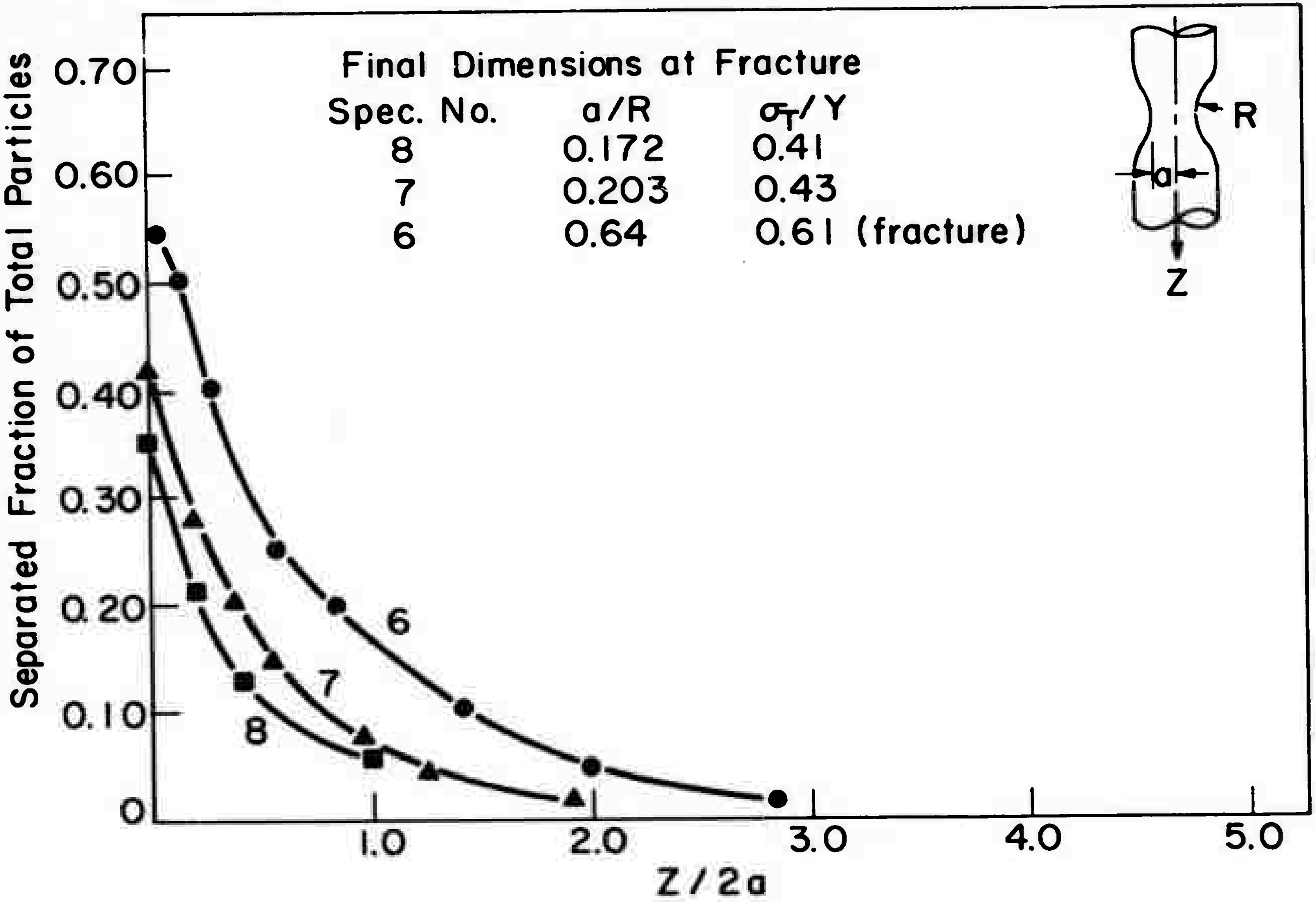

Figure 7 - Decrease of separated fraction of inclusions away from the median plane, for three different necks of increasing acuity.